Submicron scale metamorphic processes in the Óbrennberg Micaschist from the Sopron area

RESEARCH REPORT

Summary of research activities

The research grant has been awarded for three years from 01.09.2012. The original research period has been intermitted and extended twice between 01.03.2013 and 31.07.2014 because of child birth and between 01.06.2016. and 31.03.2017 because of family reasons by the permission of the scientific committee. The original host institute of the project, the Geological and Geophysical Institute of Hungary was merged into the Mining and Geological Survey of Hungary at 01.07.2017, therefore the final the closing date of the project has been modified to 31.01.2018. Due to the family reasons leading to the second intermission, the principal investigator has resigned from the host institute by 30.11.2017, when the originally planned 36 months research has ended.

The project aimed to re-evaluate and refine the metamorphic evolution of andalusite-sillimanite-biotite schist from Óbrennberg Micaschist using state of the art analytical techniques and thermodynamic modelling tools. The studied sample set of 79 thin sections from 62 hand specimens was collected during field work and scientific cooperation.

Main and trace element composition of the Óbrennberg Micaschist was determined from average whole rock specimens using ICP-OES at the Geological and Geophysical Institute of Hungary. Sm-Nd dating of ultraclean garnet separates and Rb-Sr age determination of biotite separates were carried out at the Austrian Geological Survey. 8 thin sections from 5 selected samples were studied in high resolution in order to describe submicron scale characteristics using a field emission gun scanning electron microscope at the MTA-ME Materials Science Research Group - Bay Zoltán Nonprofit Ltd. Main element distributions of garnet porphyroblasts were first studied at the University of Miskolc on larger scale and selected grains were studied on the micrometer scale at ETH Zurich and on the submicron scale at the University of Vienna. This was complemented by electron microprobe analyses carried out at the ETH Zurich and at the University of Vienna.

Based on these information, phase equilibria models were calculated for three stages of the metamorphic evolution using the PERPLE_X software package (Connolly 2009) and the internally consistent thermodynamic database of Holland and Powell (1998). The originally planned garnet isopleth thermobarometry was not applicable because the chemical zoning of the garnet porphyroblasts seems to be influenced by local pressure variations and local chemical reactions as well. Therefore the planned procurement of the extra thin diamond disk for serial slicing of rocks was cancelled.

The originally planned research was extended by the systematic study of in situ trace element composition of different zones of garnet porphyroblasts and main rock forming phases of the Óbrennberg Micaschist and Kő-hegy orthogneiss from Sopron area using LA-ICP-MS installed at the Geological and Geophysical Institute of Hungary. In addition, an ultrathin sample have been prepared by FIB for TEM investigation of retrograde garnet breakdown on the submicron scale.

Summary of the results

The project focused on the metamorphic evolution of andalusite-sillimanite-biotite schist. The opened questions in connection with the Óbrennberg Micaschist addressed in the research plan, such as re-evaluation of microstructural features, P-T conditions, timing of metamorphic events and correlation with Austroalpine analogues have been mostly resolved during the research period. The extension of the project with the trace element analyses of the rock-forming minerals have shown that trace element redistribution in metamorphic reactions can be used for the refinement of metamorphic evolution. The result have been presented on numerous scientific conferences (Dégi et al. 2015a,b; Király et al. 2015, 2016, 2017; Schuster et al. 2017; Török et al. 2017) and summarized in two manuscripts Dégi et al. (2018), submitted to Mineralogy and Petrology and Török et al. (in prep), to be submitted to Chemical Geology. The most important results of all research topics concerned by this project are found below.

1. Microstructural relation between different pre-Alpine domains

The studied andalusite-sillimanite-biotite schist from Óbrennberg Micaschist has uniquely preserved numerous pre-Alpine mineral relics in three domain types. Kfs-Pl-Sil-Bt-rich bands are dominated by the high temperature mineral assemblage of Ti-rich biotite, poikilitic plagioclase, K-feldspar with albitic exsolutions, sillimanite and quartz, which is partly replaced by a new garnet, staurolite, biotite, muscovite, plagioclase mineral assemblage. Garnet porphyroblasts are strongly zoned: a Ca-rich inclusion free core (Grt-I), an Fe-rich outer core (Grt-II), a Mn-rich zone (Grt-III) and a locally occurring outermost zone containing ilmenite inclusions (Grt-IV). Andalusite porphyroblasts has two generations sometimes separated by fibrous sillimanite. The older, deformed inclusion-rich And1A generation contains sillimanite laths, staurolite, biotite ±spinel ±corundum ±quartz inclusions, while the undeformed And2A generation contains mainly biotite and quartz.

The conventional petrological description extended by submicron scale microstructural features and element distributions allowed to distinguish between mineral assemblages representing the whole rock in different stages of metamorphism and mineral assemblages which are products of local mineral reactions (Dégi et al. 2018). Different mineral assemblages and reactions in all domains are classified to three main events. Stage1 preceded the high temperature event, referred to as Stage2, while Stage3 postdated Stage2. Detailed study of contacts between minerals of different domains together with element distributions of garnets and thermodynamic modelling have shown the relation of pre-Alpine domains to each other and to the metamorphic stages. Based on local garnet-consuming reactions it has been proven that garnet was not stable at the temperature peak of Stage 2 when the high temperature mineral assemblage of Kfs-Pl-Sil-Bt-rich bands were formed. The presence of fibrous sillimanite between the two andalusite generations implies that the formation of And1 and And2 preceded and postdated the temperature peak. Based on detailed analysis of inclusions and phase equilibria modelling, both andalusite generations could be fitted to the retrograde part of the metamorphic stage. These imply that cores of garnet porphyroblasts (Grt-I and Grt-II), biotite, sillimanite, staurolite and plagioclase and were formed in Stage1. The temperature peak in Stage2 resulted in the formation of Ti-rich biotite, plagioclase, K-feldspar, sillimanite ± melt. The mineral assemblage formed in Stage3 includes new garnet, staurolite, biotite, muscovite and plagioclase. The local reactions of inclusions in andalusite porphyroblasts, as well as local garnet-forming reactions could be correlated to Stage3. In addition, it was proven that the breakdown of staurolite to andalusite, spinel and corundum is a result of local chemical variations and therefore cannot be used for P–T estimation. This clarified some discrepancies and contradictions regarding the P–T history of the andalusite-sillimanite-biotite schist published in earlier studies.

2. P–T–t evolution of the Óbrennberg Micaschist

In order to study the formation conditions of different mineral assemblages, P–T phase diagram sections were calculated for the measured whole rock composition representing Stage1 and bulk compositions corrected based on petrological considerations for Stage2 and 3. This was combined with garnet-biotite geothermometry for local equilibrium pairs. Based on this the following PT path was derived. The Stage1 peak was achieved in the garnet-sillimanite stability field. This was followed by decompression and cooling to 550−650 °C and 0.4−0.6 GPa to form Stage1 staurolite, which was decomposed to andalusite and biotite below 570 °C 0.37 GPa. In Stage2 near isobaric heating at c.a. 0.4 GPa to the temperature peak between 650–680 °C resulted in the destabilization of andalusite and garnet and the formation of a K-feldspar-sillimanite-biotite-plagioclase-melt mineral assemblage. This was followed by isobaric cooling leading to rehydration due to in situ melt crystallization and the formation of the second andalusite generation between 590–570 °C. Nearly isothermal compression in the Alpine prograde path from 580 °C, 0.36 GPa to a maximum of 680 °C, 0.65 GPa was followed by retrograde decompression and cooling in the staurolite stability field down to 560 °C, 0.35 GPa.
We have shown clear evidence that andalusite-sillimanite-biotite schist from the Óbrennberg Micaschist did not experience high pressure Alpine metamorphism (with peak pressures above 1.0 GPa) as the surrounding kyanite-staurolite-chloritoid-garnet bearing micaschist or rocks of the Sopron series. These results open new questions mainly with respect to the structural geology of the area.

3. Dating of metamorphic events and correlation with Austroalpine analogues

Inclusion-free cores of garnet porphyroblasts were dated by the Sm-Nd method to be 330.4±2.7 Ma. This is the first study where the existence of c. 330 Ma Variscan mineral relics is proved. This gives direct evidence for the existence of two pre-Alpine tectonic phases, which was a question of debate in earlier works. The low pressure – high temperature event of Stage2 was assigned to be Permo-Triassic while Stage3 was correlated with the Alpine tectonometamorphic event. Based on the fact that the andalusite-sillimanite-biotite micaschist did not experience Alpine high pressure metamorphism as the surrounding rocks within the same tectonic unit together with microstructural observations and timing of metamorphism, the Óbrennberg Micaschist is correlated to the Rabenwald Nappe in Styria/Austria (Dégi et al. 2018).

4. The behaviour of trace elements in metamorphic reactions

Main and trace element profiles revealed from ICP-MS measurements combined with by high resolution main element distributions taken from FE-EPMA and trace element maps obtained from micro-PIXE allow for determining the limits and P–T conditions of garnet growth phases as it is shown in Török et al. (in prep). For the case of Kő-hegy gneiss from Sopron area, magmatic and metamorphic growth phases are further divided to 4 and 3 subzones, respectively. The change of main element and REY distributions between the subzones can be used for precise zone boundary definition and the identification of conditions and processes acting during garnet growth.

5. Redistribution of zinc during high temperature metamorphic reactions

Systematic measurement of Zn concentration in garnet, staurolite and biotite have shown that at low temperatures Zn is preferably hosted by staurolite. The water released from the decomposition of staurolite to andalusite and biotite should have percolated in the rock and transported Zn to larger distances, since the Zn-content of garnet reaches its maximum in the Mn-rich Grt-III zone formed right after staurolite decomposition at the early prograde part of the Permo-Triassic low pressure – high temperature event (Király et al. 2015). After the decomposition of garnet, Ti-rich, high temperature biotite sank the Zn, but following cooling Zn was not redistributed again although the P–T conditions during Alpine staurolite formation were similar as in the Variscan. This may imply that the structure of Ti-rich biotite allows for the accumulation of Zn. The results on the distribution of Zn between staurolite, garnet and biotite may be subject of international interest. However, this requires further systematic measurements.

Perspectives

In the sample Ka-3a, a submicron scale retrograde metamorphic reaction, the breakdown of garnet to biotite and aluminosilicate in the presence of fluid was observed. The reaction front was sampled by FIB. A combined TEM-Raman study in order to determine the structure of the aluminosilicate and the reaction front as well as element distributions of phases involved in the reaction could make high impact in the future.

References

Connolly JAD (2009) The geodynamic equation of state: what and how. Geochemistry, Geophysics, Geosystems 10:Q10014 DOI:10.1029/2009GC002540

Dégi J, Schuster R, Király E, Zajzon N, Tajcmanova L (2018) Distinction of Variscan, Permo-Triassic and Alpine metamorphic events in the Óbrennberg Micaschist, Sopron area (W-Hungary): phase equilibria modelling and Sm-Nd age dating. Submitted to Mineralogy and Petrology

Dégi J, Török K, Schuster R (2015a): Szubmikrométeres léptékű megfigyelések az Óbrennbergi Csillámpalában — Három tektonikai ciklus elkülönítése. 6. Kőzettani és Geokémiai Vándorgyűlés, 2015. szeptember 10–12., Ópálos, Románia, Meddig ér a takarónk? A magmaképződéstől a regionális litoszféra formáló folyamatokig, 42-45.

Dégi J, Török K, Schuster R (2015b) Distinction of Variscan, Permo–Triassic and Alpine events in andalusite–biotite–sillimanite schists from Sopron area, W-Hungary. 13th Meeting of the Central European Tectonic Studies Groups. Abstract Volume, 12.

Holland TJB, Powell R (1998) An internally consistent thermodynamic data set for phases of petrological interest. J Metamorph Geol 16: 309–343

Király E, Török K, Dégi J (2015): Gránátok nyomelemvilága mórágyi és soproni minták alapján 6. Kőzettani és Geokémiai Vándorgyűlés, 2015. szeptember 10–12., Ópálos, Románia. Meddig ér a takarónk? A magmaképződéstől a regionális litoszféra formáló foyamatokig, 75-78.

Király E, Török K, Dégi J, Kertész Zs, Abart R (2016): A kő-hegyi (Soproni-hegység) gránátok magmás és metamorf képződésének körülményei EMPA, PIXE és LA-ICP-MS vizsgálatok alapján. 7. Kőzettani és Geokémiai Vándorgyűlés, 2016. szeptember 22–23., Debrecen. Itt az idő! Kőzettani-geokémiai folyamatok és azok geokronológiai vonatkozásai, 45–48.

Király E, Török K, Dégi J, Kertész Zs, Abart R (2017) Garnet growth history in Kő-hegy gneiss (Sopron Mts, Hungary): combined FE-EPMA, micro-PIXE and LA-ICP-MS study CETEG 2017, 15th Meeting of the Central European Tectonic Studies Groups. Abstract Book, Acta Mineralogica-Petrographica 32:38

Schuster R, Reiser M, Linner M, Dégi J, Király E (2017) Correlation of basement units from the Pannonian basin and surrounding areas based on lithological associations and the distribution of tectonometamorphic imprints. CETEG 2017, 15th Meeting of the Central European Tectonic Studies Groups. Abstract Book, Acta Mineralogica-Petrographica 32:35

Török K, Király E, Dégi J (2017) A Soproni Gneisz csillámainak nyomelem-geokémiai változásai a magmás–metamorf fejlődéstörténet tükrében. 8. Kőzettani és Geokémiai Vándorgyűlés, 2017. szeptember 7–9., Szihalom, Absztrakt kötet, 164–167

Török K, Király E, Dégi J, Kertész Zs, Abart R, Maigut V (in prep) Refinement of the evolution history of garnet (from Grobgneiss of Kő-hegy, Sopron Mountains, Hungary) based on major- and trace-element studies by EMPA, micro-PIXE and LA-ICP-MS. Planned to be submitted to Chemical Geology by February 2019

Mineralogy and Petrology

Distinction of Variscan, Permo-Triassic and Alpine metamorphic events in the Óbrennberg Micaschist, Sopron area (W-Hungary): phase equilibria modelling and Sm-Nd age dating

--Manuscript Draft--

Manuscript Number:	MIPE-D-18-00184
Full Title:	Distinction of Variscan, Permo-Triassic and Alpine metamorphic events in the Óbrennberg Micaschist, Sopron area (W-Hungary): phase equilibria modelling and Sm-Nd age dating
Article Type:	Standard Article
Keywords:	garnet porphyroblast; Sm-Nd age; Óbrennberg Micaschist; thermodynamic modelling; Sopron
Corresponding Author:	Júlia Dégi Mining and Geological Survey of Hungary Budapest, HUNGARY
Corresponding Author Secondary Information:	
Corresponding Author's Institution:	Mining and Geological Survey of Hungary
Corresponding Author's Secondary Institution:	
First Author:	Júlia Dégi
First Author Secondary Information:	
Order of Authors:	Júlia Dégi
	Ralf Schuster
	Edit Király
	Norbert Zajzon
	Lucie Tajcmanova
Order of Authors Secondary Information:	
Funding Information:	Hungarian National Research, Development and Innovation Office (OTKA PD 104692) — Dr Júlia Dégi Magyar Tudományos Akadémia (Bolyai János Research Scholarship) — Dr Júlia Dégi
Abstract:	Polymetamorphic andalusite-sillimanite-biotite schist from the Óbrennberg Micaschist contains well-preserved relics of pre-Alpine mineral assemblages in three different domains and therefore provide a unique opportunity to reconstruct the complete P–T–t path of an Austroalpine unit in the Sopron area. Microstructural characteristics, major and trace element zoning patterns, garnet Sm-Nd ages and mineral stabilities were studied in order to determine mineralogical changes over time. Three stages of metamorphic evolution are distinguished. Cores of garnet porphyroblasts formed at 330 Ma in equilibrium with staurolite which corresponds to the Variscan metamorphic peak around 600650 °C 0.6 GPa. This was followed by decompression and cooling below 570 °C 0.37 GPa where staurolite and muscovite decomposed to form andalusite and biotite. Nearly isobaric heating to 650680 °C around 0.370.40 GPa during the Permo-Triassic high temperature – low pressure event led to the formation of the K-feldsparplagioclasesillimanitebiotite mineral assemblage, which constitutes the majority of the rock. Retrograde cooling induced mineral exsolutions, rehydration processes and intensive andalusite formation between 590570 °C. The following prograde and retrograde path – interpreted to be Alpine with peak conditions of 640 °C and 0.65 GPa is recorded in newly formed zoned garnets. The results from the phase equilibria modelling indicate that the Óbrennberg Micaschist experienced only medium

Refinement of the evolution history of garnet (from Grobgneiss of Kő-hegy, Sopron Mountains, Hungary) based on major- and trace-element studies by EMPA, micro-PIXE and LA-ICP-MS.

Török, K., Király, E., Dégi, J., Kertész, Zs., Abart, R., Maigut V.

Abstract

We studied garnets from the high pressure/medium temperature orthogneiss and a coarse grained pegmatitic nest from the Kő-hegy, (Sopron Mountains, Hungary) by means of EMPA, LA-ICP-MS and Micro PIXE to unravel a complex garnet growth during the magmatic and metamorphic history of the gneiss. Complex changes of major and trace elements in the garnets enabled us to reveal the processes that operated during garnet growth and thus to refine the magmatic and metamorphic evolution of the gneisses around Sopron. Garnets with complex magmatic and metamorphic zoning were found in a coarse grained pegmatitic nest. The magmatic history starts with the formation of the garnet cores (Z1), which are characterized by relatively high rare-earth element and Y (REY) content. The REY distribution shows enrichment of heavy rare earth elements (HREE-s). It is overgrown by a depleted zone with oscillatory zoning and the lowest REY-contents (Z2). The following zone (Z3) is distinguished by limited enrichment in Ca and trace elements and a finer scale oscillatory zoning, than in Z2. The evolution of magmatic garnet is completed with zone Z4, where depletion of Ti, Zr and Ca was observed. Oscillatory zoning in magmatic garnet is coupled with modified REY patterns (humpback distribution) relative to Z1 indicating non-equilibrium, probably open-system conditions, changes in growth rate and fractionation of heavy REE-s in the core (Z1). After partial resorption of the magmatic zones, 3 narrow zones (Z5-7) of Alpine metamorphic garnet are overgrown on the resorbed magmatic grain with distinctive Ca enrichment relative to the magmatic part. The REY distribution pattern changes again from humpback to increased heavy REE, similar to the Z1 and the REY content increases relative to Z4. The second metamorphic zone (Z6) with the highest Ca and decreasing REY content relative to Z5 represents the metamorphic peak pressure and temperature conditions. The last zone, Z7 is discontinuous and displays Mn and REY enrichment and is thought to belong to the Alpine retrograde phase. The highest concentrations of REY were detected in the limbs of this last zone developed in pressure shadows, which were interpreted as an effect of retrograde metamorphic fluids, which percolated the Grobgneiss.

Garnet from gneiss reveals different major (grossular content about 50%) and trace element geochemistry (low REE and Zn, high Ti), than either magmatic or metamorphic zones of pegmatitic nests. The main reason can be the difference in compositions of the local environment and/or the different garnet forming reactions.

Introduction

Several aspects of the metamorphic history of the metamorphic rocks belonging to the Austroalpine basement, outcropping in the Sopron Mountains were discussed in the last three decades. Previous authors first described low grade alpine metamorphism of orthogneisses (Lelkes-Felvári et al., 1984; Kisházi & Ivancsics, 1985, 1987a,b, 1989) using petrography, mineral and bulk rock chemistry. Later Alpine high pressure, medium temperature metamorphism was discovered and described for the orthogneiss (Török, 1996, 1998, 2001),

Mineralogy and Petrology

Distinction of Variscan, Permo-Triassic and Alpine metamorphic events in the Óbrennberg Micaschist, Sopron area (W-Hungary): phase equilibria modelling and Sm-Nd age dating

--Manuscript Draft--

Manuscript Number:	MIPE-D-18-00184
Full Title:	Distinction of Variscan, Permo-Triassic and Alpine metamorphic events in the Óbrennberg Micaschist, Sopron area (W-Hungary): phase equilibria modelling and Sm-Nd age dating
Article Type:	Standard Article
Keywords:	garnet porphyroblast; Sm-Nd age; Óbrennberg Micaschist; thermodynamic modelling; Sopron
Corresponding Author:	Júlia Dégi Mining and Geological Survey of Hungary Budapest, HUNGARY
Corresponding Author Secondary Information:	
Corresponding Author's Institution:	Mining and Geological Survey of Hungary
Corresponding Author's Secondary Institution:	
First Author:	Júlia Dégi
First Author Secondary Information:	
Order of Authors:	Júlia Dégi
	Ralf Schuster
	Edit Király
	Norbert Zajzon
	Lucie Tajcmanova
Order of Authors Secondary Information:	
Funding Information:	Hungarian National Research, Development and Innovation Office (OTKA PD 104692) — Dr Júlia Dégi
	Magyar Tudományos Akadémia (Bolyai János Research Scholarship) — Dr Júlia Dégi
Abstract:	Polymetamorphic andalusite-sillimanite-biotite schist from the Óbrennberg Micaschist contains well-preserved relics of pre-Alpine mineral assemblages in three different domains and therefore provide a unique opportunity to reconstruct the complete P–T–t path of an Austroalpine unit in the Sopron area. Microstructural characteristics, major and trace element zoning patterns, garnet Sm-Nd ages and mineral stabilities were studied in order to determine mineralogical changes over time. Three stages of metamorphic evolution are distinguished. Cores of garnet porphyroblasts formed at 330 Ma in equilibrium with staurolite which corresponds to the Variscan metamorphic peak around 600650 °C 0.6 GPa. This was followed by decompression and cooling below 570 °C 0.37 GPa where staurolite and muscovite decomposed to form andalusite and biotite. Nearly isobaric heating to 650680 °C around 0.370.40 GPa during the Permo-Triassic high temperature – low pressure event led to the formation of the K-feldsparplagioclasesillimanitebiotite mineral assemblage, which constitutes the majority of the rock. Retrograde cooling induced mineral exsolutions, rehydration processes and intensive andalusite formation between 590570 °C. The following prograde and retrograde path – interpreted to be Alpine with peak conditions of 640 °C and 0.65 GPa is recorded in newly formed zoned garnets. The results from the phase equilibria modelling indicate that the Óbrennberg Micaschist experienced only medium

	pressure metamorphism in the Alpine cycle, whereas the surrounding rock types from Sopron area record high pressure Alpine metamorphism. The lack of the high-pressure metamorphism in this sample might have led to the unique preservation of the two pre-Alpine events.
Suggested Reviewers:	

Distinction of Variscan, Permo-Triassic and Alpine metamorphic events in the Óbrennberg Micaschist, Sopron area (W-Hungary): phase equilibria modelling and Sm-Nd age dating

Júlia DÉGI[1]*, Ralf SCHUSTER[2], Edit KIRÁLY[1], Norbert ZAJZON[3], Lucie TAJCMANOVA[4]

[1] Mining and Geological Survey of Hungary, Stefánia út 14, H-1145 Budapest, Hungary
[2] Geological Survey of Austria, Neulinggasse 38, 1030 Vienna, Austria
[3] Institute of Mineralogy and Geology, University of Miskolc, H-3515 Miskolc-Egyetemváros, Hungary
[4] Department of Earth Sciences, ETH Zurich, Sonneggstrasse 5, Zurich 8092, Switzerland
* Corresponding author (e-mail: julia.degi@gmail.com, telephone: +36 30 212 8534)

ORCID:
Júlia Dégi 0000-0002-2758-8487
Ralf Schuster
Edit Király
Norbert Zajzon
Lucie Tajcmanova

Abstract
Polymetamorphic andalusite-sillimanite-biotite schist from the Óbrennberg Micaschist contains well-preserved relics of pre-Alpine mineral assemblages in three different domains and therefore provide a unique opportunity to reconstruct the complete *P–T–t* path of an Austroalpine unit in the Sopron area. Microstructural characteristics, major and trace element zoning patterns, garnet Sm-Nd ages and mineral stabilities were studied in order to determine mineralogical changes over time. Three stages of metamorphic evolution are distinguished. Cores of garnet porphyroblasts formed at 330 Ma in equilibrium with staurolite which corresponds to the Variscan metamorphic peak around 600−650 °C 0.6 GPa. This was followed by decompression and cooling below 570 °C 0.37 GPa where staurolite and muscovite decomposed to form andalusite and biotite. Nearly isobaric heating to 650−680 °C around 0.37−0.40 GPa during the Permo-Triassic high temperature – low pressure event led to the formation of the K-feldspar−plagioclase−sillimanite−biotite mineral assemblage, which constitutes the majority of the rock. Retrograde cooling induced mineral exsolutions, rehydration processes and intensive andalusite formation between 590−570 °C. The following prograde and retrograde path – interpreted to be Alpine − with peak conditions of 640 °C and 0.65 GPa is recorded in newly formed zoned garnets. The results from the phase equilibria modelling indicate that the Óbrennberg Micaschist experienced only medium pressure metamorphism in the Alpine cycle, whereas the surrounding rock types from Sopron area record high pressure Alpine metamorphism. The lack of the high-pressure metamorphism in this sample might have led to the unique preservation of the two pre-Alpine events.

Keywords: garnet porphyroblast, Sm-Nd age, Óbrennberg Micaschist, thermodynamic modelling, Sopron

1. Introduction

The Sopron area (W-Hungary) is located at the margin of the Eastern Alps being one of the easternmost places where rocks of the Austroalpine nappes can be studied at the surface (**Fig. 1**). Polymetamorphic metapelite, various types of orthogneiss, minor amphibolite and pegmatite of the area (Kisházi and Ivancsics 1985) have been subdivided into the Sopron series and the Óbrennberg Micaschist by Draganits (1998). Of special interest is the andalusite-biotite-sillimanite schist of the Óbrennberg Micaschist which records a complex pre-Alpine metamorphic history. Due to a variable but often weak Alpine retrogression this rock provides a unique opportunity to reconstruct its complete Phanerozoic metamorphic evolution, which is an important information for the geodynamic evolution of the Austroalpine units as a whole.

Although several studies aimed to determine the *P–T–t* evolution of the Óbrennberg Micaschist, there remain many open questions. Often the petrological relations are not clear because pre-Alpine relics are found in domains separated from each other in space. Therefore, uncertainty exists with respect to the number of pre-Alpine metamorphic imprints, and to which of the different regional tectonometamorphic events they are attributed. Lelkes-Felvári et al. (1984) argued for the existence of two pre-Alpine events, a 'Caledonian' (Ordovician) Barrovian-type metamorphism and a Variscan ('Hercynian') high temperature event. However, observations of Török (1999) did not support the presence of a Barrovian-type metamorphism. He suggested that a pre-Alpine temperature maximum preceded the pressure peak. Draganits (1998) found evidence only for a single high temperature event in the pre-Alpine evolution. In Schuster et al. (2001a) the formation of andalusite and sillimanite is interpreted to be the product of a regional Permo-Triassic high temperature – low pressure event. The inclusions of kyanite within andalusite and at the rims of the andalusite porphyroblasts are attributed to the Cretaceous (eo-Alpine) tectonometamorphic event.

Additionally, the relations of the Óbrennberg Micaschist to the Sopron series and the correlation of these units to other Austroalpine Complexes are still the subject of debate. Draganits (1998) suggested that the Óbrennberg Micaschist (Óbrennberg-Kaltes Bründl series in Austrian literature) should be correlated with the Strallegg Complex (sensu Wieseneder 1971), whereas the Sopron series is part of the Grobgneis unit. On the other hand, Alpine metamorphic evolution and peak *P–T* conditions of kyanite-staurolite-chloritoid-garnet-bearing micascist from the Óbrennberg Micaschist and massive orthogneiss from the Sopron series are very similar. Based on this, Török (2003) suggests that the two series were metamorphosed together during the Alpine high pressure event and should be treated as one unit. However, the imprints of Alpine metamorphism in andalusite-sillimanite-biotite schists usually appear as small scale local reactions for which *P–T* estimates have not been done in earlier works.

Recent improvements in analytical and phase equilibria modelling techniques provide opportunity to revise the open questions in connection with the andalusite-biotite-sillimanite schist. In this study we describe petrological features and element distributions of this special rock type using high resolution electron microscopy in order to better distinguish and correlate mineral generations in the pre-Alpine domains. New observations are combined with the results of Sm-Nd dating of garnet porphyroblasts, Rb-Sr dating of biotites and phase equilibria modelling to refine and distinguish stages of the metamorphic evolution of the Óbrennberg Micaschist in the Sopron area and the relation of the andalusite-biotite-sillimanite schist to similar lithologies in other Austroalpine units.

2. Regional geology

The Sopron area, located at the Austrian-Hungarian border (**Fig. 1**), is formed by polymetamorphic rocks of the Austroalpine nappes, which are surrounded by Neogene sediments of the Pannonian Basin and its marginal embayments. Draganits (1998) classified the metamorphic rocks of the Sopron area into two series, the Sopron series and the Óbrennberg Micaschist. The latter is referred to as Óbrennberg-Kaltes Bründl series in Austrian terminology. The Sopron series (Lelkes-Felvári et al. 1984; Kisházi and Ivancsics 1985, 1987a, 1987b, 1989; Török 1996, 1998, 2001, 2003; Demény et al. 1997) consists of garnet-bearing chlorite-muscovite-quartz schist, massive orthogneiss, leucophyllite and subordinate amphibolite, all of which dominantly record Alpine metamorphism. On the other hand, the Óbrennberg Micaschist show a polymetamorphic character. Nearly undisturbed pre-Alpine mineral assemblages are preserved in andalusite-sillimanite-biotite schist (Lelkes-Felvári et al. 1984; Kisházi and Ivancsics 1987b; Török 1999), whereas kyanite-staurolite-chloritoid-garnet-bearing micaschist is considered to be the Alpine-overprinted variety of the andalusite-bearing schist (Kisházi and Ivancsics 1987b; Török 2003). Locally occurring kyanite-chloritoid-garnet or chloritoid-garnet bearing micaschist and chlorite-muscovite schist with or without garnet are interpreted as the retrogressed and/or Mg-metasomatized varieties of the kyanite-staurolite-chloritoid-garnet bearing micaschist (Török 2003). Metapelites from the Óbrennberg Micaschist are sometimes crosscut by orthogneiss veins (Kisházi and Ivancsics 1987b) thought to have formed during anatexis of the metapelites (Török 1999).

The *P–T* evolution of the Óbrennberg Micaschist had at least two stages, pre-Alpine and Alpine. The best preserved pre-Alpine relics are found in the andalusite-sillimanite-biotite schist in three microstructurally distinct domains: garnet porphyroblasts, andalusite porphyroblasts and Kfs-Pl-Sil-Bt-rich bands. Unfortunately, domain contacts are not well characterized, thus the relations among different pre-Alpine metamorphic processes in different domains are the subject of debate.

Regarding the pre-Alpine evolution of the rocks, many hypotheses exist. All authors agree in the existence of a high temperature − low pressure event with conditions of 0.3−0.5 GPa, 600−700 °C (Lelkes-Felvári et al. 1984; Kisházi and Ivancsics 1987b; Draganits 1998; Török 1999). Draganits (1998) states that this is the only pre-Alpine phase. In contrast, Lelkes-Felvári et al. (1984) argues for the existence of a ‘Caledonian’ (Ordovician) Barrovian-type metamorphism solely on petrographical basis. At the same time, Török (1999) argues for the presence of a high pressure (0.9 GPa, 650 °C) event postdating the temperature peak, i.e. counterclockwise $P-T$ evolution.

The timing of the different metamorphic stages in the Sopron area is uncertain as well, because only a limited amount of geochronological age data representing mineral formation ages or cooling ages through high temperatures are available. Nagy et al. (2002) provided Th-U-total Pb ages from LREE-phosphates. According to this, the first generation of monazite was formed at ca. 300 Ma, which they assigned to the Variscan event. The Alpine monazite generation yielded ages around 75 Ma. From the Óbrennberg Micaschist a Sm-Nd isochron including garnet, whole rock and biotite was measured on a garnet-quartz fels yielding 263±2 Ma and a Rb-Sr errorchron including two muscovite fractions, whole rock and plagioclase from a micaschist yielded 283±27 Ma (Schuster et al. 2001b).

Isotopic systems with low blocking temperatures partly show contradictory results. K/Ar ages measured from different biotite and white mica fractions cover a large time span from 330 to75 Ma (Balogh and Dunkl 2005). The oldest ages (> 200 Ma) were measured on biotites from the Óbrennberg Micaschist. As muscovites from the same samples are generally younger these values have to be interpreted as influenced by large amounts of excess Ar. Muscovite fractions with grain sizes between 80 and 315 μm yield age values in the range of 76 to 105 Ma, whereas larger grain sizes show scattering and often higher values. Ar-Ar dating on muscovites mostly shows disturbed age spectra with values between 280 and 90 Ma (Balogh and Dunkl 2005; Schuster et al. 2001b). Further zircon fission track ages in the range of 63–77 Ma and apatite fission track ages of 33–62 Ma have been reported. Based on these data it can be concluded that the peak of the Alpine imprint occurred in the Late Cretaceous and cooling of the rocks lasted until the late Eocene (Balogh and Dunkl 2005).

3. Analytical techniques

Submicron scale features of the samples were studied in high resolution using a Hitachi S-4800 Scanning Electron Microscope equipped with Bruker XFlash Detector 4010 type energy dispersive X-ray spectrometer at the Electron Microscope Laboratory of MTA-ME Materials Science Research Group - Bay Zoltán Nonprofit Ltd. Electron microprobe analyses were carried out at the Institute of Geochemistry and Petrology, ETH Zürich on JEOL JXA-8200 electron probe microanalyser equipped with WDS detectors. An acceleration voltage of 15 kV and a beam current of 20 nA were applied. The probe diameter was set to 5 and 2 μm in case of point analyses in plagioclase grains and micas, respectively. In all other cases the smallest possible beam diameter was used. Natural and synthetic mineral standards were used for calibration and ZAF correction was applied.
Part of the element distribution maps were produced at the Department of Mineralogy, University of Miskolc on a JEOL 8600 Superprobe in stage scanning mode using combined EDS-WDS system. Ca, Mn and Mg were detected using WDS detectors. Additional element distributions were measured at the Institute of Geochemistry and Petrology, ETH Zürich on JEOL JXA-8200 Superprobe in stage scanning mode using WDS detectors. An acceleration voltage of 15 kV, a beam current of 20 nA, dwell times between 100-300 ms and 0.50 – 2.0 micron step were applied in both cases.
An average sample was produced by crushing 12 kg of andalusite-sillimanite-biotite schist. Bulk composition of the average sample was determined using a Jobin Yvon ULTIMA-2C ICP-OES at the Department of Geochemistry and Laboratory, Geological and Geophysical Institute of Hungary.

For the Sm-Nd and Rb-Sr dating the minerals were separated from the remaining part of the crushed andalusite-sillimanite-biotite schist by the standard methods of crushing, grinding, sieving and magnetic separation. Garnet was hand-picked under the binocular microscope from sieve fractions 0.2–0.3 mm and cleaned in distilled water and acetone. Further it was leached in 6n HCl at 100 °C for several hours. Samples used for dissolution weighed about 100 mg for whole rock powder, ~200 mg for biotite and 30–45 mg for garnet. Chemical preparation was performed at the Geological Survey of Austria in Vienna and at the Department of Lithospheric Research at the University of Vienna. The chemical sample preparation follows the procedure described by Sölva et al. (2005). Element concentrations were determined by isotope dilution using mixed ^{147}Sm/^{150}Nd and ^{84}Rb/^{87}Sr spikes. Total procedural blanks are ≤300 pg for Nd and Sm and ≤1 ng for Rb and Sr. Isotopic ratios were measured at the Department of Geological Sciences, University of Vienna. Rb-ratios were determined with a Finnigan® MAT 262, whereas Sr, Sm and Nd ratios were analysed with a ThermoFinnigan® Triton TI TIMS. All elements were run from Re double filaments, except Rb which was evaporated from a Ta single filament. During measuring, the La Jolla standard yielded $^{143}Nd/^{144}Nd = 0.511845 \pm 1$ (n = 12, 2σm) on the Triton TI, whereas standard NBS987 yielded a ratio of $^{86}Sr/^{87}Sr = 0.710253 \pm 6$ (n=12, 2σm). Errors of 1% were determined for the $^{87}Rb/^{86}Sr$ and $^{147}Sm/^{144}Nd$ ratios based on interactive sample analysis and spike recalibration. Ages were calculated with the software ISOPLOT/Ex (Ludwig 2001; 2003) using the Sm- and Rb-decay constants of 6.54×10^{-12} a^{-1} and 1.42×10^{-11} a^{-1}, respectively.

4. Description of samples from the Óbrennberg Micaschist

The studied micaschist is composed of andalusite, sillimanite, biotite, plagioclase, K-feldspar and quartz. Besides these, staurolite, garnet, muscovite, spinel, corundum, ilmenite, rutile, tourmaline, monazite and apatite may be present in small amounts. The rock is built up by alternating metapelitic and metapsammitic layers preserving chemical heterogeneities of the precursor sediments. This work focuses on metapelitic layers showing complex domainal structure. Usually up to 2 cm long elongated andalusite porphyroblasts alternate with quartz-rich or Kfs-Sil-Pl-Bt-rich bands. The latter may contain isolated garnet or andalusite porphyroblasts.

4.1. Microscale petrography and mineral chemistry

Pre-Alpine mineral relics are best preserved in garnet porphyroblasts, andalusite porphyroblasts, and Kfs-Sil-Pl-Bt-rich bands. In this chapter petrography and mineral chemistry of these domains are described. Two samples are studied in detail: KA-6n contains all types of pre-Alpine domains, whereas garnet porphyroblasts are absent from KA-10. Representative mineral chemical analyses of feldspar, mica, garnet and staurolite are given in Tab. 1-4, respectively.

4.1.1. Kfs-Sil-Pl-Bt-rich bands

Kfs-Sil-Pl-Bt-rich bands contain biotite, plagioclase, K-feldspar, sillimanite, quartz, muscovite and garnet grains, most of which have several generations (**Fig. 2**). The bands are dominated by large biotite flakes ($Bt1_K$) containing ilmenite inclusions (**Fig. 2a**) and millimetre sized poikilitic plagioclase grains ($Pl1_K$) hosting smaller K-feldspar (Kfs_K) and quartz grains (**Fig. 2b**). Fibrous sillimanites (Sil_K), sometimes intergrown with Kfs_K K-feldspars (**Fig. 2c**) as well as large muscovites ($Ms1_K$) containing relics of $Bt1_K$ (**Fig. 2d**), appear frequently. In addition, fine-grained subdomains containing euhedral garnet grains ($Grt1_K$, **Fig 2e**), sometimes reaching several hundred micrometre width, holding microstructural equilibrium with small staurolite ($St1_K$), muscovite ($Ms2_K$) and inclusion-free biotite laths ($Bt2_K$) as well as plagioclase grains ($Pl2_K$) are also found within these bands.

$Bt1_K$ biotites usually exceed several hundred micrometres in width. They are characterized by numerous ilmenite inclusions of micrometre to submicrometre size (**Fig. 2a**). These ilmenites frequently form trails along grain boundaries or cracks, more rarely they are found as solitary inclusions within the $Bt1_K$ grains. Along cracks within the $Bt1_K$ biotites, garnet ($Grt2_K$) and muscovite ($Ms3_K$) growth is observed. $Grt2_K$ overgrowths usually inherit oriented ilmenite inclusions from the precursor $Bt1_K$ grains.

Poikilitic $Pl1_K$ plagioclase grains reach millimetres in diameter and they contain numerous inclusions of quartz, Kfs_K K-feldspar and more rarely muscovite (**Fig. 2b**). Kfs_K K-feldspars appear as individual grains, sometimes intergrown with Sil_K sillimanite as well (**Fig. 2c**). 1−10 µm wide albitic plagioclase lamellae ($Pl3_K$) are frequently observed in larger Kfs_K K-feldspars in both microstructural positions (**Fig. 2b, c**). $Ms1_K$ muscovites may replace individual K-feldspars. The extent of alteration varies in a wide range, sometimes the complete grain is replaced.

In garnet-bearing subdomains, the appearance of garnet core and rim is completely different. Sometimes the core is absent. The core is rich in micron to submicron sized, anhedral biotite inclusions, whereas the rim is intergrown with a few tens of microns wide euhedral $Bt2_K$ biotite and $St1_K$ staurolite laths (**Fig. 2e**). Significantly smaller, euhedral staurolite laths or twins ($St2_K$) may be found as overgrowths on $Ms1_K$ muscovites (**Fig. 2d**) and $Bt1_K$ biotites, along cracks and in nests filled by ultrafine-grained alteration products as well (**Fig. 2e**). These nests, usually reaching a few tens of micrometers in diameter, are formed by submicron scale intergrowths of biotite and white micas, referred to as $MicaIG_K$, and pure albite.

4.1.2. Garnet porphyroblasts

The garnet porphyroblasts (Grt_G) are always found in Kfs-Sil-Pl-Bt-rich bands. However, their size and appearance is strikingly different from $Grt1_K$. Grt_G garnets show various shapes including rounded, elongated or xenoblastic, and their longest dimension may reach a few millimetres, whereas $Grt1_K$ grains are usually euhedral and the largest ones hardly reach 300 µm in diameter.

Grt_G garnets are considerably larger than the surrounding coarse-grained $Bt1_K$ biotite, $Pl1_K$ plagioclase or quartz grains (**Fig. 3**). Contacts between Grt_G and the surrounding minerals tend to be even. However, $Bt1_K$ biotite – Grt_G garnet grain boundaries have several embayments and protrusions.

Regarding inclusions, the core of Grt_G rarely contains inclusions, but their number increases fast towards the rim. Two types of biotite inclusions can be distinguished: $Bt1_G$ inclusions are usually euhedral, while $Bt2_G$ inclusions are related to cracks and they are usually found together with muscovite (Ms_G). At the contact of $Bt1_K$ biotite flakes and Grt_G garnet porphyroblasts, submicron sized ilmenite inclusions are found along a well-defined line parallel to the garnet-biotite phase boundary within 10-20 micrometres (**Fig. 3a** inlet).

4.1.3. Andalusite porphyroblasts

The andalusite-sillimanite-biotite schist is dominated by large elongated andalusite porphyroblasts reaching a few centimetres in length. Two types can be distinguished: older, inclusion-rich And1$_A$ porphyroblasts showing mosaic extinction in optical microscope are overgrown by an undeformed And2$_A$ generation where inclusions are not so variable (**Fig. 4a**). Sillimanite laths (Sil1$_A$), anhedral staurolite (St1$_A$), biotite (Bt1$_A$), spinel and corundum relics are preserved in the And1$_A$ generation. In contrast, biotite (Bt2$_A$) and quartz inclusions dominate in the And2$_A$ generation, staurolite may be present only as micrometer-sized late alteration product. In some cases, fibrous sillimanite (Sil2$_A$) is found in between And1$_A$ and And2$_A$ (**Fig. 4b**).

The St1$_A$ staurolite relics show the same optical orientation within one host andalusite grain and they are interconnected with cracks. St1$_A$ staurolite relics are always overgrown by c. 10 μm long, 2–5 μm wide staurolite laths (St2$_A$) showing different optical orientation and poikilitic appearance (**Fig. 4c**). Similar St2$_A$ staurolite overgrowths are found on spinel and on biotite inclusions in both And1$_A$ and And2$_A$ (**Fig. 4d**). Besides this, small St2$_A$ staurolite laths may also be found as individual inclusions along cracks of And1$_A$.

4.1.4. Mineral compositions

Feldspars

The composition of Kfs$_K$ K-feldspar (Ab$_{0.06–0.11}$Or$_{0.89–0.94}$) is homogenous and uniform in both samples regardless microstructural position (**Tab. 1**). Composition of plagioclase grains mostly depends on microstructural position, it does not show differences between the two samples. In general, all plagioclase grains are albitic. Pl1$_K$, contains the most anorthite component (Ab$_{0.79–0.85}$An$_{0.15–0.19}$Or$_{0.01–0.03}$) Pl2$_K$ is a bit more albite-rich (Ab$_{0.83–0.88}$An$_{0.12–0.17}$Or$_{0.00–0.01}$), while Pl3$_K$ feldspar lamellae in Kfs$_K$ K-feldspar contain the most albite component (Ab$_{0.90–0.98}$An$_{0.02–0.09}$Or$_{0.01}$). Some compositional variations within poikilitic Pl1$_K$ grains may be observed. The anorthite content may be slightly lower (X_{An}=0.13–0.14) in the core of grains containing only small Kfs$_K$ inclusions (**Tab. 1**). Right at the contact of Pl1$_K$ and its Kfs$_K$ inclusions, the albite content may increase suddenly to nearly 100% within 0.5−1 μm distance to form a 1–4 μm wide pure albite rim around the Kfs$_K$ K-feldspar inclusion.

Micas

Mica compositions are similar in both samples. Biotites in different microstructural positions show significantly different mg# and Ti-content (**Fig. 3e**, **Tab. 2**). Ti-rich biotites (X_{Ti} >0.3 p.f.u.) are found among microstructurally older generations as Bt1$_K$ biotite flakes as well as Bt1$_A$, Bt2$_A$ and Bt1$_G$ inclusions, while lower Ti-content (> 0.2 a.p.f.u.) is characteristic for younger biotites as Bt2$_K$ holding microstructural equilibrium with the outer rim of Grt1$_K$ and crack-filling Bt2$_G$. The highest mg# is shown by Bt2$_K$ biotites (>0.44) which appears as a separated group in **Fig. 3e** as well as crack-filling Bt2$_G$ characterized by the lowest mg# and Ti-content. The mg# of Ti-rich bitoties in different microstructural positions partly overlap, but the mg# of Bt1$_A$ inclusions in And1$_A$ and Bt1$_G$ inclusions in Grt$_G$ is definitely higher than the ones of Bt2$_A$ inclusions in And2 and Bt1$_K$.

Muscovite composition is quite uniform regardless microstructural position. Celadonite content is slightly higher in crack-filling Ms3$_K$ muscovites in Kfs-Sil-Pl-Bt-rich bands, similar to crack-filling Ms$_G$ (**Tab. 2**).

Garnet

All garnet generations are almandine-rich. However, they have different composition and they show different zoning trends. Grt1$_K$ garnets have spessartine-rich core (up to 0.15 p.f.u. Sps), while the rim has low Mn-content (**Fig. 2f**). From the core towards the rim the spessartine content is continuously decreasing parallel with the increase of mg# and almandine content, while the grossular content remains extremely low. The mg# reaches a maximum in 20–50 μm distance from the grain boundary, where St1$_K$ staurolite inclusions appear. From this point outwards the mg# is slightly decreasing, while the spessartine-content shows slight increase. Grt2$_K$ overgrowth on Bt1$_K$ has similar Mn-rich composition as the core of Grt1$_K$, while smaller garnets in equilibrium with Bt2$_K$ correspond to the Grt1$_K$ rim composition.

Grt$_G$ garnets show complex asymmetric compositional zoning (**Fig. 3b-c**, **Tab. 3**). In most cases, the inclusion-free core (Grt-I$_G$, Prp$_{0.07-0.08}$Alm$_{0.76-0.78}$Sps$_{0.05-0.09}$Grs$_{0.07-0.08}$) is surrounded by an Fe-rich zone (Grt-II$_G$, Prp$_{0.07-0.08}$Alm$_{0.78-0.80}$Sps$_{0.05-0.07}$Grs$_{0.06-0.07}$) containing large number of Bt1$_G$ inclusions, which continuously develops to a Mn-rich zone (Grt-III$_G$, Prp$_{0.06-0.08}$Alm$_{0.78-0.80}$Sps$_{0.07-0.15}$Grs$_{0.06-0.07}$). In contact with biotite within 10-20 micrometer distance from the grain boundary a fourth zone (Grt-IV$_G$, Prp$_{0.06-0.08}$Alm$_{0.75-0.79}$Sps$_{0.11-0.12}$Grs$_{0.02-0.08}$) may develop, which shows complex submicron scale chemical zoning perpendicular to the grain boundary (**Fig. 3g**).

The Grt-I$_G$ garnet cores show quite constant compositions (Grs-content varies between 7-8 %), with Ca-content slightly decreasing towards the Fe-rich Grt-II$_G$, but their boundary is not sharp (**Fig 3d)**. In some cases a decrease in Ca-content is observable within the core region, which may be interpreted as a low Ca inner core (**Fig. 3e**). However, overall Ca distribution in the grains clearly shows that the depletion in Ca is related to cracks (**Fig. 3b**).

The Fe-rich Grt-II$_G$ zone is typically not concentric and its width may vary from a few tens to hundreds of micrometres. The widest zones develop in the elongation directions of garnet (**Fig. 3f**) mostly parallel to the

schistosity of the sample. In general, Ca- and Mn-content continuously decreases while Fe-content increases from the garnet core towards the grain boundary (**Tab. 3**).
The Mn-rich Grt-III_G zone is found along the rims of Grt_G garnet porphyroblasts. The maximum width of Grt-III_G is found perpendicular to garnet elongation where the Grt-II_G is the narrowest. However, in most of the cases the boundary and connection of Grt-II_G and Grt-III_G is not well-defined. In general, Mn-content increases remarkably, while Fe-content decreases in Grt-III_G zone towards the grain boundary. The maximum value of Mn-content varies in a wide range (6-20 % Sps) from point to point along the grain boundary. However, the concentration changes along the grain boundary do not depend on the neighbouring phase (**Fig. 3c**). Extremely Mn-rich, mostly elongated subzones within Grt-III_G may be formed parallel to garnet elongation and schistosity. Both $Bt1_G$ and $Bt2_G$ inclusions and Ms_G muscovite as well are found within the Grt-III_G zone and their composition do not show systematic change compared to the inclusions in Grt-II_G zone. According to element distributions, garnet composition is frequently disturbed around biotite inclusions.

The Grt-IV_G garnet zone containing submicron sized ilmenite inclusions is restricted to contacts between $Bt1_K$ and Grt_G. Small scale chemical zoning was detected within this zone. The best developed example is shown in **Fig. 3g**. In general, a sudden drop of grossular content defines the zone boundary. According to element distributions, Ca minimum forms a straight line parallel to the grain boundary. Mn-content starts to decrease parallel with the increase of Fe within Grt-III_G zone 10-20 μm before the zone boundary. This trend holds until a Ca minimum is reached. Further outwards, grossular content increases fast within a few micrometres, which is accompanied by a drop in almandine content. Mn-content still keeps on decreasing. After the Ca peak, grossular content may drop again while almandine content is increasing. At the outermost 2-3 micrometres the composition stabilizes. Mg-content decreases slightly all along the Grt-III_G and Grt-IV_G zones.

Staurolite and oxides

Regarding composition, staurolite has two types. St1 staurolite appearing as relics in andalusite porphyroblasts contain representative amount of Zn (up to 0.149 p.f.u., **Tab. 4**). The composition of $St2_A$ staurolite laths grown on $St1_A$ staurolite is very similar. In contrast, $St2_A$ found as overgrowth on biotite or as small individual laths along cracks in andalusite as well as $St1_K$ and $St2_K$ staurolites in Kfs-Sil-Pl-Bt-rich bands have definitely lower Zn-content of (below 0.06 p.f.u.). The highest Mg-content was measured from $St1_K$ staurolite holding equilibrium with the rim of $Grt1_K$.

Oxides do not show compositional variations. Ilmenite is an ilmenite-rich ilmenite-hematite solid solution and it has the same composition appearing as inclusion in biotite and garnet as well. Zn-bearing spinels (X_{Zn} > 0.28 p.f.u.) are found as inclusions in $And1_A$ andalusite porphyroblasts (**Tab. 4**).

4.2. Whole rock composition

Major element compositions determined by ICP-OES from the average andalusite-sillimanite-biotite schist sample described in this study is similar to the compositions published by Kisházi and Ivancsics (1985) from the same locality. It is characterized by high Al_2O_3 and remarkable Fe_2O_3 content, while CaO content is extremely low (**Tab. 5**). This is close to the average metapelite composition of Symmes and Ferry (1991) or Mahar et al. (1997) but the CaO content is even lower.

4.3. Radiometric ages

In order to get better information on the timing of the pre-Alpine metamorphic evolution, garnet porphyroblasts were dated by the Sm-Nd method. As mentioned above, the Grt-I_G cores of the garnet porphyroblasts rarely contain inclusions, whereas all other zones are inclusion rich. This allowed us to separate grains from the central parts of the garnet from the 0.2 to 0.3 mm sized magnetic concentrate of the sample KA-1. A pure garnet fraction (Grt-C1), a garnet fraction with a few tiny intergrowths and inclusions (Grt-C2) and a whole rock powder were analyzed (**Tab. 6**). The whole rock contains c. 53 ppm Nd and c. 9.7 ppm Sm causing a $^{147}Sm/^{144}Nd$ ratio of c. 0.11 and a $^{143}Nd/^{144}Nd$ ratio of 0.511857 (corresponding to an ε_0 $Nd_{(Chur)}$ of −15.2). These ratios are in the typical range for metapelites of the Austroalpine unit (Schuster et al. 2001a; Thöni 2002). The pure garnet fraction Grt-C1 is characterised by a low Nd (c. 0.69 ppm) and higher Sm (c. 4.39 ppm) content corresponding to a remarkably high $^{147}Sm/^{144}Nd$ ratio (c. 3.87). The higher Sm and Nd contents (c. 5 ppm) and lower $^{147}Sm/^{144}Nd$ ratio (c. 0.53) of Grt-C2 can be explained by the contamination with minerals not enriched in HREE with respect to the whole rock. The isochron calculated from the three data points yielded an age of 330.4±2.7 Ma (**Fig. 5a**).

Additionally biotite and whole rock of the same sample were used to determine a Rb-Sr age. The $^{87}Rb/^{86}Sr$ ratio of the biotite (c. 400) proves the purity of the used biotite concentrate. The calculated age value is 187±2 Ma (**Tab. 7**; **Fig. 5b**).

4.4. Metamorphic reactions in different domains

In this chapter, the sequence of mineral reactions in different pre-Alpine domains of the Óbrennberg Micaschist is determined based on microstructural observations, mineral chemistry and radiometric ages. Following this, the reactions are correlated between the domains.

4.4.1. Kfs-Pl-Sill-Bt-rich bands

According to Török (1999), the majority of phases in Kfs-Pl-Sill-Bt-rich bands were formed during a high-temperature event. However, subdomains preserve different mineral reactions.

The precursor of cm-large poikiloblastic $Pl1_K$ plagioclase grains containing Kfs_K K-feldspar inclusions may have been a ternary feldspar crystallized from melt at the temperature maximum. However, the insignificant compositional difference between Kfs_K appearing as inclusion in $Pl1_K$ or as individual grains and the irregular distribution of Kfs_K in $Pl1_K$ suggests that both types were formed during the same high temperature event related to the decomposition of a presumed $Ms0_K$ muscovite generation. The formation of Kfs_K–Sil_K intergrowths could be the product of the local reaction:

$Ms0_K + Qtz \rightarrow Kfs_K + Sil_K + H_2O$.

The occurrence of albitic lamellae in Kfs_K indicates retrograde cooling:

$Kfs_K \rightarrow Kfs_K' + Pl3_K$

Partial or total rehydration led to the formation of new $Ms1_K$ muscovite at the expense of Kfs_K K-feldspar and $Bt1_K$ biotite presumably in the retrograde phase following the high temperature event. The growth of the most celadonite-rich $Ms3_K$ muscovite along cracks of $Bt1_K$ may be related to a later phase at elevated pressure.

The pure albite rim around Kfs_K in $Pl1_K$ is interpreted as a late metasomatic process:

$Pl1_K + 2Na^+(aq) \rightarrow Ab + Ca^{2+}(aq)$.

The formation of Ti-rich $Bt1_K$ biotites indicate high temperature as well. Moreover, the large number of ilmenite inclusions in $Bt1_K$ suggests that the Ti-content of $Bt1_K$ biotite was even higher at the temperature maximum and ilmenite was exsolved from $Bt1_K$ during cooling:

$Bt1_K \rightarrow Bt1_K' + Ilm$,

Ilmenite inclusions found in $Grt2_K$ growing at the expense of $Bt1_K$ indicate that the garnet formation postdated the temperature maximum. In $Grt1_K$ garnet-bearing subdomains, the garnet core may have formed at the same stage in equilibrium with $Bt1_K$. In contrast, the rim was formed in equilibrium with $St1_K$ staurolite and $Bt2_K$ biotite. The Mg-content of $Bt2_K$ biotite found as inclusions in the rim of $Grt1_K$ is lower than the Mg-content of $Bt2_K$ found in contact with $Grt1_K$. At the same time, the Mg-content of the rim of $Grt1_K$ decreases outwards, which suggests that staurolite, biotite and garnet were in equilibrium under changing conditions during the crystallization of the rim. Since the composition of $Bt2_K$ found in the matrix is uniform within the domain, it represents final equilibrium. This retrograde re-equilibration could affect muscovite composition as well. This explains insignificant compositional differences between large $Ms1_K$ muscovite and small, inclusion-free $Ms2_K$ muscovite both holding microstructural equilibrium with $Bt2_K$.

4.4.2. Garnet porphyroblasts

In the case of garnet porphyroblasts, the Grt-I_G core belongs to the oldest preserved mineral assemblage. The subsequent Fe-rich Grt-II_G zone was grown at the expense of, or in equilibrium with $Bt1_G$ biotite now found as inclusions within the garnet. The growth of the Mn-rich Grt-III_G garnet zone on the Fe-rich Grt-II_G zone may indicate a new garnet growth phase. However, asymmetric zoning character and diffuse zone boundaries shown by major element distributions (**Fig. 3b–f**) do not allow to distinguish the two growth phases from each other. In addition, $Bt1_G$ biotite inclusions in Grt-III_G do not show systematic change in composition compared to the ones in Grt-II_G. Well-defined even boundaries between Grt-III_G and Grt-IV_G indicate a break in garnet growth. If we try to redraw the garnet grain boundary at this period, it shows embayments in contact with $Bt1_K$, which is more Ti –rich and less magnesian than $Bt1_G$ (**Fig. 4e**). This suggests that $Bt1_K$ was consuming Grt-III_G, e.g. in the following reaction:

Grt-III_G + Qtz + Fluid $\rightarrow$ $Bt1_K$.

Observation of Grt-IV_G developing only at Ti-rich $Bt1_K$ biotite – Grt_G garnet contacts and the unique occurrence of ilmenite inclusion trails in Grt-IV_G suggest that this zone was formed by a local reaction:

Ti-Bt $\rightarrow$ Grt + Ilm + Qtz + Fluid.

The Ca-content of Grt-IV_G increases from <1 % Grs up to the highest measured values in the investigated garnet porphyroblasts (>8 % Grs), which suggests garnet growth due to pressure increase postdating the high temperature event.

4.4.3. Andalusite porphyroblasts

In this domain, the stages of the metamorphic evolution can be reconstructed from polymorphic transformations of aluminosilicates and subsequent reactions of $St1_A$ staurolite relics. $Sil1_A$ sillimanite laths found as inclusions in $And1_A$ andalusite (**Fig. 4a**) are interpreted to be the oldest aluminosilicate relics. Destabilization of $And1_A$ first resulted in the growth of mostly fibrolitic $Sil2_A$ sillimanite (**Fig. 4b**), which was followed by the formation of $And2_A$ andalusite by postdeformative recrystallization of $And1_A$.

$St1_A$ is interpreted as the precursor of hosting $And1_A$. $St1_A$ was first destabilized together with a presumed $Ms0_A$ muscovite generation, which should have been consumed by the reaction:

$St1_A + Ms0_A + Qtz \rightarrow And1_A + Bt1_A + H_2O$ (Török 1999).

Growth of poikilitic $St2_A$ staurolite laths containing white mica and quartz inclusions on $St1_A$ and slightly lower Zn-content of $St2_A$ implies that later staurolite became stable again by the local reaction:

$Bt + And1_A + Fluid \rightarrow St2_A + Wmca + Qtz$.

Although the Zn-content of $St2_A$ staurolite laths grown on staurolite relics is higher, than the ones grown on spinel as well as on both $Bt1_A$ and $Bt2_A$ biotites, the similar microstructural appearance and inclusion content suggests that all $St2_A$ staurolite laths were formed in the same fluid-assisted reaction following the entrapment of $Bt2_A$ biotites in $And2_A$. Variations of Zn-content indicate differences in locally available Zn sources.

4.4.4. Correlation of the domains

Different mineral assemblages and reactions in all domains are classified to three main events. Stage1 preceded the high temperature event, referred to as Stage2, while Stage3 postdated Stage2.

The formation of high temperature minerals in Kfs-Sil-Pl-Bt-rich bands, such as Ti-rich $Bt1_K$, fibrolitic Sil_K sillimanite and K-feldspar are all related to the temperature peak in Stage2. The presumed muscovite precursor of K-feldspar and part of the plagioclase are the only phases in this domain, which may existed prior to the temperature peak.

In garnet porphyroblasts, inclusion-free Variscan Grt-I_G cores represent the oldest phase. Since $Bt1_K$ grows at the expense of Grt-III_G the destabilization of garnet porphyroblasts should be related to Stage2. Therefore the Grt-I_G core represents Stage1 and the Grt-III_G garnet zone should have formed latest at the beginning of Stage2. Grt-IV_G replaces $Bt1_K$ and therefore postdates the high temperature event as it is seen in the case of $Grt2_K$, which shows similar composition. According to composition and garnet zoning trends, $Grt2_K$ corresponds to the core of $Grt1_K$. Therefore all of these garnets are correlated to the same event postdating Stage2.

The correlation in andalusite porphyroblasts is the most difficult since only the youngest $And2_A$ aluminosilicate generation contacts with other domains. According to previous studies (e.g. Kisházi and Ivancsics 1987b; Török 1999) the last sillimanite forming event in the metamorphic history was a Permo-Triassic high temperature low pressure event. Therefore $Sil2_A$ sillimanite fibres are correlated with Sil_K sillimanite in Kfs-Pl-Sil-Bt-rich layers formed in Stage2, while $Sil1_A$ is assigned to Stage1. The formation of $And1_A$ at the expense of $St1_A$ should take place between the two temperature peaks.

These imply that cores of garnet porphyroblasts (Grt-I_G and Grt-II_G), $Bt1_G$ biotite, $Sil1_A$ sillimanite, $St1_A$ staurolite and $Pl1_K$ plagioclase found in the KA-6 sample are remnants of the mineral assemblage formed during peak conditions of Stage1. According to the observed mineral reactions, muscovite should have been part of this assemblage as well. The high temperature event in Stage2 resulted in the $Bt1_K$ biotite, $Pl1_K$ plagioclase, K-feldspar, sillimanite ± melt assemblage which was preserved in Kfs-Pl-Sil-Bt-rich layers in both samples. The mineral assemblage formed in Stage3 includes $Grt1_K$ garnet, $St1_K$ staurolite $Bt2_K$ biotite, $Ms2_K$ muscovite and $Pl2_K$ plagioclase as preserved in the KA-10 sample. Quartz is present in all assemblages.

4.5. Phase equilibria modelling

In order to study the formation conditions of different mineral assemblages, P−T phase diagram sections were calculated for the compositions listed in **Tab. 5** in the MnNCKFMASH system using the PERPLEX software package (Connolly 2009) and the database of Holland and Powell (1998). Solution models used were garnet, cordierite, chloritoid, orthopyroxene and staurolite from Holland and Powell (1998), biotite from Tajcmanova et al. (2009), high temperature feldspar from Fuhrman and Lindsley (1988), low temperature feldspar from Newton et al. (1980), sanidine from Waldbaum and Thompson (1968) and white mica from Coggon and Holland (2002).

4.5.1. Stage1 mineral assemblage

Based on microstructural observations and mineral chemistry we assumed that the amount of melt formed in the KA-6 sample during the high temperature event in Stage2 should not be large and most probably it was in situ crystallized in the rock. In addition, there is no evidence for the late infiltration of metasomatic fluids which could significantly modify the bulk chemistry. Therefore, the ICP-OES bulk composition shown in **Tab. 5** should be representative for the Variscan bulk chemistry of the rock. In order to check this concept, the phase diagram section was calculated for this composition (**Fig. 6a**). Since only subsolidus reactions occurred in Stage1, water was treated as saturated component. We compared the measured mineral chemistry of the Stage1 mineral assemblage found in KA-6 and the phase compositions predicted by the P−T section (**Fig 6b−c**). The peak metamorphic assemblage of garnet, staurolite, biotite, plagioclase and muscovite is stable in a narrow field between 550−650 °C and 0.30−0.65 GPa. The mg# of staurolite decreases with pressure and temperature from 0.16 to 0.11, while the measured staurolite mg# is between 0.15−0.16. The anorthite content of plagioclase in the staurolite field increases with decreasing pressure and temperature from 0.11 below 0.15 p.f.u. The measured plagioclase compositions are variable. In grains which are microstructurally separated from Kfs-Pl-Sil-Bt-rich assemblages, it changes between 0.13-0.16 p.f.u., while in the high temperature assemblages it is higher 0.18-0.19 p.f.u. As shown by the P−T diagram, the spessartine content of garnet is significantly increasing with decreasing pressure and temperature from 0.02 to 0.10 p.f.u., while the mg# of garnet basically does not change. This is in accordance with the observed garnet zoning trend of Grt-I_G and Grt-II_G zones (**Fig. 3**). According to this, the P−T section shown in **Fig. 6** describes well the peak metamorphic assemblage formed in Stage1 and the retrograde zoning trend of garnet shown by solid arrow on **Fig 6a**. Since $Sil1_A$ sillimanite laths were found within $And1_A$, the suggested arrow may run closer to the upper temperature limit of the staurolite stability field. However, significant Zn-content of staurolite may expand the staurolite-sillimanite field to somewhat lower temperatures as well. Following this path staurolite destabilizes to form andalusite and biotite as observed in the thin section at around 570 °C and 0.37 GPa. The absence of cordierite in the samples indicates that the pressure was higher than 0.35 GPa. Further isobaric heating between 0.35-0.37 GPa above 620 °C may explain the compositional zoning trend observed in Grt-III_G with the spessartine content increasing above 0.16 p.f.u. as well as intense andalusite growth. This temperature increase should reflect the early prograde part of the Stage2 high temperature event.

4.5.2. Stage2 mineral assemblage

During Stage2, Grt-I_G and Grt-II_G zones of garnet porphyroblasts formed in Stage1 did not react. Therefore a new bulk (P in **Tab. 5**) was derived from the whole rock composition by extracting the average composition of old garnet relics (which is determined as the average of the Grt-I_G core composition and the representative Grt-II_G composition) weighted by their modal proportion (c.a. 1 wt%).

Since there is evidence in the Stage2 high temperature assemblage that melt was produced, water was treated as a constrained component during calculation. The amount of H_2O component involved in the calculation for the bulk rock composition was assumed as the loss of ignition of the XRF analysis.

According to the resulting P–T diagram (**Fig. 7**), the peak metamorphic assemblage containing Bt, Kfs, Pl, Sil is stable from c.a. 640 °C, 0.3 GPa towards higher pressures and temperatures as indicated by the blue field in **Fig. 7b**. If we take into consideration that cordierite is absent from the rock, the lower pressure limit increases to 0.37 GPa. Since there is petrographic evidence for the growth of $Bt1_K$ at the expense of garnet, i.e. consumption of garnet by the biotite-plagioclase-K-feldspar-sillimanite assemblage, the stability field of the peak metamorphic assemblage significantly reduces to 650–680 °C, 0.37–0.47 GPa (orange field in **Fig. 7b**). According to the spessartine isopleths shown on **Fig. 7c**, the Mn-concentrations measured at the rims of garnet porphyroblasts (higher than 0.12 p.f.u. Sps) would fit better to isobaric heating close to the lower pressure limit, around 0.4 GPa. According to phase equilibria modelling melt is produced during isobaric heating from 650 °C onward. Isobaric cooling around 0.4 GPa in the retrograde path of Stage2 allows for rehydration reactions, such as the replacement of K-feldspar by muscovite observed frequently in the samples. This suggest that most of the melt produced was in situ crystallized during the retrograde path. Therefore the bulk composition change due to melt loss in Stage2 should not be significant as it was assumed previously. The formation of andalusite corresponding to the And2 generation occurs between 590–570 °C on this path.

4.5.3. Stage3 mineral assemblage

For the KA-10 sample, where Stage3 garnet and staurolite is found, a new bulk was calculated from the whole rock composition (A in **Tab. 5**). Since garnet porphyroblasts are absent from the thin section and $And1_A$ containing Variscan $St1_A$ staurolite relics has only minor late modification, the composition of all Stage1 relics weighted by their modal amount measured in other samples (1-1 wt% for garnet and andalusite porphyroblasts and 0,1 wt% for staurolite) was deduced from the whole rock composition. Water was treated as saturated component.

Based on the phase diagram section calculated between 450–650 °C and 0.1–1.1 GPa (Online Resource 1), the Stage3 garnet, plagioclase, biotite, staurolite, muscovite mineral assemblage is stable in a narrow field (560–660 °C, 0.33–0.62 GPa, shown in detail in **Fig. 8**). According to the garnet isopleths shown in **Fig. 8a**, such Mn-rich garnet as $Grt2_K$ or the core of $Grt1_K$ (**Fig. 2e–f**), not containing staurolite and showing intense decrease of spessartine content from 0.14 to about 0.10 p.f.u. may have formed by isobaric cooling around 0.4 GPa, most probably in the retrograde phase of Stage2. Further decrease of spessartine content from about 0.10 to 0.06 p.f.u. together with the increase of mg# from 0.13 to 0.16 and the Grs-content remaining constant around 0.01 p.f.u. suggest compression from 550 °C, 0.36 GPa to a maximum of 640 °C, 0.65 GPa. Based on mg# isopleths of garnet, biotite and staurolite showing microstructural equilibrium (**Fig. 8b–c**), the crystallization of the staurolite-bearing assemblage took place close to the peak conditions (680 °C, 0.60 GPa). The decrease of mg# in later biotite and staurolite generations indicates retrograde cooling.

4.6. Geothermobarometry

Garnet-biotite thermometry was carried out assuming local equilibria between garnet porphyroblasts and their inclusions, and contacting garnet-biotite pairs. Seven calibrations of the thermometer were tested. Temperatures derived from the calibration of Battacharya et al. (1992) are discussed here.

Biotite inclusions in Grt-II_G and Grt-III_G zone of garnet porphyroblasts give confusing results. Estimated temperatures vary between 460–580 °C. However, they do not show systematic change with distance from garnet core or any compositional changes in garnet. This suggests that garnet zoning is not simply the result of crystallizing under varying PT conditions. According to element distributions, garnet composition is frequently modified in relatively wide halos around cracks (**Fig. 3b**).

Temperatures calculated for the rim of $Grt1_K$ in equilibrium with its $Bt2_K$ inclusions and contacting $Bt2_K$ biotite grains show continuous decrease towards the rim from 600 °C to 540 °C corresponding to the Alpine retrograde cooling, which is in accordance with the P−T estimates from thermodynamic modelling. Rim compositions of $Bt1_K$ in contact with $Grt\text{-}IV_G$ as well as with $Grt2_K$ garnet overgrowths give temperatures scattering around 500 °C. Compositional zoning within $Bt1_K$ towards $Grt\text{-}IV_G$ indicates that Fe-Mg exchange between garnet and biotite was continuous during cooling. Therefore the estimated temperature was preserved from the latest retrograde phase. Based on this, peak temperature of 600 °C in Stage3 and subsequent retrograde cooling to 500 °C is also detected. This corresponds well with temperatures estimated for the Alpine phase in earlier works (e.g. Török 2003).

5. Discussion

In this chapter we first discuss the relations of the Óbrennberg Micaschist to other Austroalpine units in order to highlight the timing of tectonometamorphic events affecting the Óbrennberg Micaschist. Following this, we set up the sequence of mineral reactions in the different pre-Alpine domains and correlate processes and mineral parageneses between the domains. We combine this with mineral stabilities derived from thermodynamic modelling, thermobarometry and radiometric ages in order to construct the metamorphic history of the studied andalusite-biotite-sillimanite schist.

5.1. Relations of the Óbrennberg Micaschist to other Austroalpine units

As mentioned above, Draganits (1998) subdivided the polymetamorphic rocks of the Sopron area into the Óbrennberg-Kaltes Bründl series (Óbrennberg Micaschist) correlated with the Strallegg Complex and the Sopron series, which was linked to the Grobgneiss unit. In fact, very similar andalusite-biotite-sillimanite schist occurs in the Strallegg-Complex which build up the Rabenwald Nappe in Styria/Austria (Matura and Schuster, 2014; Schuster and Nowotny, 2015) (**Fig. 1**). In the Traibach- and Freßnitz valley south of Mürzzuschlag (**Fig. 1**) the pre-Alpine mineral assemblage is well preserved, whereas in the area around Hartberg and Strallegg (**Fig. 1**), andalusite and sillimanite are totally replaced by Alpine kyanite, even if the pre-Alpine microstructures are nearly unaffected in some rock types. However, the Rabenwald Nappe also includes rock series similar to the Sopron series which are rich in orthogneiss with Permian intrusion ages (Schuster et al. 2010). This is in line with the interpretation of Török (2003) who suggested that the Óbrennberg Micaschist and the Sopron series are part of a single Alpine nappe - the Rabenwald Nappe - because they share the same Alpine metamorphic history.

The Rabenwald Nappe is overlying the Stuhleck-Kirchberg Nappe (**Fig. 1**). The latter is characterised by huge masses of porphyric orthogneiss embedded in phyllonitic micaschist. This orthogneiss referred to as “Grobgneiss” in the literature is problematic, because the main part is developed from Permian granite, whereas others formed from Ordovician intrusions. For this reason the former Grobgneiss unit was subdivided into a part with Permo-Mesozoic metasediments and a basement with Ordovician intrusives belonging to the Lower Austroalpine unit and a main part representing the Stuhleck-Kirchberg Nappe with the Permian intrusive rocks (Froitzheim et al. 2008; Schuster and Nowotny 2015). In the southwestern part of the Sopron area porphyric orthogneiss similar to the Permian one occurs. Therefore this part is attributed to the Stuhleck-Kirchberg Nappe in **Fig. 1**.

5.2. Timing of metamorphism

The Sm-Nd garnet age of 330.4±2.7 Ma (**Fig. 5a**) indicates the formation of the first garnet-bearing mineral assemblage during a Variscan tectonometamorphic event. This age is in line with a Sm-Nd garnet age from a very similar lithology of the Strallegg Complex from the Traibach valley south of Mürzzuschlag. The age of 320.6±1.5 Ma (Berka 2000) is calculated just from the whole rock and one garnet fraction. Also the Th-U monazite ages from the Sopron area (Nagy et al. 2002) and from the Strallegg Complex near to Stubenberg (Bernhard et al. 2000) are in the range of 300 to 330 Ma.

All previous studies on andalusite-sillimanite-biotite schist have shown that the rock experienced a low pressure, high temperature event (Lelkes-Felvári et al., 1984; Kisházi and Ivancsics, 1987b; Draganits, 1998; Török, 1999). Concerning its timing, data from the Austroalpine unit are in the range of 290 to 240 Ma (Thöni 2002; Schuster and Stüwe 2008) indicate a Permian to Triassic age. Beside a few Sm-Nd ages of garnets and Rb-Sr ages of muscovites (Schuster et al. 2001b) the Permian intrusion ages of granites in the southern part of the Strallegg Complex north of Stubenberg (Schuster et al. 2010) have to be taken into consideration.

As mentioned in the regional geology chapter, the Alpine imprint in the Sopron area occurred in the Late Cretaceous and cooling of the rocks lasted until the late Eocene (Balogh and Dunkl, 2005). This interpretation fits the data from other occurrences of the Rabenwald Nappe and Stuhleck-Kirchberg Nappe further in the west.

The Rb-Sr biotite age from sample KA-1 presented in this paper is in accordance with other scattered Rb-Sr, Ar-Ar and K-Ar data from the Óbrennberg Micaschist. Even though these ages were obtained from the best preserved pre-Alpine assemblages which were not affected by Alpine deformation and fluid interaction, we interpret these values as geological meaningless due to incomplete reset of the Rb-Sr isotopic system even at high temperatures or due to excess Ar in rocks.

5.3. P−T evolution of metamorphic rocks from Sopron area

According to refined microstructural observations combined with mineral chemistry, geothermobarometry and thermodynamic modelling we could clearly distinguish three stages of metamorphic evolution (**Fig. 9**). The results of radiometric age dating in this study provided evidence that Stage1 and Stage2 record Variscan and Permo-Triassic tectonometamorphic events in the Óbrennberg Micaschist, whereas 71–75 Ma Ar/Ar and K/Ar ages of white mica from Kovács-árok (Balogh and Dunkl 2005) indicate that Stage3 is related to the Alpine tectonometamorphic event.

5.3.1. Stage1: Variscan metamorphism

According to our results, Ca-rich Grt-I_G cores of garnet porphyroblasts are the oldest preserved Variscan relics formed ca. 330 Ma. Török (1999) reported a low Ca inner core within garnet porphyroblasts and estimated 650–700 °C, 0.18–0.38 GPa as the oldest equilibration conditions. However, thermodynamic modelling have shown that cordierite should have been present at such low pressures, which is not the case. In addition, our observations on element distributions in garnet porphyroblasts (**Fig. 3b–f**) have shown that the garnet composition is modified in wide halos surrounding cracks which could be falsly interpreted as low Ca inner cores in some sections.

Based on geothermobarometry using Ca-rich Grt-I_G garnet cores and related biotite and plagioclase inclusions, Török (1999) estimated the equilibration conditions of the pressure peak to be 605–660 °C, 0.67–0.89 GPa. In the samples we studied, we could not find mineral inclusions sufficient for these calculations, but the estimates of Török (1999) could fit in the $P–T$ path we suggested (**Fig. 9**). Phase equilibria and isopleths shown in **Fig. 6**, calculated for the Variscan stage indicates that Fe-rich Grt-II_G zones of the garnet porphyroblasts could hold equilibrium with its $Bt1_G$ biotite inclusions, $St1_A$ staurolite, muscovite, quartz and feldspar between 550-650 °C and 0.4–0.6 GPa in the early retrograde path of the Variscan tectonometamorphic cycle. Further decompression and cooling below 570 °C 0.37 GPa and/or the subsequent Permo-Triassic isobaric heating led to the formation of $And1_A$ porphyroblasts, and $Bt1_A$ type biotite. Zn-rich spinel and corundum inclusions in $And1_A$ should have been formed during the same process due to local reactions in SiO_2 undersaturated conditions and does not necessarily indicate pressure decrease as suggested by Török (1999).

5.3.2. Stage2: Permo-Triassic high temperature event

The beginning of nearly isobaric heating between 0.35-0.37 GPa above 620 °C during the Permo-Triassic phase first resulted in increasing spessartine content in Grt-III_G than the destabilization of garnet. Further nearly isobaric temperature increase above 640 °C resulted in the decomposition of Variscan muscovite and formation of K-feldspar and melt. The majority of the mineral assemblage of the Kfs-Pl-Sil-Bt-rich bands preserved the peak metamorphic conditions 650–680 °C, c.a. 0.4 GPa. This corresponds to the PT conditions estimated by Draganits (1998), indicated in **Fig. 9**. However, it must be noted that based on thermodynamic modelling (**Fig. 7**) the absence of cordierite from the andalusite-sillimanite-biotite schist together with the measured high Mn-content of garnet defines much narrower pressure limits. During isobaric cooling around 0.4 GPa ilmenite exsolved from high temperature $Bt1_K$ biotite, local rehydration caused by the in situ crystallizing melt led to the formation of new muscovite and the formation of $And2_A$ andalusite generation took place between 590–570 °C.

5.3.3. Stage3: Alpine metamorphism

The Alpine metamorphic overprint in the andalusite-sillimanite-biotite schists is usually present in local reactions forming micrometre to submicrometre sized reaction products. This study reports zoned garnets preserving the complete P–T path from the Permo-Triassic retrograde phase through the Alpine pressure peak and the early retrograde path for the first time from this rock type. According to phase equilibria modelling shown in **Fig. 8**, the prograde path of the Alpine cycle was characterized by compression from 550 °C, 0.36 GPa to a maximum of 640 °C, 0.65 GPa recorded by chemical zoning of $Grt1_K$ core (**Fig. 2f**). From the changes of spessartine content in garnet we could relate the formation of garnet Mn-rich overgrowths on $Bt1_K$ biotite (such as $Grt2_K$ or Grt-IV_G) to the Permo-Triassic retrograde path. The characteristic Mn-poor garnet-staurolite-biotite-muscovite-plagioclase mineral assemblage was formed at the Alpine prograde path close to the metamorphic peak (640 °C, 0.60 GPa) and remained stable during retrograde cooling down to 560 °C, 0.35 GPa. Staurolite laths formed in local reactions within andalusite porphyroblasts and Kfs-Pl-Sil-Bt-rich bands should be related to this phase as well. Further cooling to 500 °C is shown by garnet-biotite thermometry.

The estimated Alpine $P–T$ path shows significantly lower pressure and slightly higher temperature than the one determined from kyanite-staurolite-chloritoid-garnet bearing micaschist found also within Óbrennberg Micaschist (patterned arrow in **Fig. 9**, Török 2003). Based on relic minerals and microstructures, this rock type is assigned to be the Alpine overprinted variety of the studied andalusite-sillimanite-biotite schist (Török 2003). As it is inferred from phase equilibria modelling using the measured (Variscan) bulk chemistry of the studied sample in the P–T range extended to 0.1–1.1 GPa and 450–700 °C (see Online Resource 1), this rock chemistry does not allow for the crystallization of kyanite and chloritoid even at very high pressure and low temperature. In addition, the observed garnet zoning trend as well as the presence of staurolite in the mineral assemblage is not compatible with high pressure metamorphism. Although the two rock types occur in the field quite close to each other, our observations have clearly shown that andalusite-sillimanite-biotite schist did not experience the

Alpine high pressure metamorphism with peak conditions between 1.3–1.4 GPa at 550–600 °C (Török, 2003) as the kyanite-staurolite-chloritoid-garnet bearing micaschist or rocks of the Sopron series (0.8–1.1 GPa at 520–580 °C, Draganits 1998; or 1.0–1.2 GPa at 550–600 °C Török, unpublished data).

According to the whole rock data of Kisházi and Ivancsics (1985), the bulk rock composition of the two rock types differ significantly from each other especially in SiO_2, Al_2O_3 and FeO content. Therefore the transformation of andalusite-sillimanite-biotite schist to kyanite-staurolite-chloritoid-garnet bearing micaschist requires significant change in bulk chemistry, such as metasomatism, melt infiltration or extraction. These processes may cause significant local pressure variations. In addition, the preservation of metastable medium pressure assemblages in the andalusite-sillimanite-biotite schists at higher pressures may be easier in the absence of fluids. As it was mentioned above, similar feautres are observed in the Rabenwald Nappe. The fact that some lithologies did not experience Alpine high pressure metamorphism could explain why pre-Alpine mineral assemblages are preseved uniquely in some rock types. However, this observation opens new questions for the tectonic interpretation of the Sopron area and the Austroalpine units as a whole.

6. Conclusions

Submicrometre scale petrography, main element zoning patterns, garnet Sm-Nd ages and mineral stabilities were studied in polymetamorphic andalusite-sillimanite-biotite schist from the Óbrennberg Micaschist from the Sopron area. This is the first study where the existence of ca. 330 Ma Variscan mineral relics in the rock is proved by Sm-Nd age determination. This gives direct evidence for the existence of two pre-Alpine tectonic phases, which was a question of debate in earlier works. Different mineral generations in Kfs-Pl-Sil-Bt-rich bands, garnet and andalusite porphyroblasts were correlated to each other and distinguished to be formed in three stages correlated with Variscan, Permo-Triassic and Alpine tectonic phases, which clarified some discrepancies and contradictions regarding the P-T history of the rocks published in earlier studies.

From microstructural observation combined with phase equilibria modelling we concluded that the Variscan peak was achieved in the garnet-sillimanite stability field at 330 Ma. This was followed by decompression and cooling to 550−650 °C and 0.4−0.6 GPa to form Variscan staurolite, which was decomposed to andalusite and biotite below 570 °C 0.37 GPa. In the Permo-Triassic phase near isobaric heating at ca. 0.4 GPa to the temperature peak between 650−680 °C resulted in the destabilization of andalusite and garnet and the formation of a K-feldspar-sillimanite-biotite-plagioclase-melt mineral assemblage. This was followed by isobaric cooling leading to rehydration due to in situ melt crystallization and the formation of the second andalusite generation between 590−570 °C. Nearly isothermal compression in the Alpine prograde path from 580 °C, 0.36 GPa to a maximum of 680 °C, 0.65 GPa was followed by retrograde decompression and cooling in the staurolite stability field down to 560 °C, 0.35 GPa.

Based on microstructural observations and timing of metamorphism we could correlate Óbrennberg Micaschist to the Rabenwald Nappe in Styria/Austria. We have shown clear evidence that andalusite-sillimanite-biotite schist from the Óbrennberg Micaschist did not experience high pressure Alpine metamorphism (with peak pressures above 1.0 GPa) as the surrounding kyanite-staurolite-chloritoid-garnet bearing micaschist or rocks of the Sopron series. Similar feature is also observed in the Rabenwald Nappe, which arises questions on the tectonic evolution of the area.

Acknowledgements. The project was financed by the Hungarian National Research, Development and Innovation Office (grant nr. OTKA PD 104692) and the Bolyai János Research Scholarship donated to Júlia Dégi. The authors highly appreciate the help of Kálmán Török in establishing the sample set and the fruitful conversations about the material which highly improved this study. We thank the help of Adrienn Menyhárt at MTA-ME Materials Science Research Group and Eric Reusser at ETH Zürich during electron beam microanalytical work. Monika Horschinegg from the Department of Lithospheric Research at the University of Vienna is acknowledged for the help with isotopic measurements.

References

Balogh K, Dunkl I (2005) Argon and fission track dating of Alpine metamorphism and basement exhumation in the Sopron Mts. (Eastern Alps, Hungary): thermochronology or mineral growth? Mineral Petrol 83(3−4):191−218. doi: 10.1007/s00710-004-0066-0

Battacharya A, Mohanty L, Maji A, Sen SK, Raith M (1992) Non-ideal mixing in the phlogopite-annite binary: constraints from experimental data on Mg−Fe partitioning and a reformulation of the biotite-garnet geothermometer. Contrib Mineral Petrol 111(1):87−93. doi: 10.1007/BF00296580

Berka R (2000) Zur Stellung der Traibachschiefer im Semmering–Wechsel–System. – MSc Thesis, Universität Wien

Bernhard F, Finger F, Schitter F (2000) Timing of metamorphic, magmatic, hydrothermal and deformational events revealed by EMP total Pb dating of monazite and xenotime in the polymetamorphic Austroalpine Grobgneis complex, Eastern Alps, Styria, Austria. - Abstracts Volume, 31st International Geological Congress, Rio de Janeiro, Brazil. Session 18-3, Rio de Janeiro 2000

Coggon R, Holland TJB (2002): Mixing properties of phengitic mica and revised garnet-phengite thermobarometers. J Metamorph Geol 20:683−696. doi: 10.1046/j.1525-1314.2002.00395.x

Connolly JAD (2009) The geodynamic equation of state: what and how. Geochem Geophys 10(10):Q10014 doi:10.1029/2009GC002540.

Demény A, Sharp ZD, Pfeiffer HR (1997) Mg-metasomatism and formation conditions of Mg-chloritemuscovite-quartzphyllites (leucophyllites) of the Eastern Alps (W Hungary) and their relations to Alpine whiteschists. Contrib Mineral Petrol 128(2−3):247−260. doi: 10.1007/s004100050306

Draganits E (1998) Two crystalline series of the Sopron Hills (Burgenland) and their correlation to the lower Austroalpine in Eastern Austria. Jb Geol B-A 141(2):113−146.

Fuhrman ML, Lindsley DH (1988) Ternary-feldspar modeling and thermometry. Amer Miner 73:201–215.

Froitzheim N, Plasienka D, Schuster R (2008) Alpine tectonics of the Alps and Western Carpathians. In: McCann T (ed) The geology of Central Europe. Geological Society, London, pp 1141–1232

Holland TJB, Powell R (1998) An internally consistent thermodynamic data set for phases of petrological interest. J Metamorph Geol 16:309–343. doi: 10.1111/j.1525-1314.1998.00140.x

Kisházi P, Ivancsics J (1985) Genetic petrology of the Sopron crystalline schist sequence. Acta Geol Hung 28:191−213.

Kisházi P, Ivancsics J (1987a) Contribution to the problematics of the origin of leuchtenbergite-bearing metamorphics in the Sopron area. Földt Közl 117:31−45.

Kisházi P, Ivancsics J (1987b) Genetic petrology of the Sopron Micaschist Formation. Földt Közl 117:203−221.

Kisházi P, Ivancsics J (1989) Petrogenesis of the Sopron Gneiss Formation. Földt Közl 119:153−166.

Lelkes-Felvári Gy, Sassi FP, Visoná D (1984) Pre-Alpine and Alpine developments of the Austridic basement in the Sopron area (Eastern Alps, Hungary). Rend Soc It Mineral Petrol 39:593–612.

Ludwig KR (2001) Isoplot/Ex version 2.49. A Geochronological toolkit for Microsoft Excel. Berkeley Geochronology Center Special Publication 1a.

Ludwig KR (2003) Isoplot/Ex version 3.0. A geochronological toolkit for Microsoft Excel. Berkeley Geochronological Centre Special Publication 4.

Mahar EM, Baker JM, Powell R, Holland TJB, Howell N (2004) The effect of Mn on mineral stability in metapelites. J Metamorph Geol 15(2):223−238. doi: 10.1111/j.1525-1314.1997.00011.x

Matura A, Schuster R (2014): Geologische Karte der Republik Österreich 1:50.000, Blatt 135 Birkfeld. – Geol B-A Wien

Nagy B, Draganits E, Demény A, Pantó Gy, Árkai P (2002) Genesis and transformations of monazite, florencite and rhabdophane during medium grade metamorphism: examples from the Sopron Hills, Eastern Alps. Chem Geol 191:25–46. doi: 10.1016/S0009-2541(02)00147-X

Newton RC, Charlu TV, Kleppa OJ (1980) Thermochemistry of the high structural state plagioclases. Geochim Cosmochim Acta 44:933–41. doi: 10.1016/0016-7037(80)90283-5

Schmid SM, Fügenschuh B, Kissling E, Schuster R (2004) Tectonic map and overall architecture of the Alpine orogen. Eclogae Geol Helv 97/1:93−117. doi: 10.1007/s00015-004-1113-x

Schuster K, Berka R, Draganits E, Frank W, Schuster R (2001b) Lithologien, Metamorphosegeschichte und tektonischer Bau der kristallinen Einheiten am Alpenostrand. Arbeitstagung der Geologischen Bundesanstalt Blatt 104 Mürzzuschlag, Neuberg a.d. Mürz 3.-7. September 2001: 29−56

Schuster R, Nowotny A (2015) Die Einheiten des Ostalpinen Kristallins auf den Kartenblättern GK50 Blatt 103 Kindberg und 135 Birkfeld. Arbeitstagung der Geologischen Bundesanstalt Geologie der Kartenblätter GK50 ÖK 103 Kindberg und ÖK 135 Birkfeld, Mitterdorf im Mürztal 21.–25. September 2015:10−37.

Schuster R, Rockenschaub M, Klötzli U, Nowotny A, Grösel K (2010): In-situ laser ablation zircon U-Pb ages on granitic rocks from the eastern margin of the Eastern Alps: implications for the tectonic and

lithostratigraphic subdivision. – Journal of Alpine Geology, Abstract Volume PANGEO 2010 Leoben, 52: 228.
Schuster R, Scharbert S, Abart R, Frank W (2001a) Permo-Triassic extension and related HT/LP metamorphism in the Austroalpine – Southalpine realm. Mitt Ges Geol Bergbaustud Österr 44:111−141.
Schuster R, Stüwe K (2008):The Permian Metamorphic Event in the Alps. Geology 36(8):303–306. doi: 10.1130/G24703A.1
Sölva H, Grasemann B, Thöni M, Thiede R, Habler G (2005) The Schneeberg Normal Fault Zone: Normal faulting associated with Cretaceous SE-directed extrusion in the Eastern Alps (Italy/ Austria). Tectonophysics 401:143−166. doi: 10.1016/j.tecto.2005.02.005
Symmes GH, Ferry JM (1991) Evidence from mineral assemblages for infiltration of pelitic schists by aqueous fluids during metamorphism. Contrib Mineral Petrol 108:419−438. doi: 10.1007/BF00303447
Tajčmanová L, Conolly JAD, Cesare B (2009) A thermodynamic model for titanium and ferric iron solution in biotite. J Metamorph Geol 27:153–165. doi: 10.1111/j.1525-1314.2009.00812.x
Thöni M (2002): Sm-Nd isotope systematics in garnet from different lithologies (Eastern Alps): age results, and an evaluation of potential problems for garnet Sm-Nd chronometry. Chem Geol 185:255–281. doi: 10.1016/S0009-2541(01)00410-7
Török K (1996) High-pressure/low-temperature metamorphism of the Kő-hegy gneiss, Sopron (W-Hungary); Phengite barometry and fluid inclusions. Eur J Mineral 8(5):917−925. doi: 10.1127/ejm/8/5/0917
Török K (1998) Magmatic and high-pressure metamorphic development of orthogneisses in the Sopron area, eastern Alps (W-Hungary). Neu Jb Mineral Abh 173(1):63−91. doi: doi:10.1127/njma/173/1998/63
Török K (1999) Pre-Alpine development of the andalusite-sillimanite-biotite-schists from the Sopron Mountains Eastern Alps, Western Hungary. Acta Geol Hung 42:127–160.
Török K (2001) Multiple fluid migration events in the Sopron Gneisses during the Alpine high-pressure metamorphism, as recorded by bulk-rock and mineral chemistry and fluid inclusions Neu Jb Mineral Abh 177(1):1−36. doi: doi: 10.1127/007777502753418566
Török K (2003) Alpine P-T path of micaschists and related orthogneiss veins near Óbrennberg (W-Hungary, Eastern Alps). Neu Jb Mineral Abh 179(2):101−142. doi: 10.1127/0077-7757/2003/0179-0101
Waldbaum DR, Thompson JB (1968) Mixing Properties Of Sanidine Crystalline Solutions: II. Calculations Based On Volume Data. Amer Miner 53:2000–2017.
Wieseneder H (1971) Gesteinsserien und Metamorphose im Ostabschnitt der Österreichischen Zentralalpen. Verh Geol B-A 1971:344–357.
Whitney DL, Evans BW (2010) Abbreviations for names of rock-forming minerals. Amer Miner 95:185–187. doi: 10.2138/am.2010.3371

Figures

Fig. 1 Geological map of the eastern part of the Eastern Alps including Sopron area (W-Hungary). Tectonic nomenclature after Schmid et al. (2004) and Schuster and Nowotny (2015). The Austrian-Hungarian border is marked with double dotted dashed line.

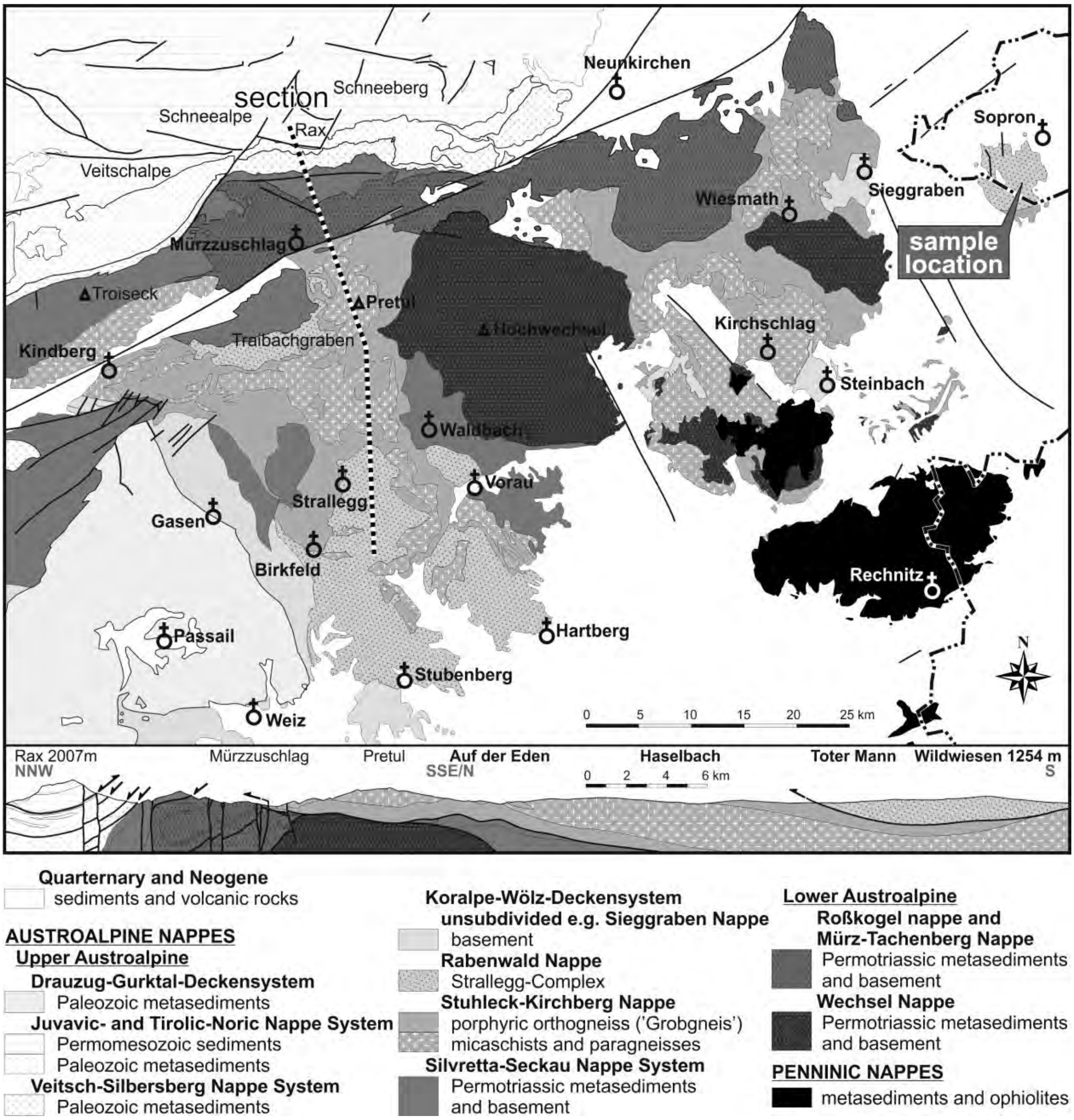

Fig. 2 Microstructure and mineral chemistry of Kfs-Pl-Sill-Bt-rich bands. Abbreviations and descriptions of mineral generations are listed in **Appendix 1**. **a)** Back-scattered electron image (BSEI) of a $Bt1_K$ biotite generation containing ilmenite inclusions, obliterated by $Grt2_K$ garnet and $Ms3_K$ muscovite. Fibrous sillimanite (Sil_K) crosscuts muscovite-biotite grain boundary. **b)** BSEI of poikilitic plagioclase ($Pl1_K$) and K-feldspar (Kfs_K) containing albitic plagioclase lamellae ($Pl3_K$). **c)** Photomicrograph of a K-feldspar-sillimanite (Kfs_K–Sil_K) intergrowth. The K-feldspar contains oriented albitic plagioclase lamellae ($Pl3_K$). **d)** BSEI of an $Ms1_K$ muscovite flake containing Ti-rich $Bt1_K$ relic contacting with small, Mg-rich $Bt2_K$ biotite. At the grain boundaries small $St2_K$ staurolite laths are observed. **e)** BSEI of a garnet-bearing subdomain. $Pl2_K$ plagioclase, $Ms2_K$ muscovite and $Bt2_K$ biotite hold microstructural equilibrium with a zoned $Grt1_K$ garnet with a core hosting submicrometre sized anhedral biotite inclusions and a rim intergrown with larger $St1_K$ staurolite and $Bt2_K$ biotite laths. The $Grt1_K$ garnet is in contact with an ultrafine-grained nest built up by $MicaIG_K$. The arrow shows the position of the compositional profile shown in **Fig. 2f**. **f)** Compositional profile of a $Grt1_K$ garnet along the line marked by an arrow pointing to the endpoint in **Fig. 2e**.

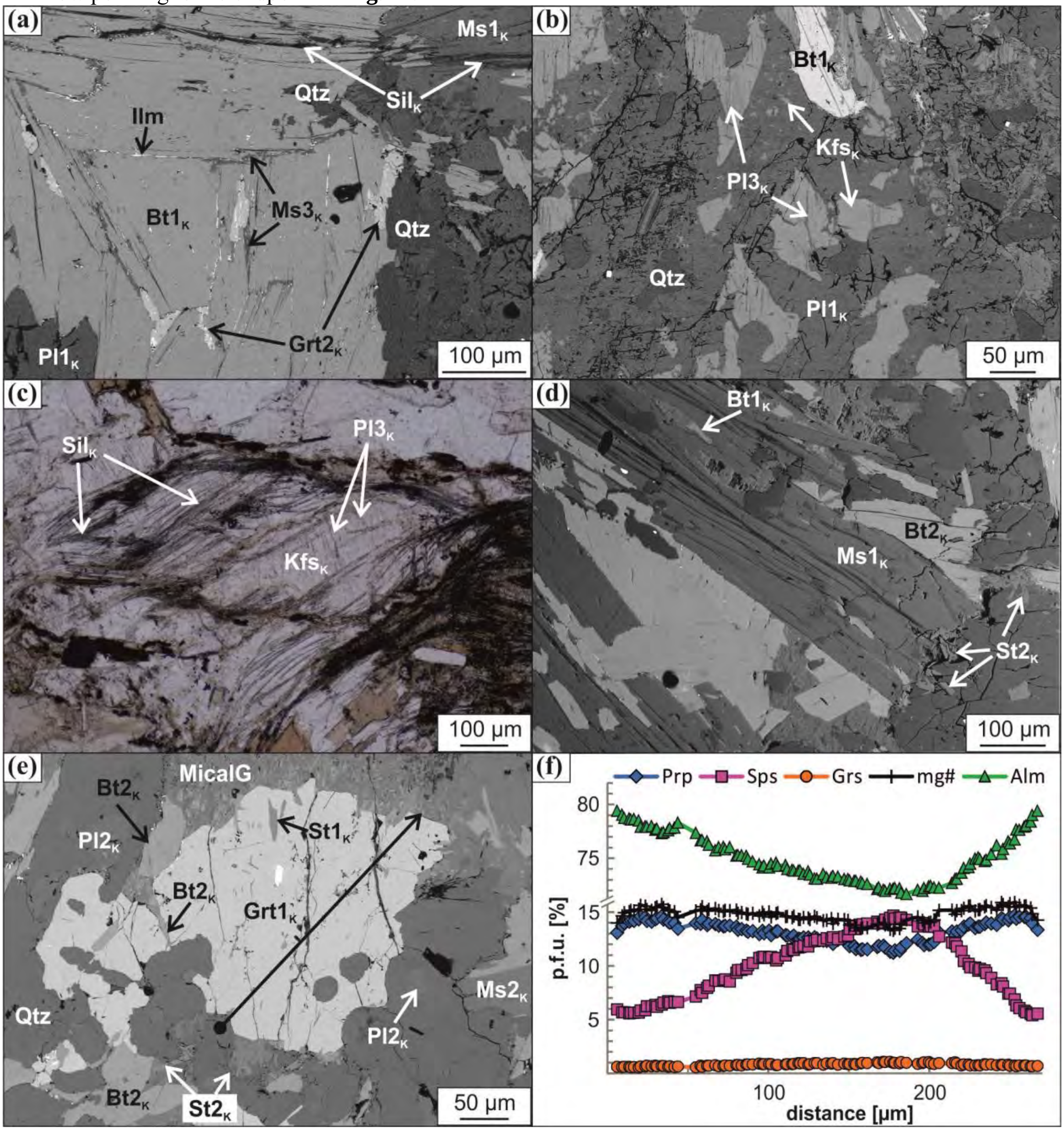

Fig. 3 Petrography and mineral chemistry of garnet porphyroblasts. Abbreviations and descriptions of mineral generations are listed in **Appendix 1**. **a)** BSEI of a Grt_G garnet porphyroblast from the KA-6n sample. Small white rectangle mark the place of the inlet showing the Grt_G–$Bt1_K$ contact in higher magnification, where ilmenite inclusions elongated perpendicular to the interphase boundary are found. Places of the compositional profiles shown in **Fig. 3d–f** are marked by red arrows pointing to the end of the profiles. Yellow rectangle indicates the place of element distribution maps shown in **Fig. 3b–c**. **b-c)** Ca and Mn element distributions from the area marked by a yellow rectangle on **Fig. 3a**. Lighter colours indicate higher concentrations. Ca distribution is clearly modified by a crack on the left hand side of the garnet. Distribution of Mn maxima does not seem to depend on the neighbouring phase. **d-f)** Compositional profiles along the lines marked on **Fig. 3a.** Please note that a false low Ca core is seen on P2 profile between the dotted lines which is the result of a late modification. **g)** High resolution compositional profile perpendicular to the boundary of $Bt1_K$ and Grt_G.

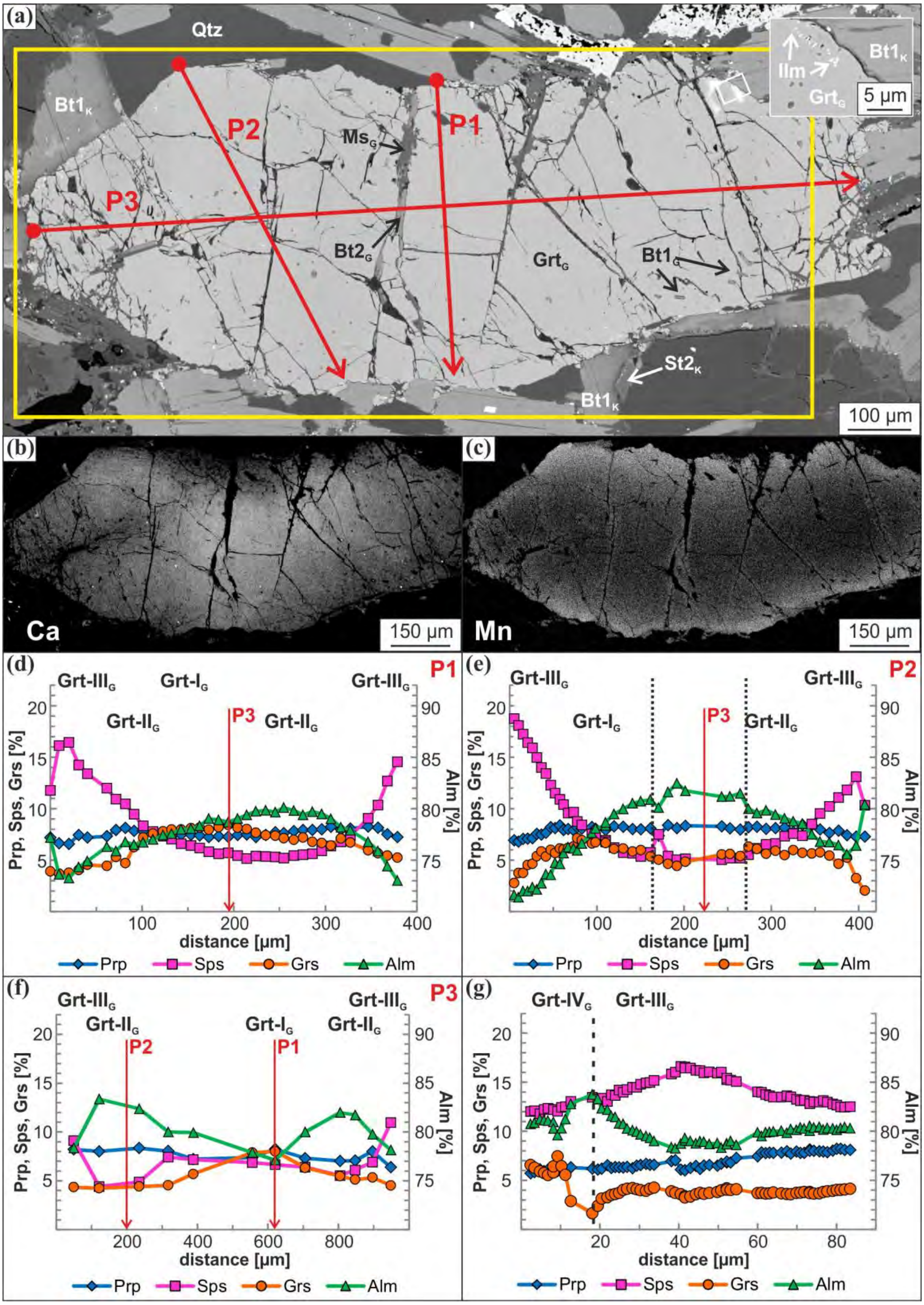

(a)
Qtz
Bt1K
Ilm
Grt G
5 µm
P1
P2
P3
Ms G
Bt2G
Grt G
Bt1G
St2K
Bt1K
100 µm
(b)
Ca
150 µm
(c)
Mn
150 µm
(d)
P1
Grt-III G
Grt-I G
Grt-II G
P3
Prp, Sps, Grs [%]
Alm [%]
distance [µm]
Prp
Sps
Grs
Alm
(e)
P2
Grt-I G
Grt-II G
(f)
P3
Grt-III G
Grt-II G
Grt-I G
P2
P1
(g)
Grt-IV G
Grt-III G

Fig. 4 Microstructure and mineral chemistry of andalusite porphyroblasts. Abbreviations and descriptions of mineral generations are listed in **Appendix 1**. **a)** Two generations of andalusite porphyroblasts. Staurolite relics ($St1_A$), sillimanite ($Sil1_A$) and biotite ($Bt1_A$) are found as inclusions in deformed $And1_A$ overgrown by undeformed $And2_A$ andalusite porphyroblast. **b)** Fibrous $Sil2_A$ sillimanite grown between $And1_A$ and $And2_A$. **c)** Spinel and corundum inclusions in an $And1_A$ porphyroblast close to $St1_A$. Spinel and $St1_A$ staurolite is overgrown by $St2_A$ staurolite laths. **d)** $Bt1_A$ biotite inclusion partly replaced by $St2_A$ staurolite, muscovite and ilmenite in $And1_A$ porphyroblast. **e**) X_{Ti} vs. mg# plot of different biotite generations found in the andalusite-sillimanite-biotite schist.

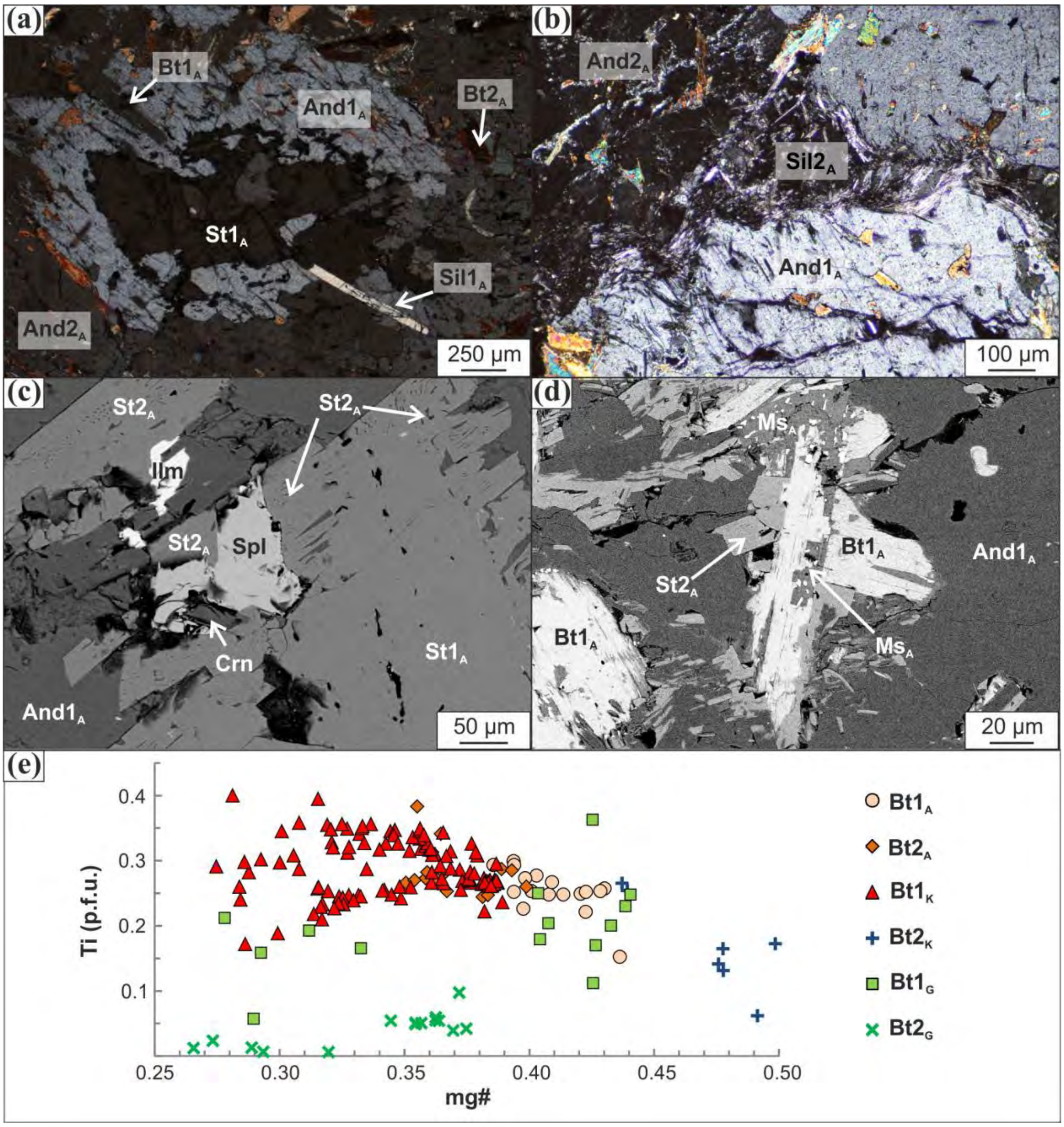

Fig. 5 Age diagrams from sample KA-1. **a**) Sm-Nd isochron for whole rock (WR) and two garnet fractions (Grt-C1, Grt-C2) indicating the formation of the cores of garnet porphyroblasts at 330 Ma during the Variscan tectonometamorphic event. **b**) Rb-Sr age from whole rock (WR) and biotite (Bt), interpreted as a pre-Alpine age partly rejuvenated during the Alpine metamorphic overprint.

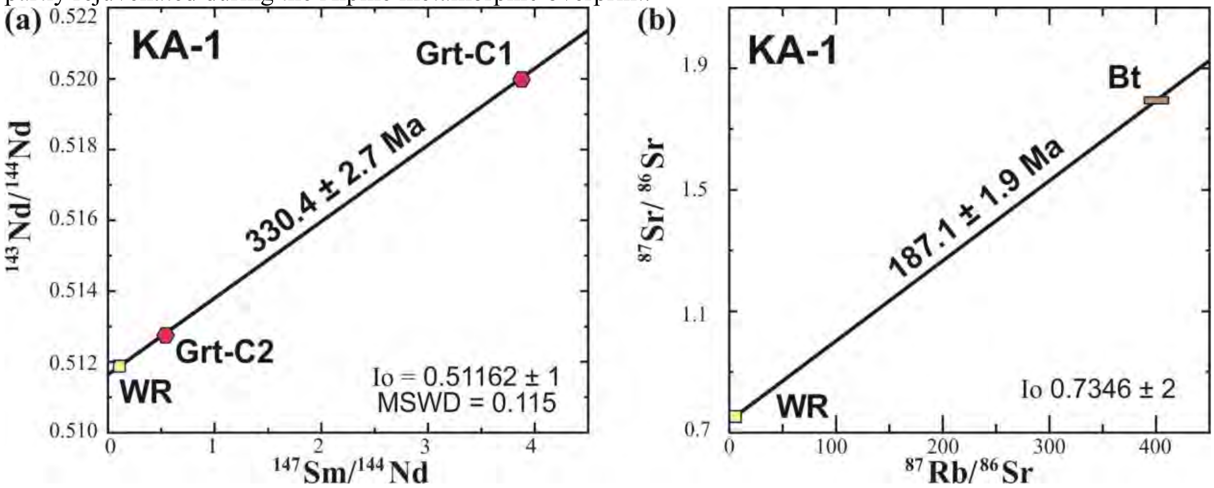

Fig. 6 Phase equilibria modelling for Stage1. **a)** Phase equilibria calculated for the measured whole rock composition (V, **Tab. 5**) and the suggested Variscan (dotted arrow) and prograde Permo-Triassic (solid arrow) P–T path explaining zoning trend seen in Grt-II_G and Grt-III_G. Stability fields of garnet, staurolite, andalusite and cordierite are contoured by pink, orange, blue and red heavy lines, respectively. Mineral abbreviations follow Whitney and Evans (2010). Mineral assemblages in numbered fields: 1 – Bt, Crd, Pl, Ms, Sil; 2 – Bt, Crd, Pl, Ms, Sil, San; 3 – Bt, Crd, Pl, Sil, San; 4 – Bt, Crd, Grt, Pl, Ms, Sil, San; 5 – Bt, Grt, Pl, Ms, Sil, San, 6 – Bt, Crd, St, Pl, Ms, Grt, And, 7 – Bt, St, Pl, Ms, Grt, And. **b)** Staurolite (white) and biotite (yellow) mg# isopleths plotted on the fields of the phase diagram pseudosection shown in **Fig. 6a**. **c)** Isopleths of X_{An} in plagioclase (yellow lines) and X_{Sps} in garnet (dark blue lines) plotted on the fields of the phase diagram pseudosection shown in **Fig. 6a**. Mineral abbreviations follow Whitney and Evans (2010).

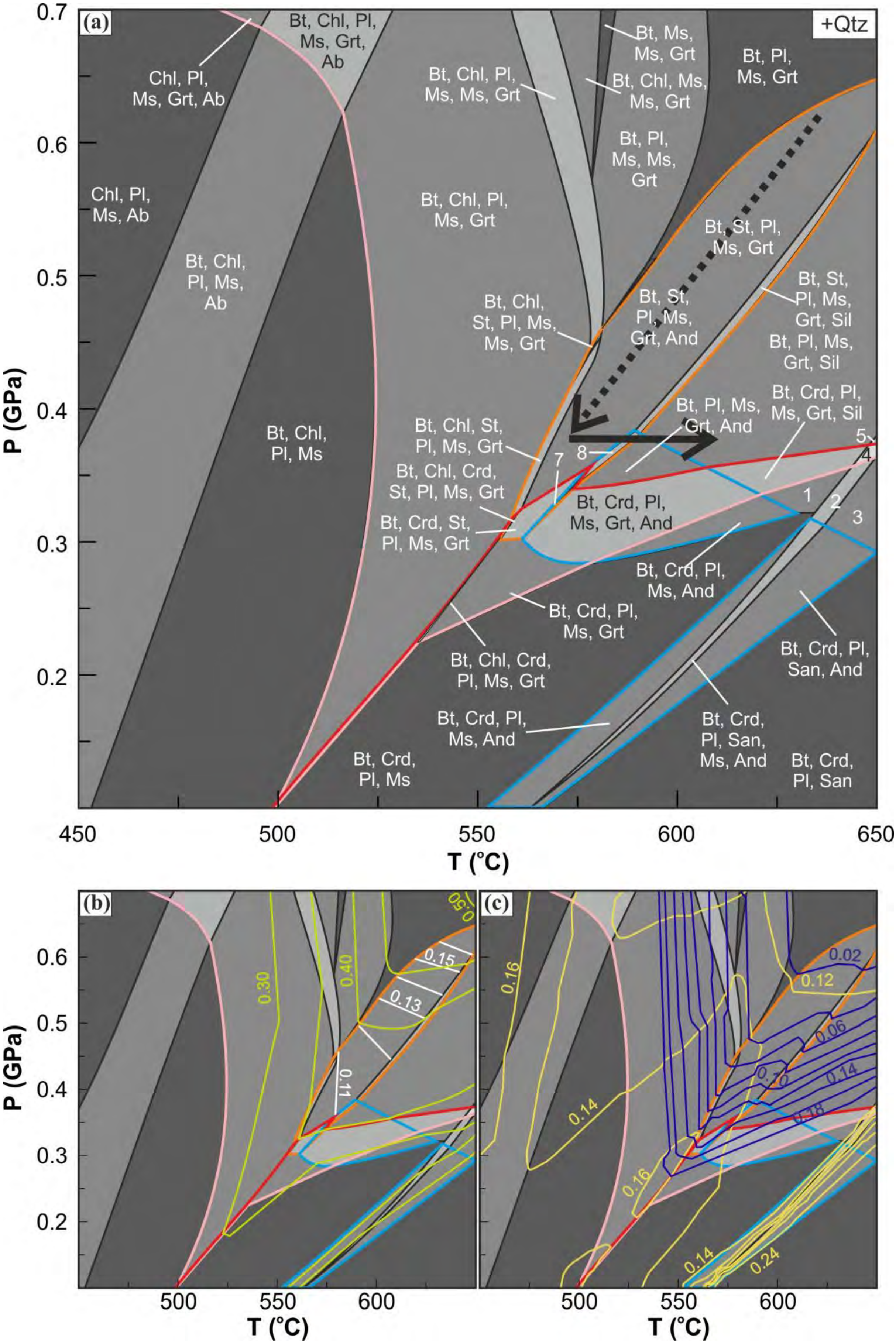

(a)
+Qtz
Chl, Pl, Ms, Grt, Ab
Bt, Chl, Pl, Ms, Grt, Ab
Chl, Pl, Ms, Ab
Bt, Chl, Pl, Ms, Ab
Bt, Chl, Pl, Ms
Bt, Chl, Pl, Ms, Ms, Grt
Bt, Ms, Ms, Grt
Bt, Chl, Ms, Ms, Grt
Bt, Pl, Ms, Grt
Bt, Pl, Ms, Ms, Grt
Bt, Chl, Pl, Ms, Grt
Bt, St, Pl, Ms, Grt
Bt, Chl, St, Pl, Ms, Ms, Grt
Bt, St, Pl, Ms, Grt, And
Bt, St, Pl, Ms, Grt, Sil
Bt, Pl, Ms, Grt, Sil
Bt, Crd, Pl, Ms, Grt, Sil
Bt, Pl, Ms, Grt, And
Bt, Chl, St, Pl, Ms, Grt
Bt, Chl, Crd, St, Pl, Ms, Grt
Bt, Crd, St, Pl, Ms, Grt
Bt, Crd, Pl, Ms, Grt, And
Bt, Crd, Pl, Ms, And
Bt, Crd, Pl, Ms, Grt
Bt, Chl, Crd, Pl, Ms, Grt
Bt, Crd, Pl, San, And
Bt, Crd, Pl, Ms, And
Bt, Crd, Pl, San, Ms, And
Bt, Crd, Pl, Ms
Bt, Crd, Pl, San
1
2
3
4
5
7
8
P (GPa)
0.7
0.6
0.5
0.4
0.3
0.2
T (°C)
450
500
550
600
650
(b)
0.30
0.40
0.50
0.15
0.13
0.11
P (GPa)
0.6
0.5
0.4
0.3
0.2
T (°C)
500
550
600
(c)
0.16
0.14
0.16
0.14
0.24
0.02
0.12
0.06
0.10
0.14
0.18
T (°C)
500
550
600

Fig. 7 Phase equilibria modelling for Stage2. The calculation is based on the estimated Permo-Triassic bulk rock composition (P in **Tab. 5**). Stability limits of garnet, K-feldspar, muscovite, melt and cordierite are contoured by pink, green, yellow, magenta and red heavy lines, respectively. **a)** Phase stabilities. Mineral assemblages in numbered fields: 1 – Crd, Pl, Kfs, Opx, Grt, H_2O; 2 – Crd, Pl, Kfs, Opx, melt, H_2O; 3 – Crd, Pl, Kfs, Opx, Grt, melt, H_2O; 4 – Bt, Crd, Pl, Kfs, Opx, Grt, melt, H_2O; 5 – Bt, Pl, Ms, Grt, melt; 6 – Bt, Pl, Ms, Grt, melt, H_2O; 7 – Bt, Pl, Ms, Grt, H_2O; 8 – Bt, St, Pl, Ms, Grt, melt, H_2O; 9 – Bt, St, Pl, Ms, Grt, melt; 10 – Bt, St, Pl, Ms, Grt, Sil, melt; 11 – Bt, Pl, Kfs, Crd, Ms, Sil, melt, H_2O; 12 – Bt, Pl, Kfs, Ms, Sil, H_2O; 13 – Bt, Pl, Kfs, Sil, H_2O;14 – Bt, Pl, Kfs, Sil, melt, H_2O; 15 – Bt, Pl, Kfs, Crd, Sil, melt, H_2O. **b)** P−T conditions where biotite, plagioclase, K-feldspar and sillimanite are stable together (blue field) and P−T conditions of the metamorphic peak, where the biotite-plagioclase-K-feldspar-sillimanite assemblage is stable in the absence of garnet and cordierite (orange field) plotted on the fields of the phase diagram pseudosection shown in **Fig. 7a**. **c)** X_{Sps} isopleths and the suggested Permo-Triassic prograde (black solid arrow) and retrograde (white solid arrow) P–T path explaining the formation of Kfs-Pl-Sil-Bt-rich bands, plotted on the fields of the phase diagram pseudosection shown in **Fig. 7a**. Mineral abbreviations follow Whitney and Evans (2010).

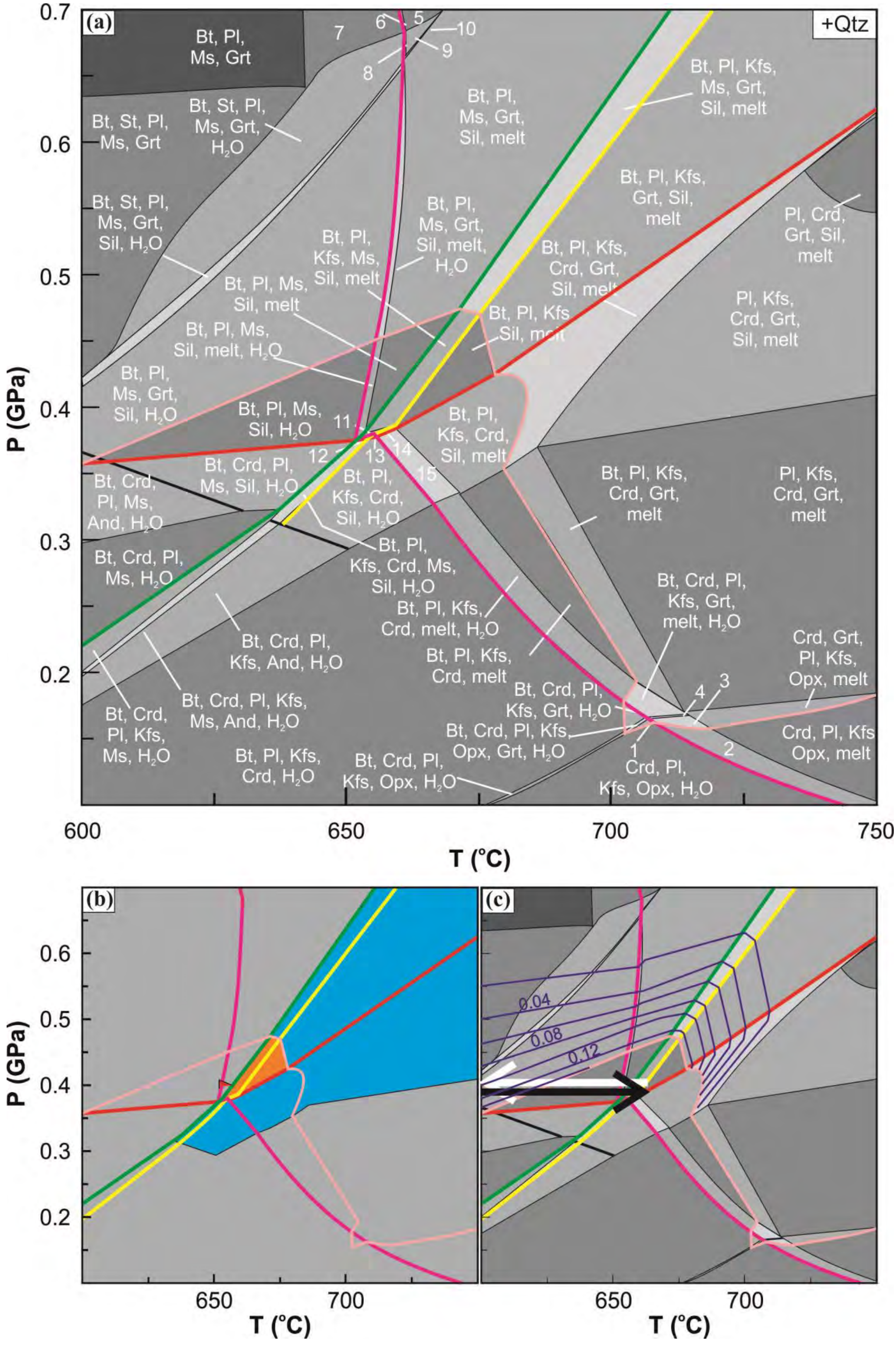
(a)
+Qtz
Bt, Pl, Ms, Grt
Bt, St, Pl, Ms, Grt
Bt, St, Pl, Ms, Grt, H2O
Bt, St, Pl, Ms, Grt, Sil, H2O
Bt, Pl, Ms, Grt, Sil, H2O
Bt, Crd, Pl, Ms, And, H2O
Bt, Crd, Pl, Ms, H2O
Bt, Crd, Pl, Kfs, Ms, H2O
Bt, Crd, Pl, Kfs, Ms, And, H2O
Bt, Crd, Pl, Kfs, And, H2O
Bt, Pl, Kfs, Crd, H2O
Bt, Crd, Pl, Kfs, Opx, H2O
Bt, Pl, Ms, Grt, Sil, melt
Bt, Pl, Ms, Grt, Sil, melt, H2O
Bt, Pl, Kfs, Ms, Sil, melt
Bt, Pl, Ms, Sil, melt
Bt, Pl, Ms, Sil, melt, H2O
Bt, Pl, Ms, Sil, H2O
Bt, Crd, Pl, Ms, Sil, H2O
Bt, Pl, Kfs, Crd, Sil, H2O
Bt, Pl, Kfs, Crd, Ms, Sil, H2O
Bt, Pl, Kfs, Crd, melt, H2O
Bt, Pl, Kfs, Crd, melt
Bt, Pl, Kfs, Crd, Sil, melt
Bt, Pl, Kfs, Sil, melt
Bt, Pl, Kfs, Ms, Grt, Sil, melt
Bt, Pl, Kfs, Grt, Sil, melt
Bt, Pl, Kfs, Crd, Grt, Sil, melt
Pl, Crd, Grt, Sil, melt
Pl, Kfs, Crd, Grt, Sil, melt
Bt, Pl, Kfs, Crd, Grt, melt
Pl, Kfs, Crd, Grt, melt
Bt, Crd, Pl, Kfs, Grt, melt, H2O
Bt, Crd, Pl, Kfs, Grt, H2O
Bt, Crd, Pl, Kfs, Opx, Grt, H2O
Crd, Pl, Kfs, Opx, H2O
Crd, Grt, Pl, Kfs, Opx, melt
Crd, Pl, Kfs Opx, melt
1 2 3 4 5 6 7 8 9 10 11 12 13 14 15
P (GPa)
0.7 0.6 0.5 0.4 0.3 0.2
T (°C)
600 650 700 750
(b)
P (GPa)
0.6 0.5 0.4 0.3 0.2
T (°C)
650 700
(c)
0.04
0.08
0.12
T (°C)
650 700

Fig. 8 Phase equilibria modelling for Stage3. The calculation was carried out using the estimated Alpine bulk rock composition (A in Tab. 5). **a)** Phase stabilities. Orange line indicate the stability limit of staurolite. 1 – Stability field of the Bt, St, Crd, Pl, Ms, Grt, And mineral assemblage. Mineral abbreviations follow Whitney and Evans (2010). **b)** mg# (red solid line) X_{Sps} (black dashed line) and X_{Grs} (yellow dotted line) isopleths of garnet and the suggested retrograde Permo-Triassic (solid white arrow) and Alpine (dashed white arrow) P–T path explaining the mineralogy of KA-10 sample and zoning trend of Alpine Grt1K garnet shown in **Fig. 5e,** plotted on the fields of the phase diagram pseudosection shown in **Fig. 8a**. **c)** mg# ispoleths of staurolite (dashed black line) and biotite (solid blue line) plotted on the fields of the phase diagram pseudosection shown in **Fig. 8a**.

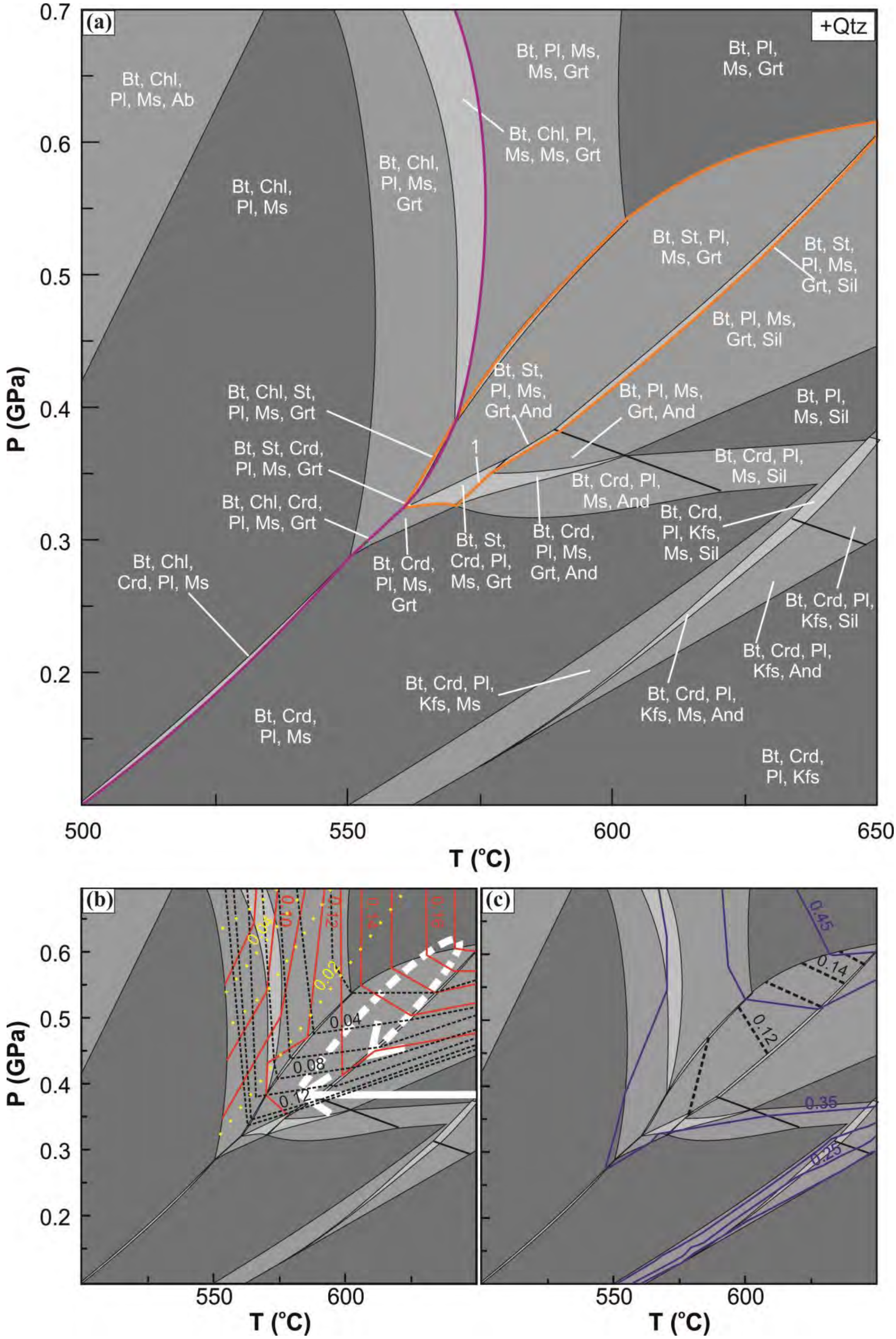

(a)
+Qtz
Bt, Chl, Pl, Ms, Ab
Bt, Chl, Pl, Ms
Bt, Chl, Pl, Ms, Grt
Bt, Pl, Ms, Ms, Grt
Bt, Chl, Pl, Ms, Ms, Grt
Bt, Pl, Ms, Grt
Bt, St, Pl, Ms, Grt
Bt, St, Pl, Ms, Grt, Sil
Bt, Pl, Ms, Grt, Sil
Bt, St, Pl, Ms, Grt, And
Bt, Pl, Ms, Grt, And
Bt, Pl, Ms, Sil
Bt, Chl, St, Pl, Ms, Grt
Bt, St, Crd, Pl, Ms, Grt
Bt, Chl, Crd, Pl, Ms, Grt
1
Bt, Crd, Pl, Ms, Sil
Bt, Crd, Pl, Ms, And
Bt, Crd, Pl, Kfs, Ms, Sil
Bt, Chl, Crd, Pl, Ms
Bt, Crd, Pl, Ms, Grt
Bt, St, Crd, Pl, Ms, Grt
Bt, Crd, Pl, Ms, Grt, And
Bt, Crd, Pl, Kfs, Sil
Bt, Crd, Pl, Kfs, And
Bt, Crd, Pl, Kfs, Ms
Bt, Crd, Pl, Kfs, Ms, And
Bt, Crd, Pl, Ms
Bt, Crd, Pl, Kfs
P (GPa)
T (°C)
(b)
0.04
0.08
0.12
0.02
(c)
0.45
0.14
0.12
0.35
0.25

Fig. 9 P-T reconstructions of the Óbrennberg Micaschist from the literature and this study. Patterned grey arrow shows Alpine P-T loop from Török (2003). Grey and white ellipses mark the pre-Alpine and Alpine peak conditions determined by Draganits (1998), respectively. Dotted green, solid red and dashed blue arrows represent the Variscan, Permo-Triasic and Alpine P–T path suggested by this study. The rectangle mark the PT estimate of Török (1999) for the pre-Alpine temperature peak.

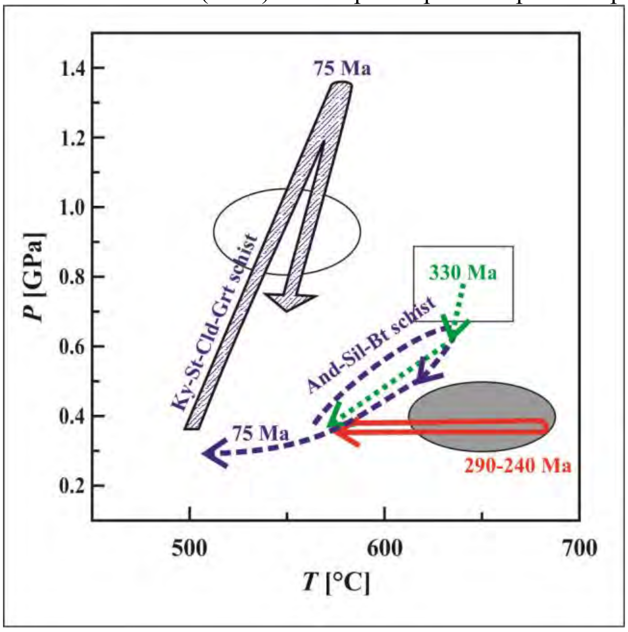

Online Resource 1 Phase equilibria calculated for the estimated Alpine bulk rock composition (A in **Tab. 5**) between 450–700 °C and 0.1–1.1 GPa in the MnNCKFMASH system using the PERPLEX software package (Connolly 2009) and the database of Holland and Powell (1998). Solution models used were garnet, cordierite, chloritoid, orthopyroxene and staurolite from Holland and Powell (1998), biotite from Tajcmanova et al. (2009), high temperature feldspar from Fuhrman and Lindsley (1988), low temperature feldspar from Newton et al. (1980), sanidine from Waldbaum and Thompson (1968) and white mica from Coggon and Holland (2002) The Stage3 garnet-plagioclase-biotite-staurolite-muscovite mineral assemblage is stable in a narrow field limited by orange line. Mineral abbreviations follow Whitney and Evans (2010).

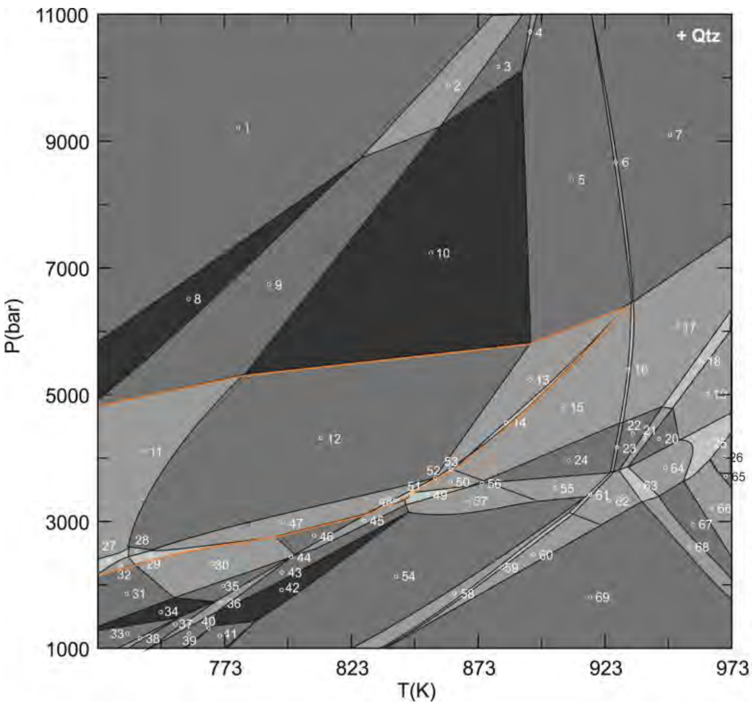

1	Bt Ms Ms Grt Ab
2	Bt Fsp Ms Ms Grt Ab
3	Bt Fsp Ms Ms Grt
4	Bt Fsp Ms Ms Grt H_2O
5	Bt Fsp Ms Grt H_2O
6	Bt melt Fsp Ms Grt H_2O
7	Bt melt Fsp Ms Grt
8	Bt Ms Grt Ab
9	Bt Fsp Ms Grt Ab
10	Bt Fsp Ms Grt
11	Bt St Fsp Ms Grt Ab
12	Bt St Fsp Ms Grt
13	Bt St Fsp Ms Grt H_2O
14	Bt St Fsp Ms Grt Sil H_2O
15	Bt Fsp Ms Grt Sil H_2O
16	Bt melt Fsp Ms Grt Sil H_2O
17	Bt melt Fsp Ms Grt Sil
18	Bt melt Fsp Fsp Ms Grt Sil
19	Bt melt Fsp Fsp Grt Sil
20	Bt melt Fsp Fsp Sil
21	Bt melt Fsp Fsp Ms Sil
22	Bt melt Fsp Ms Sil
23	Bt melt Fsp Ms Sil H2O
24	Bt Fsp Ms Sil H2O
25	Bt melt Crd Fsp Fsp Grt Sil
26	melt Crd Fsp Fsp Grt Sil
27	Bt St Fsp Ms Grt And Ab
28	Bt St Fsp Ms Ms Grt
29	Bt St Fsp Ms Ms Grt And
30	Bt Fsp Ms Ms Grt And
31	Bt Fsp Ms Grt And
32	Bt St Fsp Ms Grt And
33	Bt Chl Fsp Ms And
34	Bt Fsp Ms And
35	Bt Fsp Ms Ms And

36	Bt Crd Fsp Ms Ms And
37	Bt Crd Fsp Ms And
38	Bt Chl Crd Fsp Ms And
39	Bt Crd Fsp Ms Ms
40	Bt Chl Crd Fsp Ms Ms
41	Bt Chl Crd Fsp Ms
42	Bt Crd Fsp Ms
43	Bt Crd Fsp Ms And
44	Bt Crd Fsp Ms Ms Grt And
45	Bt Crd Fsp Ms Grt And
46	Bt Fsp Ms Grt And
47	Bt St Fsp Ms Grt And
48	Bt St Crd Fsp Ms Grt And
49	Bt Crd Fsp Ms Grt And H_2O
50	Bt Fsp Ms Grt And H_2O
51	Bt St Crd Fsp Ms Grt And H_2O
52	Bt St Fsp Ms Grt And
53	Bt St Fsp Ms Grt And H_2O
54	Bt Crd Fsp Ms H_2O
55	Bt Crd Fsp Ms Sil H_2O
56	Bt Fsp Ms And H_2O
57	Bt Crd Fsp Ms And H_2O
58	Bt Crd Fsp Fsp Ms H_2O
59	Bt Crd Fsp Fsp Ms And H_2O
60	Bt Crd Fsp Fsp And H_2O
61	Bt Crd Fsp Fsp Ms Sil H_2O
62	Bt Crd Fsp Fsp Sil H_2O
63	Bt melt Crd Fsp Fsp Sil H_2O
64	Bt melt Crd Fsp Fsp Sil
65	melt Crd Fsp Fsp Grt
66	Bt melt Crd Fsp Fsp Grt
67	Bt melt Crd Fsp Fsp
68	Bt melt Crd Fsp Fsp H_2O
69	Bt Crd Fsp Fsp H_2O

Appendix 1 Mineral generations distinguished in the andalusite-sillimanite-biotite schist. G, A and K in the bottom righ index stands for garnet porphyroblasts, andalusite prophyroblasts and Kfs-Pl-Sil-Bt-rich bands.

Mineral generation	**Description**
Grt_G	garnet porphyroblast
$Grt\text{-}I_G$	inclusion-free Ca-rich core of Grt_G
$Grt\text{-}II_G$	Fe-rich inner zone of Grt_G containing numerous biotite inclusions
$Grt\text{-}III_G$	Mn-rich outer zone of Grt_G containing numerous biotite inclusions
$Grt\text{-}IV_G$	the outermost zone of Grt_G containing oriented ilmenite inclusions; appearing just in contact with $Bt1_K$
$Bt1_G$	euhedral biotite inclusions in Grt_G
$Bt2_G$	biotite inclusions in Grt_G related to cracks, associated with Ms_G
Ms_G	muscovite inclusions in Grt_G related to cracks, associated with $Bt2_G$
$Bt1_K$	large biotite flakes containing ilmenite inclusions
$Pl1_K$	large poikilitic feldspar containing Kfs_K and quartz inclusions
Kfs_K	K-feldspar grains found as poikilitic inclusions in $Pl1_K$ or as individual grains frequently intergrown with Sil_K
Sil_K	fibrous sillimanite sometimes intergrown with Kfs_K or large micas ($Ms1_K$, $Bt1_K$)
$Ms1_K$	large muscovite flakes containing relics of $Bt1_K$
$Grt1_K$	several hundred micron wide euhedral garnet grains holding microstructural equilibrium with $St1_K$, $Ms2_K$, $Bt2_K$ and $Pl2_K$
$St1_K$	staurolite laths found as inclusion in the rim of $Grt1_K$
$Ms2_K$	small muscovite laths found in equilibrium with $Grt1_K$, $St1_K$ and $Bt2_K$
$Bt2_K$	inclusion-free bitotite laths found in equilibrium with $Grt1_K$, $St1_K$ and $Ms2_K$
$Grt2_K$	small garnet grains grown along cracks and grian boundaries of $Bt1_K$ biotite
$Ms3_K$	muscovite grown along cracks within the $Bt1_K$ biotite
$Pl3_K$	albitic lamellae in Kfs_K
$Pl2_K$	small plagioclase in equilibrium with $Grt1_K$, $St1_K$, $Ms2_K$ and $Bt2_K$
$MicaIG_K$	submicron scale intergrowths of biotite and white micas apeearing in nests in Kfs-Pl-Sil-Bt-rich bands
$St2_K$	smaller, euhedral staurolite laths or twins found as overgrowths on $Ms1_K$ muscovites, on $Bt1_K$ biotite, along cracks and in nests filled by ultrafine-grained alteration products
$And1_A$	inclusion-rich andalusite porphyroblasts showing mosaic extinction in optical microscope, frequently overprinted by $Sil2_A$
$And2_A$	undeformed andalusite generation where inclusions are restricted to biotite and quartz
$Sil1_A$	fibrous sillimanite found around $And1_A$ or in between $And1_A$ and $And2_A$
$Sil2_A$	fibrous sillimanite found around $And1_A$ or in between $And1_A$ and $And2_A$
$St1_A$	several hundreds or tens of µm sized anhedral staurolite inclusions in $And1_A$
$Bt1_A$	biotite inclusions preserved in $And1_A$
$Bt2_A$	biotite inclusions found in $And2_A$ together with quartz
$St2_A$	10 µm long, 2-5 µm wide poikilitic staurolite laths overgrown on St1A, Bt1A or spinel showing different optical orientation
Ms_A	muscovite replacing biotite within andalusite inclusions
Grt_G	garnet porphyroblast
$Grt\text{-}I_G$	inclusion-free Ca-rich core of Grt_G
$Grt\text{-}II_G$	Fe-rich inner zone of Grt_G containing numerous biotite inclusions
$Grt\text{-}III_G$	Mn-rich outer zone of Grt_G containing numerous biotite inclusions

Tables

Tab. 1 Representative microprobe analyses of feldspar generations from the andalusite-sillimanite-biotite schist. FeO_t – total iron in FeO, $Pl1_K$* – plagioclase core further from Kfs-Sill-bearing assemblages. Feldspar types are described in detail in **Appendix 1**.

Type	Kfs_K	Kfs_K	$Pl1_K$*	$Pl1_K$	$Pl1_K$	$Pl2_K$	$Pl3_K$
SiO_2	64,21	63,40	63,95	63,54	62,71	64,28	66,20
Al_2O_3	18,57	18,65	22,03	23,00	23,01	22,55	20,95
FeO_t	0,02	0,10	0,00	0,06	0,37	0,16	0,06
CaO	0,02	0,01	2,87	3,68	3,90	2,80	1,74
Na_2O	0,71	0,64	9,32	8,93	9,50	9,40	10,05
K_2O	15,82	15,85	0,24	0,16	0,09	0,04	0,16
Total	99,35	98,65	98,41	99,37	99,60	99,23	99,16
Si	2,985	2,973	2,856	2,816	2,789	2,846	2,923
Al	1,018	1,031	1,160	1,201	1,206	1,177	1,090
Fe	0,001	0,004	0,000	0,002	0,014	0,006	0,002
Ca	0,001	0,000	0,138	0,175	0,186	0,133	0,082
Na	0,064	0,058	0,807	0,768	0,820	0,807	0,860
K	0,938	0,948	0,014	0,009	0,005	0,002	0,009
Total	5,007	5,015	4,975	4,971	5,020	4,971	4,966
Ab	0,064	0,058	0,842	0,807	0,811	0,857	0,904
An	0,001	0,000	0,144	0,184	0,184	0,141	0,086
Or	0,935	0,942	0,014	0,009	0,005	0,002	0,010

FeO_t – total iron in FeO. Feldspar types are described in detail in Appendix 1.

$Pl1_K$* – plagioclase core further from Kfs-Sill-bearing assemblages

Feldspar types are described in detail in Appendix 1.

Tab. 2 Representative microprobe analyses of mica generations from andalusite-sillimanite-biotite schist. *FeO_t* – total iron in FeO, * – inclusion found in the rim of Grt1K. Mica types are described in detail in **Appendix 1**.

	Garnet porphyroblasts			Andalusite porphyroblasts			Kfs-Pl-Sill-Bt-rich bands					
Type	$Bt1_G$	$Bt2_G$	Ms_G	$Bt1_A$	$Bt2_A$	Ms_A	$Bt1_K$	$Bt2_K$	$Bt2_K$*	$Ms1_K$	$Ms2_K$	$Ms3_K$
SiO_2	35,29	34,54	48,95	34,84	34,33	46,20	33,24	35,19	33,43	45,06	45,63	47,35
TiO_2	1,84	0,48	0,20	2,18	2,71	0,52	2,77	0,19	0,54	0,38	0,08	0,65
Al_2O_3	20,25	22,20	31,80	20,53	20,46	36,22	19,87	22,18	22,61	36,55	36,86	34,63
FeO_t	20,65	22,18	2,59	20,45	21,59	1,12	21,41	16,31	19,11	0,87	0,87	1,23
MnO	0,24	0,24	0,10	0,15	0,10	0,02	0,13	0,02	0,20	0,01	0,03	0,00
MgO	8,64	7,12	2,03	8,33	6,84	0,66	7,27	11,49	10,36	0,62	0,67	0,66
CaO	0,02	0,06	0,03	0,00	0,12	0,09	0,11	0,05	0,07	0,20	0,06	0,02
Na_2O	0,09	0,05	0,12	0,11	0,13	0,35	0,24	0,18	0,11	0,48	0,42	0,19
K_2O	8,64	9,29	9,76	9,37	9,13	9,66	9,01	9,33	8,17	9,96	9,98	10,54
F	0,00	0,00	0,00	0,00	0,00	0,02	0,00	0,07	0,00	0,02	0,05	0,01
Cl	0,00	0,04	0,01	0,07	0,00	0,01	0,04	0,02	0,04	0,02	0,00	0,00
Total	95,66	96,19	95,57	96,03	95,41	94,87	94,09	95,02	94,64	94,18	94,65	95,28
Si	5,350	5,260	6,485	5,287	5,268	6,132	5,197	5,272	5,085	6,044	6,079	6,281
Ti	0,210	0,055	0,020	0,249	0,313	0,052	0,326	0,022	0,062	0,039	0,008	0,065
Al	3,619	3,986	4,965	3,672	3,702	5,666	3,661	3,917	4,053	5,779	5,789	5,415
Fe	2,618	2,825	0,287	2,595	2,771	0,124	2,800	2,043	2,431	0,098	0,096	0,137
Mn	0,030	0,031	0,011	0,019	0,013	0,002	0,017	0,003	0,026	0,001	0,003	0,000
Mg	1,952	1,616	0,401	1,884	1,566	0,131	1,694	2,565	2,349	0,124	0,134	0,130
Ca	0,003	0,010	0,004	0,000	0,020	0,013	0,018	0,008	0,011	0,029	0,008	0,003
Na	0,026	0,013	0,030	0,031	0,038	0,091	0,074	0,051	0,032	0,126	0,109	0,049
K	1,670	1,806	1,650	1,813	1,789	1,636	1,797	1,784	1,586	1,705	1,696	1,783
F	0,000	0,000	0,000	0,000	0,000	0,007	0,000	0,031	0,000	0,010	0,022	0,004
Cl	0,000	0,009	0,001	0,019	0,001	0,001	0,012	0,005	0,011	0,005	0,001	0,000
Sum	15,479	15,612	13,854	15,569	15,481	13,855	15,596	15,700	15,645	13,959	13,945	13,866
mg#	0,43	0,36	0,58	0,42	0,36	0,51	0,38	0,56	0,49	0,56	0,58	0,49
Phl	0,57	0,64		0,58	0,64		0,62	0,44	0,51			
Ann	0,43	0,36		0,42	0,36		0,38	0,56	0,49			
Ms			0,60			0,81				0,82	0,83	0,81
Marg			0,00			0,01				0,02	0,00	0,00
Pg			0,02			0,05				0,07	0,06	0,03
Mg-Cel			0,04			0,02				0,03	0,03	0,00
Fe-Cel			0,17			0,07				0,05	0,05	0,07
Pheng			0,17			0,04				0,01	0,02	0,08

FeO_t – total iron in FeO. Mica types are described in detail in Appendix 1.

* – inclusion found in the rim of $Grt1_K$

Tab. 3 Representative garnet microprobe analyses from andalusite-sillimanite-biotite schist. *FeO_t* – total iron in FeO. Garnet types are described in detail in **Appendix 1**.

	Garnet porphyroblasts					Ksp-Pl-Sill-Bt-rich bands		
Type	Grt-I_G	Grt-II_G	Grt-III_G	Grt-IV_G	Grt-IV_G	Grt1$_K$ core	Grt1$_K$ rim	Grt2$_K$
SiO_2	38,43	37,98	37,25	38,02	37,83	37,34	37,66	36,19
TiO_2	0,01	0,03	0,02	0,09	0,13	0,00	0,00	1,95
Al_2O_3	20,89	21,49	21,31	21,42	21,45	22,02	22,18	21,19
FeO_t	35,55	35,22	31,55	34,16	35,53	33,15	35,29	33,07
MnO	2,10	3,81	7,89	5,12	4,51	6,08	2,57	6,91
MgO	1,63	1,85	1,68	1,66	1,56	2,90	3,70	1,53
CaO	3,19	2,05	1,29	1,77	0,53	0,29	0,26	0,85
Total	101,80	102,43	100,99	102,24	101,53	101,78	101,67	101,70
Si	3,051	3,005	2,997	3,014	3,022	2,965	2,973	2,905
Ti	0,000	0,002	0,001	0,006	0,008	0,000	0,000	0,118
Al	1,955	2,005	2,021	2,002	2,020	2,061	2,064	2,005
Fe	2,361	2,331	2,123	2,265	2,374	2,201	2,330	2,220
Mn	0,141	0,256	0,538	0,344	0,306	0,409	0,172	0,470
Mg	0,193	0,218	0,202	0,196	0,186	0,344	0,435	0,183
Ca	0,272	0,174	0,111	0,150	0,045	0,024	0,022	0,073
Sum	7,972	7,990	7,992	7,976	7,959	8,004	7,995	7,975
Prp	0,07	0,07	0,07	0,07	0,06	0,12	0,15	0,06
Alm	0,80	0,78	0,71	0,77	0,82	0,74	0,79	0,75
Sps	0,05	0,09	0,18	0,12	0,10	0,14	0,06	0,16
Grs	0,09	0,06	0,04	0,05	0,02	0,01	0,01	0,02

FeO_t – total iron in FeO. Garnet types are described in detail in Appendix 1.

Tab. 4 Representative microprobe analyses of staurolite generations and oxides from andalusite-sillimanite-biotite schist. *FeO_t* – total iron in FeO, * – ovegrowth on $St1_A$, ** – ovegrowth on $Bt1_A$. Mineral types are described in detail in **Appendix 1**.

	Andalusite porphyroblasts					Kfs-Pl-Sill-Bt-rich bands		
Type	Spl	$St1_A$	$St1_A$	$St2_A$*	$St2_A$**	Ilm	$St1_K$	$St2_K$
SiO_2	0,02	27,22	27,18	27,31	29,84	0,07	27,44	28,44
TiO_2	0,11	0,92	0,82	0,56	0,04	53,06	0,03	0,02
Al_2O_3	60,17	54,33	54,54	54,32	54,70	0,30	56,01	56,67
FeO_t	23,36	12,91	12,62	13,17	11,91	41,74	12,72	11,78
MnO	0,31	0,40	0,38	0,38	0,37	1,93	0,21	0,33
MgO	2,81	1,36	1,35	1,44	1,15	0,11	1,69	1,29
CaO	0,02	0,02	0,02	0,00	0,01	0,02	0,01	0,01
ZnO	14,03	1,34	1,46	1,21	0,44	0,07	0,65	0,65
Total	100,82	98,50	98,37	98,39	98,45	97,30	98,75	99,19
Si	0,000	3,769	3,764	3,785	4,067	0,002	3,761	3,855
Ti	0,002	0,096	0,086	0,058	0,004	1,021	0,003	0,002
Al	2,000	8,865	8,901	8,873	8,785	0,009	9,048	9,053
Fe	0,551	1,495	1,461	1,526	1,357	0,893	1,458	1,335
Mn	0,007	0,047	0,044	0,045	0,043	0,042	0,025	0,038
Mg	0,118	0,280	0,278	0,298	0,233	0,004	0,345	0,260
Ca	0,001	0,002	0,003	0,000	0,001	0,001	0,001	0,001
Zn	0,292	0,137	0,149	0,123	0,044	0,001	0,065	0,065
Sum	2,971	14,690	14,687	14,709	14,533	1,973	14,706	14,611
mg#	0,177	0,158	0,160	0,163	0,146	0,005	0,192	0,163

FeO_t – total iron in FeO. Mineral types are described in detail in Appendix 1.
* – ovegrowth on $St1_A$
** – ovegrowth on $Bt1_A$

Tab. 5 Whole rock composition of andalusite-biotite-sillimanite schist from Kovács-árok. *1,2* – And-Sill-Bt micaschist from Kisházi and Ivancsics (1985), *3* – banded micaschist from the side-valley of Kovács-árok (Kisházi and Ivancsics, 1985), *V* – KA-I-wr01 average sample measured by ICP-OES, this study; used as bulk rock composition in Stage1, *P, A* – modified bulk rock compositions calculated for Stage2 and Stage3, respectively.

	1	2	3	V	P	A
SiO_2	63,02	75,83	57,43	68,00	68,94	69,25
TiO_2	1,07	1,00	1,30	0,85	0,87	0,88
Al_2O_3	19,29	11,97	22,99	16,60	16,71	16,19
Fe_2O_3	1,38	0,98	1,85	5,68		
FeO	5,44	2,33	4,77		4,85	4,88
MnO				0,06	0,03	0,03
MgO	2,06	1,54	1,86	1,54	1,55	1,57
CaO	0,24	0,32	0,27	0,30	0,28	0,29
Na_2O	0,95	0,93	1,61	1,12	1,14	1,17
K_2O	4,50	3,35	4,23	3,72	3,80	3,88
P_2O_5	<0,01	-	0,01	<0,15		
SO_3				<0,15		
BaO				0,08		
SrO				0,01		
H_2O	2,37	1,44	3,31	1,80	1,84	1,86
Total	100,32	99,69	99,63	99,77	100,00	100,00

1, 2 - And-Sill-Bt micaschist from Kisházi and Ivancsics (1985)
3 - banded micaschist from the side-valley of Kovács-árok (Kisházi and Ivancsics, 1985)
V - KA-I-wr01 average sample measured by ICP-OES, this study; used as bulk rock composition in Stage1
P, A – modified bulk rock compositions calculated for Stage2 and Stage3, respectively

Tab. 6 Sm-Nd isotopic data from whole rock and garnet of sample KA-1.

Sample	Material	Sm [ppm]	Nd [ppm]	$^{147}Sm/^{144}Nd$	$^{143}Nd/^{144}Nd$	2Sd(m)	Age [Ma]
KA-1	WR	9,719	53,36	0,1101	0,511857	0,000004	
KA-1	Grt-C1	4,393	0,687	3,8727	0,519988	0,000005	
KA-1	Grt-C2	5,223	5,938	0,5318	0,512771	0,000003	330.4 ± 2.7

Tab. 7 Rb-Sr isotopic data from whole rock and biotite of sample KA-1.

Sample	Material	Rb [ppm]	Sr [ppm]	$^{87}Rb/^{86}Sr$	$^{87}Sr/^{86}Sr$	2Sd(m)	Age [Ma]
KA-1	WR	150	90,0	4,837	0,74743	0,000004	
KA-1	Bt	562	4,49	401,2	1,80172	0,000013	187.1 ± 1.9

Line Figure

Click here to download Line Figure Fig1_Degi et al 2018_Sopron.jpg

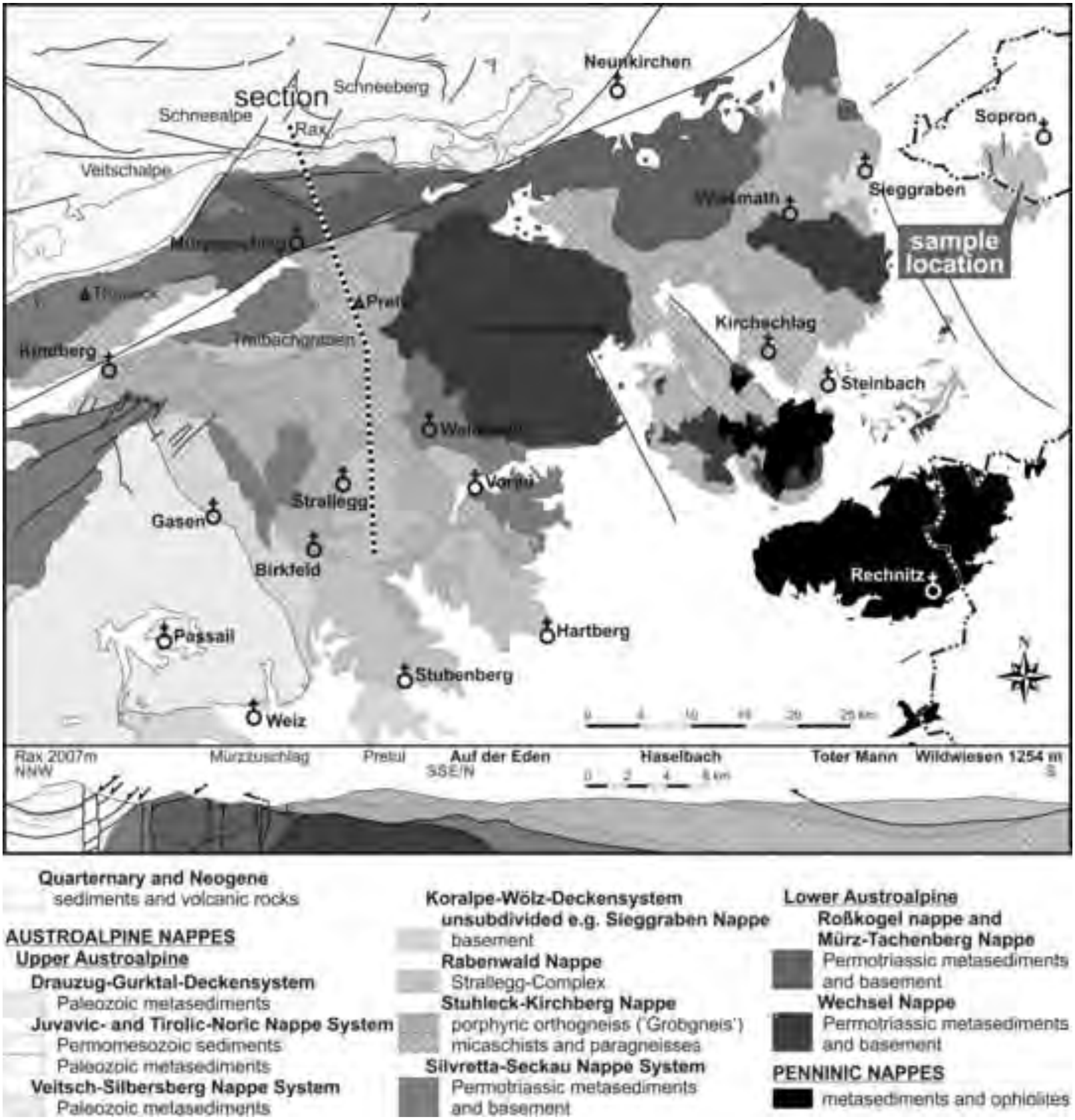

Colour Figure

Click here to download Colour Figure Fig2_Degi et al 2018_Sopron.jpg

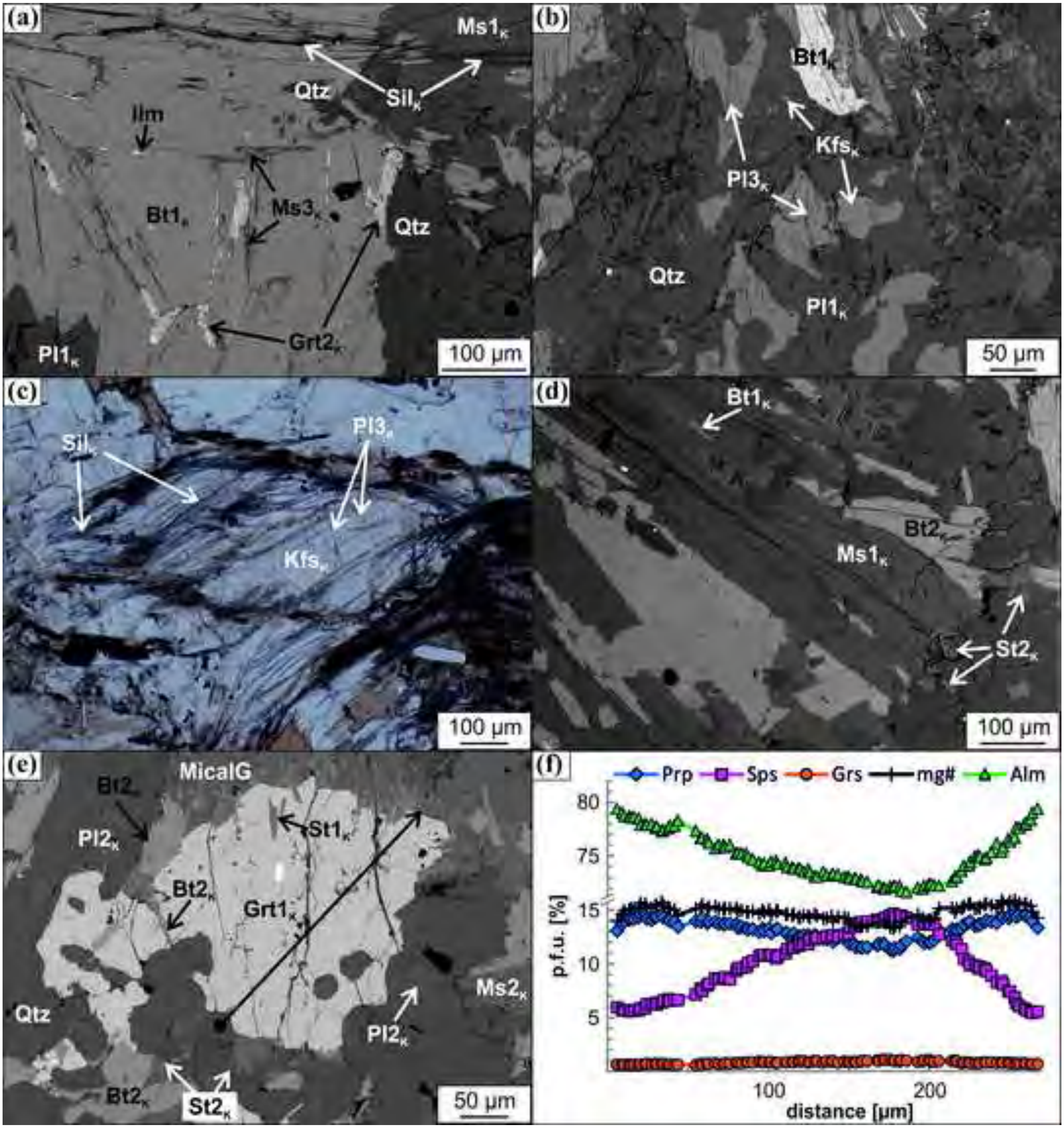

Colour Figure

Click here to download Colour Figure Fig3_Degi et al 2018_Sopron.jpg

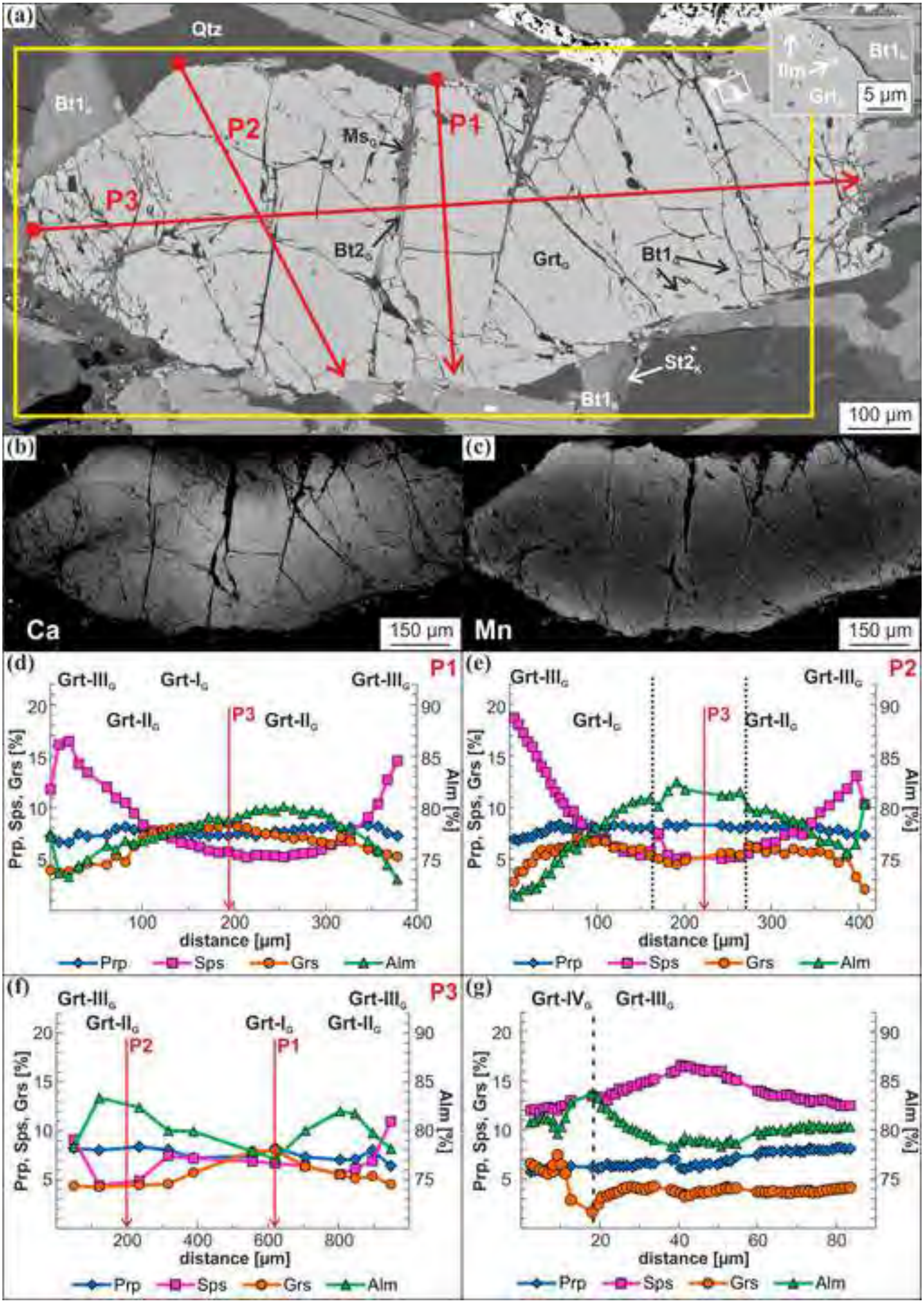

Colour Figure

Click here to download Colour Figure Fig4_Degi et al 2018_Sopron.jpg

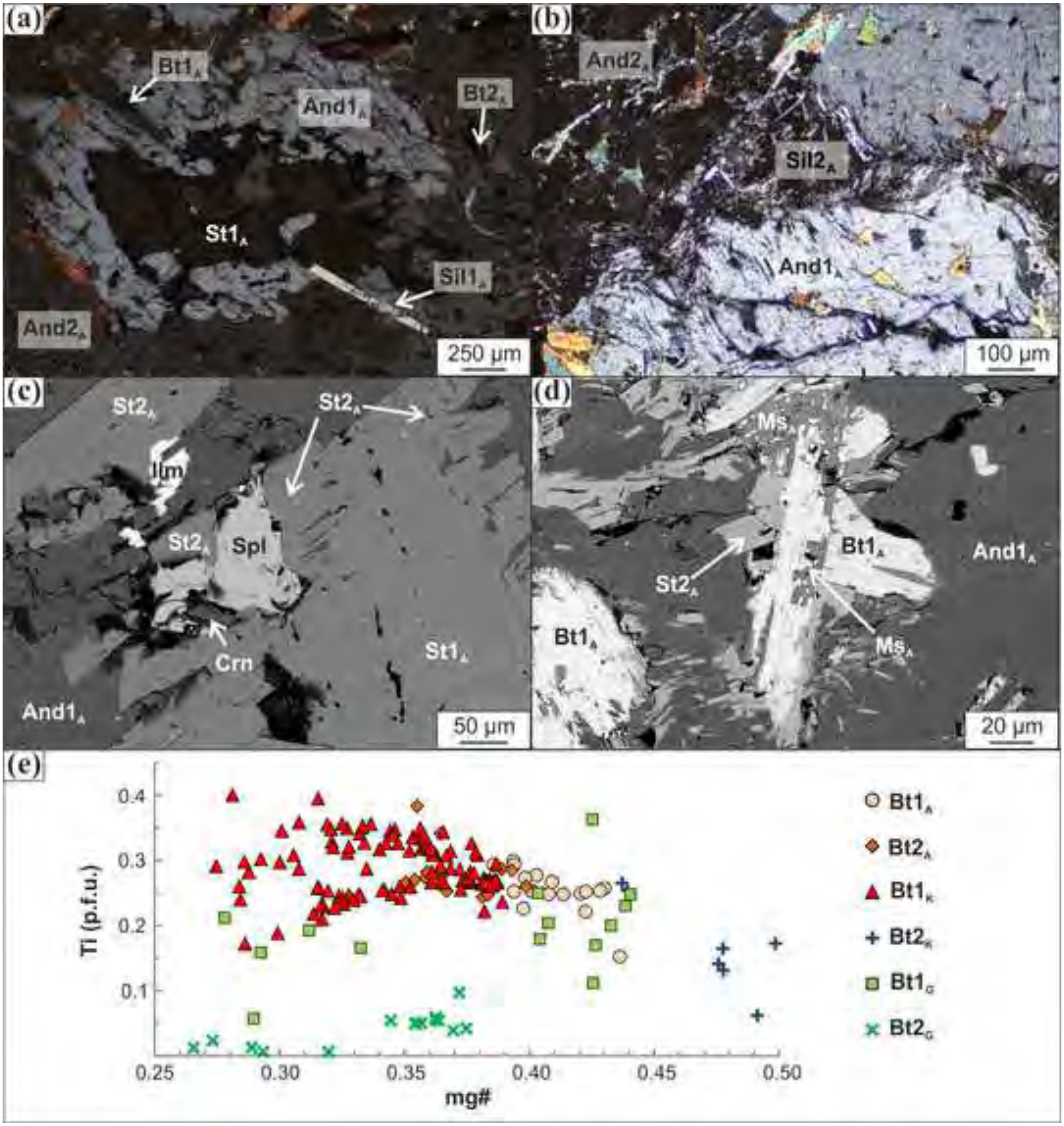

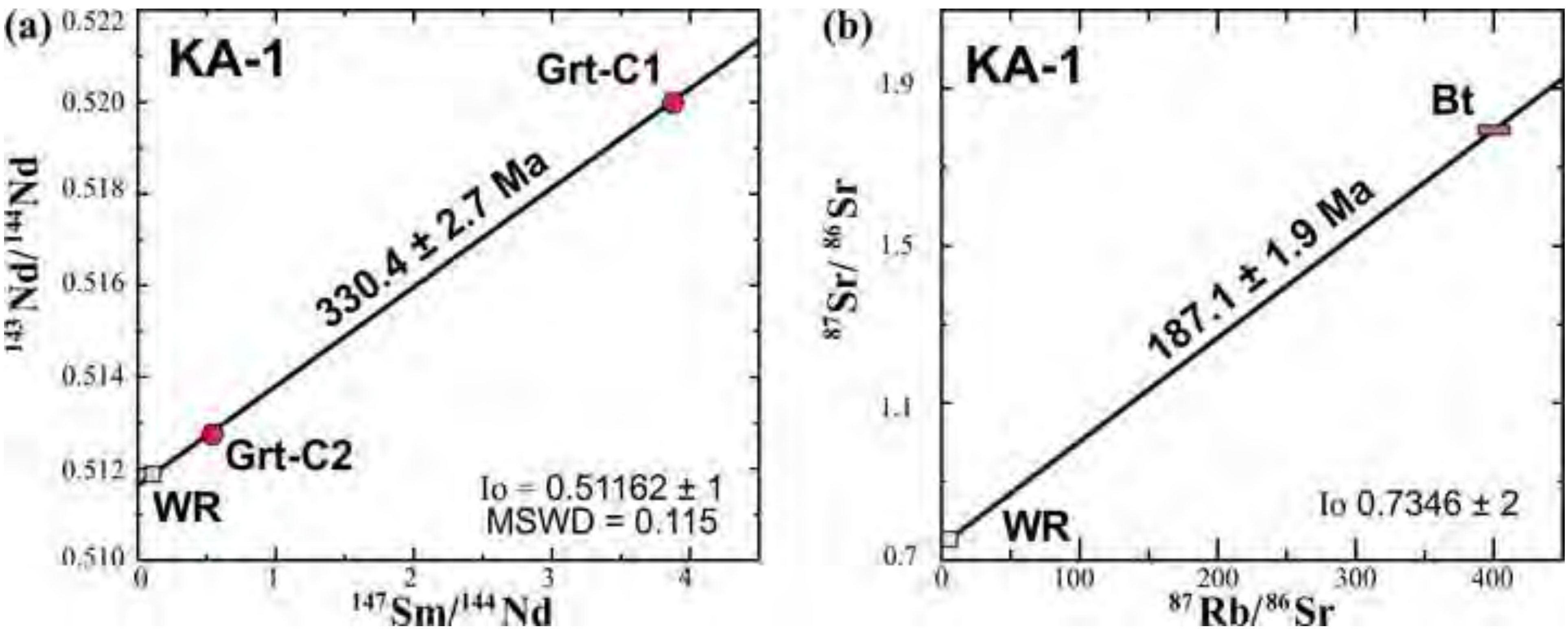

(a)
KA-1
Grt-C1
330.4 ± 2.7 Ma
Grt-C2
WR
Io = 0.51162 ± 1
MSWD = 0.115
143Nd/144Nd
147Sm/144Nd
0.522
0.520
0.518
0.516
0.514
0.512
0.510
0
1
2
3
4
(b)
KA-1
Bt
187.1 ± 1.9 Ma
WR
Io 0.7346 ± 2
87Sr/86Sr
87Rb/86Sr
1.9
1.5
1.1
0.7
0
100
200
300
400

Colour Figure

Click here to download Colour Figure Fig6_Degi et al 2018_Sopron.jpg

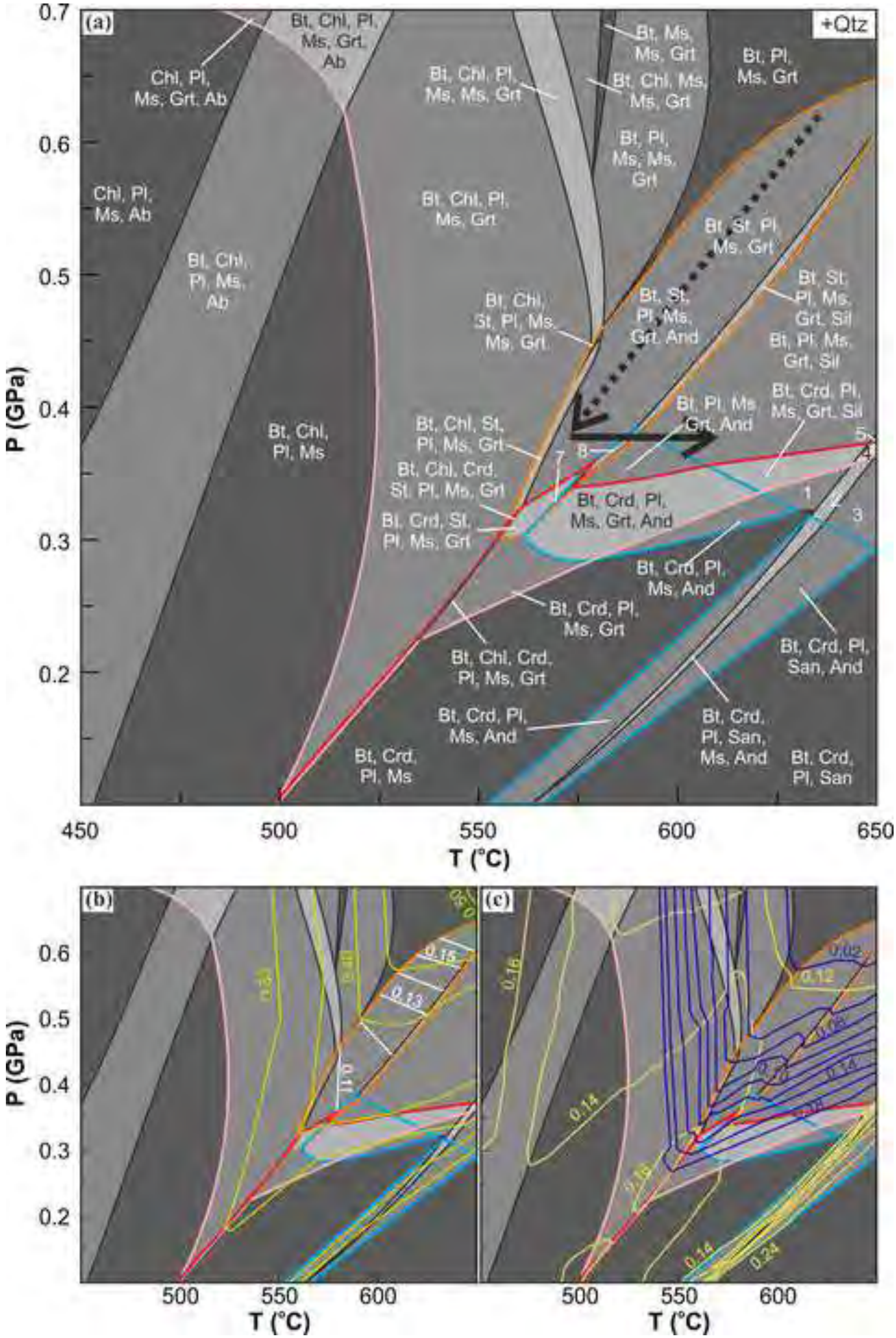

Colour Figure

Click here to download Colour Figure Fig7_Degi et al 2018_Sopron.jpg

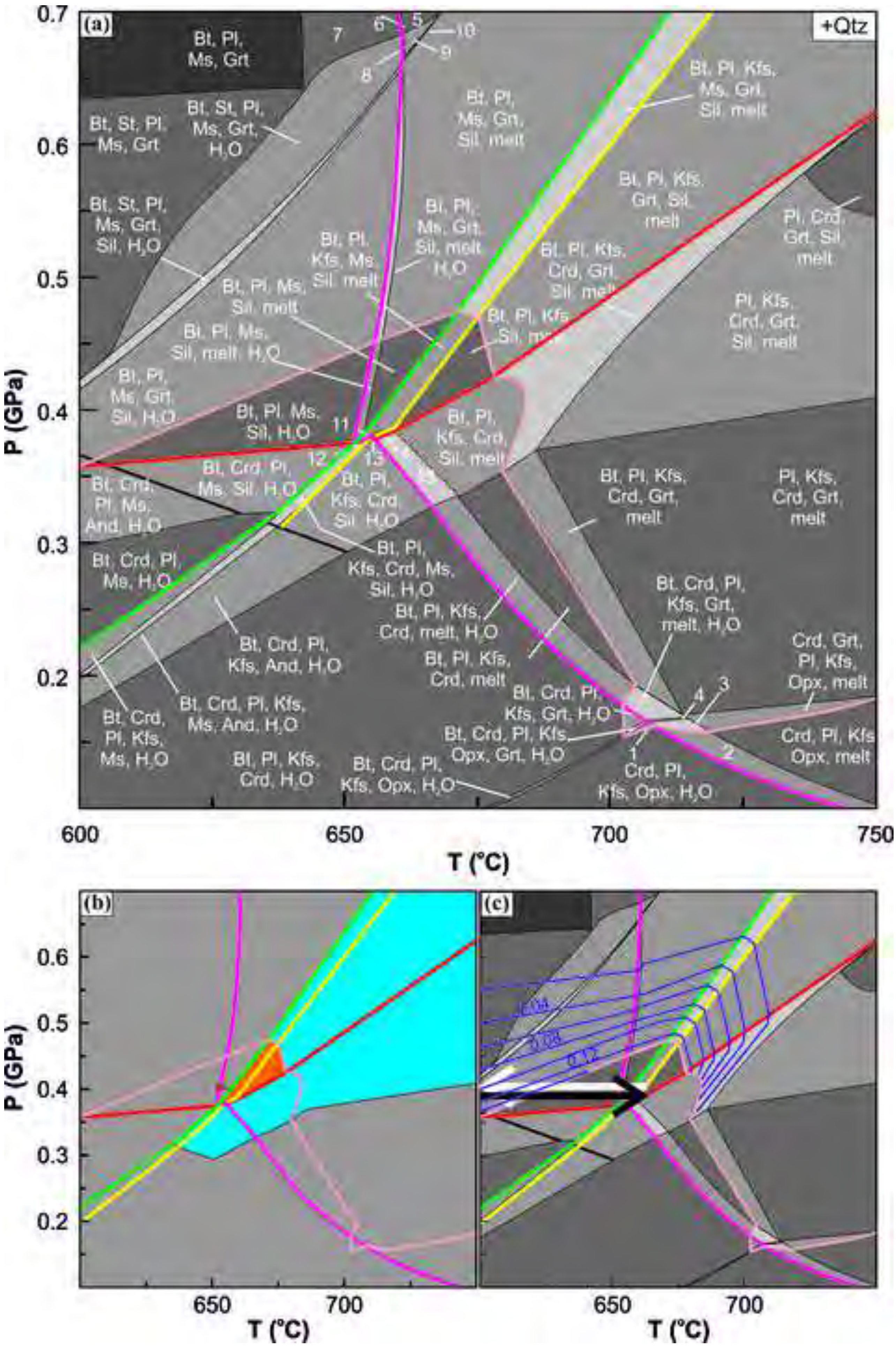

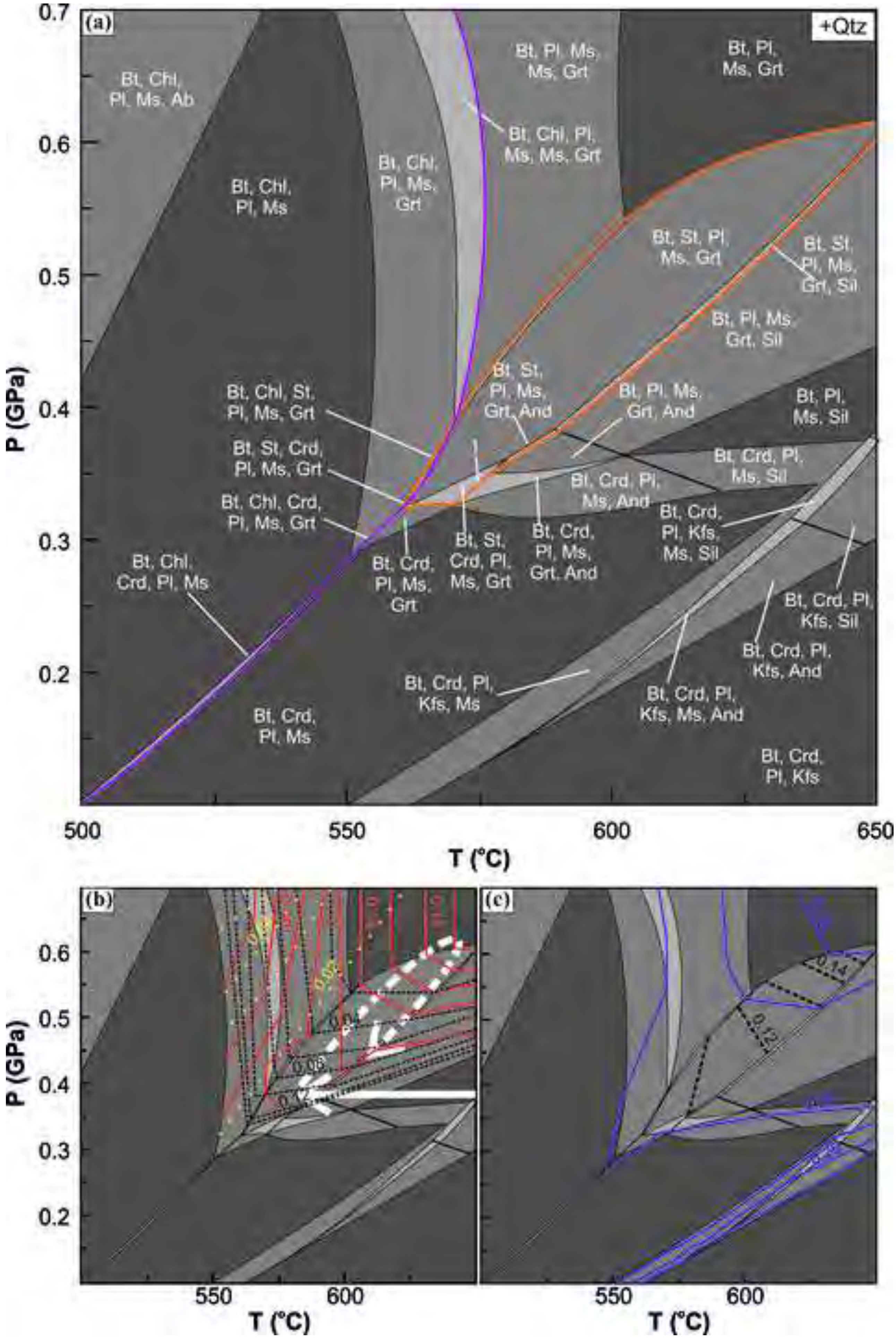
(a)
+Qtz
Bt, Chl, Pl, Ms, Ab
Bt, Chl, Pl, Ms
Bt, Chl, Pl, Ms, Grt
Bt, Pl, Ms, Ms, Grt
Bt, Chl, Pl, Ms, Ms, Grt
Bt, Pl, Ms, Grt
Bt, St, Pl, Ms, Grt
Bt, St, Pl, Ms, Grt, Sil
Bt, Pl, Ms, Grt, Sil
Bt, St, Pl, Ms, Grt, And
Bt, Pl, Ms, Grt, And
Bt, Pl, Ms, Sil
Bt, Chl, St, Pl, Ms, Grt
Bt, St, Crd, Pl, Ms, Grt
Bt, Chl, Crd, Pl, Ms, Grt
Bt, Crd, Pl, Ms, Sil
Bt, Crd, Pl, Ms, And
Bt, Crd, Pl, Kfs, Ms, Sil
Bt, Chl, Crd, Pl, Ms
Bt, Crd, Pl, Ms, Grt
Bt, St, Crd, Pl, Ms, Grt
Bt, Crd, Pl, Ms, Grt, And
Bt, Crd, Pl, Kfs, Sil
Bt, Crd, Pl, Kfs, And
Bt, Crd, Pl, Kfs, Ms
Bt, Crd, Pl, Kfs, Ms, And
Bt, Crd, Pl, Ms
Bt, Crd, Pl, Kfs
P (GPa)
0.7
0.6
0.5
0.4
0.3
0.2
500
550
600
650
T (°C)
(b)
0.06
0.1
0.14
(c)
0.14
0.12
550
600
T (°C)

Colour Figure Click here to download Colour Figure Fig9_Degi et al 2018_Sopron.jpg

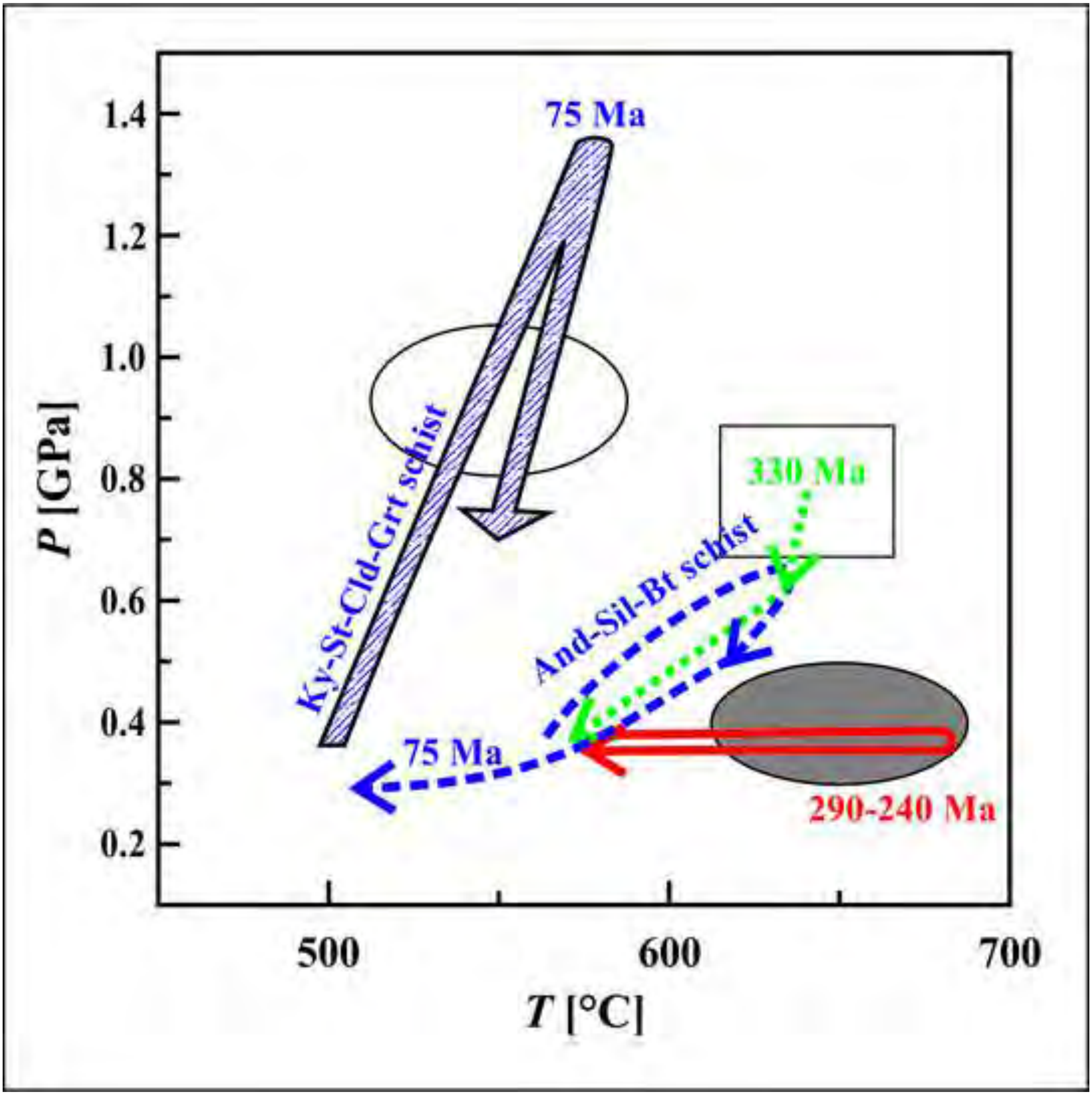

Tab. 1 Representative microprobe analyses of feldspar generations from the andalusite-sillimanite-biotite schist

Type	Kfs_K	Kfs_K	$Pl1_K$*	$Pl1_K$	$Pl1_K$	$Pl2_K$	$Pl3_K$
SiO_2	64.21	63.40	63.95	63.54	62.71	64.28	66.20
Al_2O_3	18.57	18.65	22.03	23.00	23.01	22.55	20.95
FeO_t	0.02	0.10	0.00	0.06	0.37	0.16	0.06
CaO	0.02	0.01	2.87	3.68	3.90	2.80	1.74
Na_2O	0.71	0.64	9.32	8.93	9.50	9.40	10.05
K_2O	15.82	15.85	0.24	0.16	0.09	0.04	0.16
Total	99.35	98.65	98.41	99.37	99.60	99.23	99.16
Si	2.985	2.973	2.856	2.816	2.789	2.846	2.923
Al	1.018	1.031	1.160	1.201	1.206	1.177	1.090
Fe	0.001	0.004	0.000	0.002	0.014	0.006	0.002
Ca	0.001	0.000	0.138	0.175	0.186	0.133	0.082
Na	0.064	0.058	0.807	0.768	0.820	0.807	0.860
K	0.938	0.948	0.014	0.009	0.005	0.002	0.009
Total	5.007	5.015	4.975	4.971	5.020	4.971	4.966
Ab	0.064	0.058	0.842	0.807	0.811	0.857	0.904
An	0.001	0.000	0.144	0.184	0.184	0.141	0.086
Or	0.935	0.942	0.014	0.009	0.005	0.002	0.010

FeO_t – total iron in FeO. Feldspar types are described in detail in Appendix 1.

$Pl1_K$* – plagioclase core further from Kfs-Sill-bearing assemblages

Feldspar types are described in detail in Appendix 1.

Tab. 2 Representative microprobe analyses of mica generations from andalusite-sillimanite-biotite schist

	Garnet porphyroblasts			Andalusite porphyroblasts			Kfs-Pl-Sill-Bt-rich bands					
Type	$Bt1_G$	$Bt2_G$	Ms_G	$Bt1_A$	$Bt2_A$	Ms_A	$Bt1_K$	$Bt2_K$	$Bt2_K$*	$Ms1_K$	$Ms2_K$	$Ms3_K$
SiO_2	35.29	34.54	48.95	34.84	34.33	46.20	33.24	35.19	33.43	45.06	45.63	47.35
TiO_2	1.84	0.48	0.20	2.18	2.71	0.52	2.77	0.19	0.54	0.38	0.08	0.65
Al_2O_3	20.25	22.20	31.80	20.53	20.46	36.22	19.87	22.18	22.61	36.55	36.86	34.63
FeO_t	20.65	22.18	2.59	20.45	21.59	1.12	21.41	16.31	19.11	0.87	0.87	1.23
MnO	0.24	0.24	0.10	0.15	0.10	0.02	0.13	0.02	0.20	0.01	0.03	0.00
MgO	8.64	7.12	2.03	8.33	6.84	0.66	7.27	11.49	10.36	0.62	0.67	0.66
CaO	0.02	0.06	0.03	0.00	0.12	0.09	0.11	0.05	0.07	0.20	0.06	0.02
Na_2O	0.09	0.05	0.12	0.11	0.13	0.35	0.24	0.18	0.11	0.48	0.42	0.19
K_2O	8.64	9.29	9.76	9.37	9.13	9.66	9.01	9.33	8.17	9.96	9.98	10.54
F	0.00	0.00	0.00	0.00	0.00	0.02	0.00	0.07	0.00	0.02	0.05	0.01
Cl	0.00	0.04	0.01	0.07	0.00	0.01	0.04	0.02	0.04	0.02	0.00	0.00
Total	95.66	96.19	95.57	96.03	95.41	94.87	94.09	95.02	94.64	94.18	94.65	95.28
Si	5.350	5.260	6.485	5.287	5.268	6.132	5.197	5.272	5.085	6.044	6.079	6.281
Ti	0.210	0.055	0.020	0.249	0.313	0.052	0.326	0.022	0.062	0.039	0.008	0.065
Al	3.619	3.986	4.965	3.672	3.702	5.666	3.661	3.917	4.053	5.779	5.789	5.415
Fe	2.618	2.825	0.287	2.595	2.771	0.124	2.800	2.043	2.431	0.098	0.096	0.137
Mn	0.030	0.031	0.011	0.019	0.013	0.002	0.017	0.003	0.026	0.001	0.003	0.000
Mg	1.952	1.616	0.401	1.884	1.566	0.131	1.694	2.565	2.349	0.124	0.134	0.130
Ca	0.003	0.010	0.004	0.000	0.020	0.013	0.018	0.008	0.011	0.029	0.008	0.003
Na	0.026	0.013	0.030	0.031	0.038	0.091	0.074	0.051	0.032	0.126	0.109	0.049
K	1.670	1.806	1.650	1.813	1.789	1.636	1.797	1.784	1.586	1.705	1.696	1.783
F	0.000	0.000	0.000	0.000	0.000	0.007	0.000	0.031	0.000	0.010	0.022	0.004
Cl	0.000	0.009	0.001	0.019	0.001	0.001	0.012	0.005	0.011	0.005	0.001	0.000
Sum	15.479	15.612	13.854	15.569	15.481	13.855	15.596	15.700	15.645	13.959	13.945	13.866
mg#	0.43	0.36	0.58	0.42	0.36	0.51	0.38	0.56	0.49	0.56	0.58	0.49
Phl	0.57	0.64		0.58	0.64		0.62	0.44	0.51			
Ann	0.43	0.36		0.42	0.36		0.38	0.56	0.49			
Ms			0.60			0.81				0.82	0.83	0.81
Marg			0.00			0.01				0.02	0.00	0.00
Pg			0.02			0.05				0.07	0.06	0.03
Mg-Cel			0.04			0.02				0.03	0.03	0.00
Fe-Cel			0.17			0.07				0.05	0.05	0.07
Pheng			0.17			0.04				0.01	0.02	0.08

FeO_t – total iron in FeO. Mica types are described in detail in Appendix 1.

* – inclusion found in the rim of $Grt1_K$

Tab. 3 Representative garnet microprobe analyses from andalusite-sillimanite-biotite schist

Type	Garnet porphyroblasts					Ksp-Pl-Sill-Bt-rich bands		
	Grt-I_G	Grt-II_G	Grt-III_G	Grt-IV_G	Grt-IV_G	Grt1_K core	Grt1_K rim	Grt2_K
SiO_2	38.43	37.98	37.25	38.02	37.83	37.34	37.66	36.19
TiO_2	0.01	0.03	0.02	0.09	0.13	0.00	0.00	1.95
Al_2O_3	20.89	21.49	21.31	21.42	21.45	22.02	22.18	21.19
FeO_t	35.55	35.22	31.55	34.16	35.53	33.15	35.29	33.07
MnO	2.10	3.81	7.89	5.12	4.51	6.08	2.57	6.91
MgO	1.63	1.85	1.68	1.66	1.56	2.90	3.70	1.53
CaO	3.19	2.05	1.29	1.77	0.53	0.29	0.26	0.85
Total	101.80	102.43	100.99	102.24	101.53	101.78	101.67	101.70
Si	3.051	3.005	2.997	3.014	3.022	2.965	2.973	2.905
Ti	0.000	0.002	0.001	0.006	0.008	0.000	0.000	0.118
Al	1.955	2.005	2.021	2.002	2.020	2.061	2.064	2.005
Fe	2.361	2.331	2.123	2.265	2.374	2.201	2.330	2.220
Mn	0.141	0.256	0.538	0.344	0.306	0.409	0.172	0.470
Mg	0.193	0.218	0.202	0.196	0.186	0.344	0.435	0.183
Ca	0.272	0.174	0.111	0.150	0.045	0.024	0.022	0.073
Sum	7.972	7.990	7.992	7.976	7.959	8.004	7.995	7.975
Prp	0.07	0.07	0.07	0.07	0.06	0.12	0.15	0.06
Alm	0.80	0.78	0.71	0.77	0.82	0.74	0.79	0.75
Sps	0.05	0.09	0.18	0.12	0.10	0.14	0.06	0.16
Grs	0.09	0.06	0.04	0.05	0.02	0.01	0.01	0.02

FeO_t – total iron in FeO. Garnet types are described in detail in Appendix 1.

Tab. 4 Representative microprobe analyses of staurolite generations and oxides from andalusite-sillimanite-biotite schists

	Andalusite porphyroblasts					Kfs-Pl-Sill-Bt-rich bands		
Type	Spl	$St1_A$	$St1_A$	$St2_A$*	$St2_A$**	Ilm	$St1_K$	$St2_K$
SiO_2	0.02	27.22	27.18	27.31	29.84	0.07	27.44	28.44
TiO_2	0.11	0.92	0.82	0.56	0.04	53.06	0.03	0.02
Al_2O_3	60.17	54.33	54.54	54.32	54.70	0.30	56.01	56.67
FeO_t	23.36	12.91	12.62	13.17	11.91	41.74	12.72	11.78
MnO	0.31	0.40	0.38	0.38	0.37	1.93	0.21	0.33
MgO	2.81	1.36	1.35	1.44	1.15	0.11	1.69	1.29
CaO	0.02	0.02	0.02	0.00	0.01	0.02	0.01	0.01
ZnO	14.03	1.34	1.46	1.21	0.44	0.07	0.65	0.65
Total	100.82	98.50	98.37	98.39	98.45	97.30	98.75	99.19
Si	0.000	3.769	3.764	3.785	4.067	0.002	3.761	3.855
Ti	0.002	0.096	0.086	0.058	0.004	1.021	0.003	0.002
Al	2.000	8.865	8.901	8.873	8.785	0.009	9.048	9.053
Fe	0.551	1.495	1.461	1.526	1.357	0.893	1.458	1.335
Mn	0.007	0.047	0.044	0.045	0.043	0.042	0.025	0.038
Mg	0.118	0.280	0.278	0.298	0.233	0.004	0.345	0.260
Ca	0.001	0.002	0.003	0.000	0.001	0.001	0.001	0.001
Zn	0.292	0.137	0.149	0.123	0.044	0.001	0.065	0.065
Sum	2.971	14.690	14.687	14.709	14.533	1.973	14.706	14.611
mg#	0.177	0.158	0.160	0.163	0.146	0.005	0.192	0.163

FeO_t – total iron in FeO. Mineral types are described in detail in Appendix 1.

* – ovegrowth on $St1_A$

** – ovegrowth on $Bt1_A$

Table Click here to download Table Tab5_Degi et al 2018_Sopron.xlsx

Tab. 5 Measured whole rock compositions of andalusite-l sillimanite schist from Kovács-árok and derivation composiitons for different stages of metamorphic (

	1	2	3	V	P	A
SiO_2	63.02	75.83	57.43	68.00	68.94	69.25
TiO_2	1.07	1.00	1.30	0.85	0.87	0.88
Al_2O_3	19.29	11.97	22.99	16.60	16.71	16.19
Fe_2O_3	1.38	0.98	1.85	5.68		
FeO	5.44	2.33	4.77		4.85	4.88
MnO				0.06	0.03	0.03
MgO	2.06	1.54	1.86	1.54	1.55	1.57
CaO	0.24	0.32	0.27	0.30	0.28	0.29
Na_2O	0.95	0.93	1.61	1.12	1.14	1.17
K_2O	4.50	3.35	4.23	3.72	3.80	3.88
P_2O_5	<0,01	-	0.01	<0,15		
SO_3				<0,15		
BaO				0.08		
SrO				0.01		
H_2O	2.37	1.44	3.31	1.80	1.84	1.86
Total	100.32	99.69	99.63	99.77	100.00	100.00

1, 2 - And-Sill-Bt micaschist from Kisházi and Ivancsics (1!
3 - banded micaschist from the side-valley of Kovács-árok and Ivancsics, 1985)
V - KA-I-wr01 average sample measured by ICP-OES, this used as bulk rock composition in Stage1
P, A – modified bulk rock compositions calculated for Stag Stage3, respectively

biotite-
of bulk
evolution

985)
(Kisházi

s study;

e2 and

Tab. 6 Sm-Nd isotopic data from whole rock and garnet of sample KA-1

Sample	Material	Sm [ppm]	Nd [ppm]	$^{147}Sm/^{144}Nd$	$^{143}Nd/^{144}Nd$	2Sd(m)	Age [Ma]
KA-1	WR	9.719	53.36	0.1101	0.511857	0.000004	
KA-1	Grt-C1	4.393	0.687	3.8727	0.519988	0.000005	
KA-1	Grt-C2	5.223	5.938	0.5318	0.512771	0.000003	330.4 ± 2.7

Tab. 7 Rb-Sr isotopic data from whole rock and biotite of sample KA-1

Sample	Material	Rb [ppm]	Sr [ppm]	$^{87}Rb/^{86}Sr$	$^{87}Sr/^{86}Sr$	2Sd(m)	Age [Ma]
KA-1	WR	150	90.0	4.837	0.74743	0.000004	
KA-1	Bt	562	4.49	401.2	1.80172	0.000013	187.1 ± 1.9

Appendix 1 Mineral generations distinguished in the andalusite-sillimanite-biotite schist G, A and K in the bottom righ index stands for garnet porphyroblasts, andalusite prophyroblasts and Kfs-Pl-Sil-Bt-rich bands

Grt_G	garnet porphyroblast
$Grt\text{-}I_G$	inclusion-free Ca-rich core of Grt_G
$Grt\text{-}II_G$	Fe-rich inner zone of Grt_G containing numerous biotite inclusions
$Grt\text{-}III_G$	Mn-rich outer zone of Grt_G containing numerous biotite inclusions
$Grt\text{-}IV_G$	the outermost zone of Grt_G containing oriented ilmenite inclusions; appearing just in contact with $Bt1_K$
$Bt1_G$	euhedral biotite inclusions in Grt_G
$Bt2_G$	biotite inclusions in Grt_G related to cracks, associated with Ms_G
Ms_G	muscovite inclusions in Grt_G related to cracks, associated with $Bt2_G$
$Bt1_K$	large biotite flakes containing ilmenite inclusions
$Pl1_K$	large poikilitic feldspar containing Kfs_K and quartz inclusions
Kfs_K	K-feldspar grains found as poikilitic inclusions in $Pl1_K$ or as individual grains frequently intergrown with Sil_K
Sil_K	fibrous sillimanite sometimes intergrown with Kfs_K or large micas ($Ms1_K$, $Bt1_K$)
$Ms1_K$	large muscovite flakes containing relics of $Bt1_K$
$Grt1_K$	several hundred micron wide euhedral garnet grains holding microstructural equilibrium with $St1_K$, $Ms2_K$, $Bt2_K$ and $Pl2_K$
$St1_K$	staurolite laths found as inclusion in the rim of $Grt1_K$
$Ms2_K$	small muscovite laths found in equilibrium with $Grt1_K$, $St1_K$ and $Bt2_K$
$Bt2_K$	inclusion-free bitotite laths found in equilibrium with $Grt1_K$, $St1_K$ and $Ms2_K$
$Grt2_K$	small garnet grains grown along cracks and grian boundaries of $Bt1_K$ biotite
$Ms3_K$	muscovite grown along cracks within the $Bt1_K$ biotite
$Pl3_K$	albitic lamellae in Kfs_K
$Pl2_K$	small plagioclase in equilibrium with $Grt1_K$, $St1_K$, $Ms2_K$ and $Bt2_K$
$MicaIG_K$	submicron scale intergrowths of biotite and white micas apeearing in nests in Kfs-Pl-Sil-Bt-rich bands
$St2_K$	smaller, euhedral staurolite laths or twins found as overgrowths on $Ms1_K$ muscovites, on $Bt1_K$ biotite, along cracks and in nests filled by ultrafine-grained alteration products
$And1_A$	inclusion-rich andalusite porphyroblasts showing mosaic extinction in optical microscope, frequently overprinted by $Sil2_A$
$And2_A$	undeformed andalusite generation where inclusions are restricted to biotite and quartz
$Sil1_A$	fibrous sillimanite found around $And1_A$ or in between $And1_A$ and $And2_A$
$Sil2_A$	fibrous sillimanite found around $And1_A$ or in between $And1_A$ and $And2_A$
$St1_A$	several hundreds or tens of µm sized anhedral staurolite inclusions in $And1_A$
$Bt1_A$	biotite inclusions preserved in $And1_A$

$Bt2_A$	biotite inclusions found in $And2_A$ together with quartz
$St2_A$	10 µm long, 2-5 µm wide poikilitic staurolite laths overgrown on St1A, Bt1A or spinel showing different optical orientation
Ms_A	muscovite replacing biotite within andalusite inclusions

Attachment to Manuscript

Click here to download Attachment to Manuscript Sopron_3phase_OR1.jpg

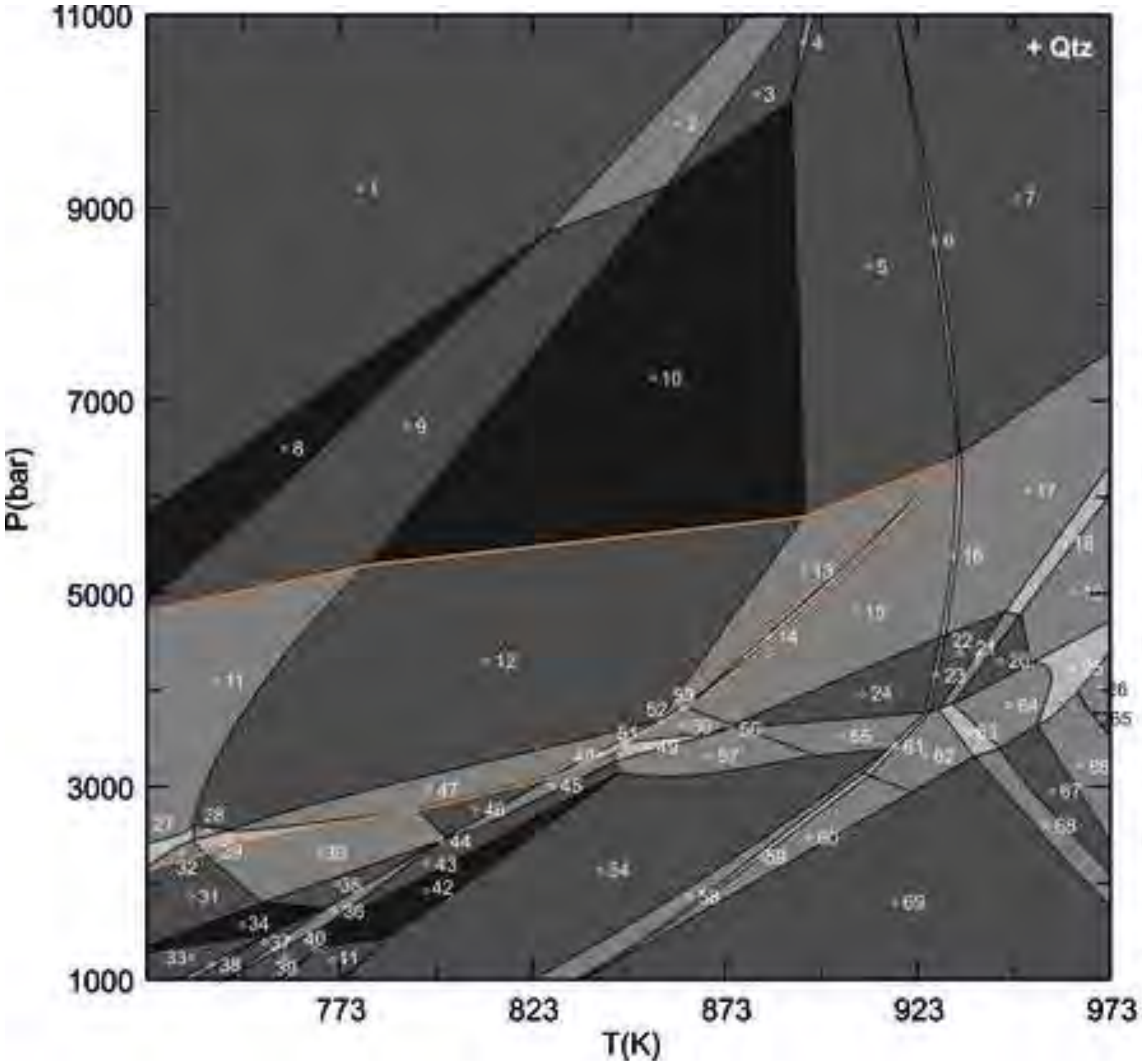

1	Bt Ms Ms Grt Ab
2	Bt Fsp Ms Ms Grt Ab
3	Bt Fsp Ms Ms Grt
4	Bt Fsp Ms Ms Grt H_2O
5	Bt Fsp Ms Grt H_2O
6	Bt melt Fsp Ms Grt H_2O
7	Bt melt Fsp Ms Grt
8	Bt Ms Grt Ab
9	Bt Fsp Ms Grt Ab
10	Bt Fsp Ms Grt
11	Bt St Fsp Ms Grt Ab
12	Bt St Fsp Ms Grt
13	Bt St Fsp Ms Grt H_2O
14	Bt St Fsp Ms Grt Sil H_2O
15	Bt Fsp Ms Grt Sil H_2O
16	Bt melt Fsp Ms Grt Sil H_2O
17	Bt melt Fsp Ms Grt Sil
18	Bt melt Fsp Fsp Ms Grt Sil
19	Bt melt Fsp Fsp Grt Sil
20	Bt melt Fsp Fsp Sil
21	Bt melt Fsp Fsp Ms Sil
22	Bt melt Fsp Ms Sil
23	Bt melt Fsp Ms Sil H2O
24	Bt Fsp Ms Sil H2O
25	Bt melt Crd Fsp Fsp Grt Sil
26	melt Crd Fsp Fsp Grt Sil
27	Bt St Fsp Ms Grt And Ab
28	Bt St Fsp Ms Ms Grt
29	Bt St Fsp Ms Ms Grt And
30	Bt Fsp Ms Ms Grt And
31	Bt Fsp Ms Grt And
32	Bt St Fsp Ms Grt And
33	Bt Chl Fsp Ms And
34	Bt Fsp Ms And
35	Bt Fsp Ms Ms And

36	Bt Crd Fsp Ms Ms And
37	Bt Crd Fsp Ms And
38	Bt Chl Crd Fsp Ms And
39	Bt Crd Fsp Ms Ms
40	Bt Chl Crd Fsp Ms Ms
41	Bt Chl Crd Fsp Ms
42	Bt Crd Fsp Ms
43	Bt Crd Fsp Ms And
44	Bt Crd Fsp Ms Ms Grt And
45	Bt Crd Fsp Ms Grt And
46	Bt Fsp Ms Grt And
47	Bt St Fsp Ms Grt And
48	Bt St Crd Fsp Ms Grt And
49	Bt Crd Fsp Ms Grt And H_2O
50	Bt Fsp Ms Grt And H_2O
51	Bt St Crd Fsp Ms Grt And H_2O
52	Bt St Fsp Ms Grt And
53	Bt St Fsp Ms Grt And H_2O
54	Bt Crd Fsp Ms H_2O
55	Bt Crd Fsp Ms Sil H_2O
56	Bt Fsp Ms And H_2O
57	Bt Crd Fsp Ms And H_2O
58	Bt Crd Fsp Fsp Ms H_2O
59	Bt Crd Fsp Fsp Ms And H_2O
60	Bt Crd Fsp Fsp And H_2O
61	Bt Crd Fsp Fsp Ms Sil H_2O
62	Bt Crd Fsp Fsp Sil H_2O
63	Bt melt Crd Fsp Fsp Sil H_2O
64	Bt melt Crd Fsp Fsp Sil
65	melt Crd Fsp Fsp Grt
66	Bt melt Crd Fsp Fsp Grt
67	Bt melt Crd Fsp Fsp
68	Bt melt Crd Fsp Fsp H_2O
69	Bt Crd Fsp Fsp H_2O

Refinement of the evolution history of garnet (from Grobgneiss of Kő-hegy, Sopron Mountains, Hungary) based on major- and trace-element studies by EMPA, micro-PIXE and LA-ICP-MS.

Török, K., Király, E., Dégi, J., Kertész, Zs., Abart, R., Maigut V.

Abstract

We studied garnets from the high pressure/medium temperature orthogneiss and a coarse grained pegmatitic nest from the Kő-hegy, (Sopron Mountains, Hungary) by means of EMPA, LA-ICP-MS and Micro PIXE to unravel a complex garnet growth during the magmatic and metamorphic history of the gneiss. Complex changes of major and trace elements in the garnets enabled us to reveal the processes that operated during garnet growth and thus to refine the magmatic and metamorphic evolution of the gneisses around Sopron. Garnets with complex magmatic and metamorphic zoning were found in a coarse grained pegmatitic nest. The magmatic history starts with the formation of the garnet cores (Z1), which are characterized by relatively high rare-earth element and Y (REY) content. The REY distribution shows enrichment of heavy rare earth elements (HREE-s). It is overgrown by a depleted zone with oscillatory zoning and the lowest REY-contents (Z2). The following zone (Z3) is distinguished by limited enrichment in Ca and trace elements and a finer scale oscillatory zoning, than in Z2. The evolution of magmatic garnet is completed with zone Z4, where depletion of Ti, Zr and Ca was observed. Oscillatory zoning in magmatic garnet is coupled with modified REY patterns (humpback distribution) relative to Z1 indicating non-equilibrium, probably open-system conditions, changes in growth rate and fractionation of heavy REE-s in the core (Z1). After partial resorption of the magmatic zones, 3 narrow zones (Z5-7) of Alpine metamorphic garnet are overgrown on the resorbed magmatic grain with distinctive Ca enrichment relative to the magmatic part. The REY distribution pattern changes again from humpback to increased heavy REE, similar to the Z1 and the REY content increases relative to Z4. The second metamorphic zone (Z6) with the highest Ca and decreasing REY content relative to Z5 represents the metamorphic peak pressure and temperature conditions. The last zone, Z7 is discontinuous and displays Mn and REY enrichment and is thought to belong to the Alpine retrograde phase. The highest concentrations of REY were detected in the limbs of this last zone developed in pressure shadows, which were interpreted as an effect of retrograde metamorphic fluids, which percolated the Grobgneiss.

Garnet from gneiss reveals different major (grossular content about 50%) and trace element geochemistry (low REE and Zn, high Ti), than either magmatic or metamorphic zones of pegmatitic nests. The main reason can be the difference in compositions of the local environment and/or the different garnet forming reactions.

Introduction

Several aspects of the metamorphic history of the metamorphic rocks belonging to the Austroalpine basement, outcropping in the Sopron Mountains were discussed in the last three decades. Previous authors first described low grade alpine metamorphism of orthogneisses (Lelkes-Felvári et al., 1984; Kisházi & Ivancsics, 1985, 1987a,b, 1989) using petrography, mineral and bulk rock chemistry. Later Alpine high pressure, medium temperature metamorphism was discovered and described for the orthogneiss (Török, 1996, 1998, 2001), leucophyllite (Demény et al, 1997) and micaschist (Török, 2003). The garnets of the gneisses in the Sopron Mountains were studied by Török (1996, 1998) in order to determine the implications of their major element chemistry to their origin. The EMPA study of garnets revealed an almandine-spessartine-rich magmatic and a grossular-almandine-rich metamorphic generation. However details of the formation of the different garnet generations remained elusive.

The recent discovery of complex composition zoning in garnets opened the way for further studies regarding the detailed garnet formation history in gneiss starting from magmatic through the high pressure metamorphic conditions. The previous studies only made the distinction between magmatic and metamorphic garnets, but in this paper we represent a much finer resolution of the development for the garnets. We studied zoned garnets from the coarse grained gneiss (further on referred to as pegmatite) and relatively fine grained foliated gneiss of the Kő-hegy quarry (Sopron, W-Hungary) by means of EMPA, LA-ICP-MS and Micro PIXE to reveal the complex magmatic and metamorphic history of gneiss belonging to the Austroalpine nappe system. We applied X-ray mapping for major and trace elements using EMPA and micro-PIXE to reveal the fine scale zoning of the garnets and to identify growth and resorption microtextures. Combining X-ray maps with major and trace element analyses of garnet allowed us to reconstruct the growth and resorption history of the garnet through its entire history. We also conducted experiments on LA-ICP-MS with smaller spot size of 30 and 8 μm to reveal small scale trace element zoning.

Geological background

The Sopron area hosts the easternmost outcrops of the Eastern Alps. The major rock types are medium grade micaschist, orthogneiss, leucophyllite and subordinate amphibolite (Lelkes-Felvári, 1984); Kisházi & Ivancsics, 1985, 1987a,b, 1989; Fig. 1.). The metamorphic rocks around Sopron extend to Austria and are thought to belong to the Grobgneiss unit of the Lower Austroalpine nappe system. However Draganits (1998) suggested that the Óbrennberg-Kaltes Bründl Series, which contains pre-Alpine andalusite-sillimanite-biotite schist, shows similarities to the Strallegger Gneiss and to the Dist-Paramorphosenschiefer (Koralpe), thus might belong to the Middle Austroalpine Unit. Age of the pre-Alpine events can only be reconstructed with uncertainty however, the age of the oldest recorded event is Variscan (310±34 Ma on monazite U-Pb-Th, 328.5±12.5 and 319.5±12.1 Ma on biotite K-Ar – Nagy et al. 2002, Balogh and Dunkl 2005) followed by a Permo-Triassic HT/LP event with ages of 275–236 Ma based on biotite K-Ar and on Ar-Ar age dating on muscovite by Balogh and Dunkl (2005). Several types of micaschists can be observed in the Sopron area. The most widespread type is the garnet-bearing chlorite-muscovite-quartz schist. Kyanite-staurolite-chloritoid-garnet bearing and kyanite-chloritoid-garnet-bearing micaschists also occur, mainly near Óbrennberg (Török, 1999, 2003). Mg-chlorite-muscovite-quartz ± kyanite schist (leucophyllite) is found in the shear zones of the micaschists and gneisses.

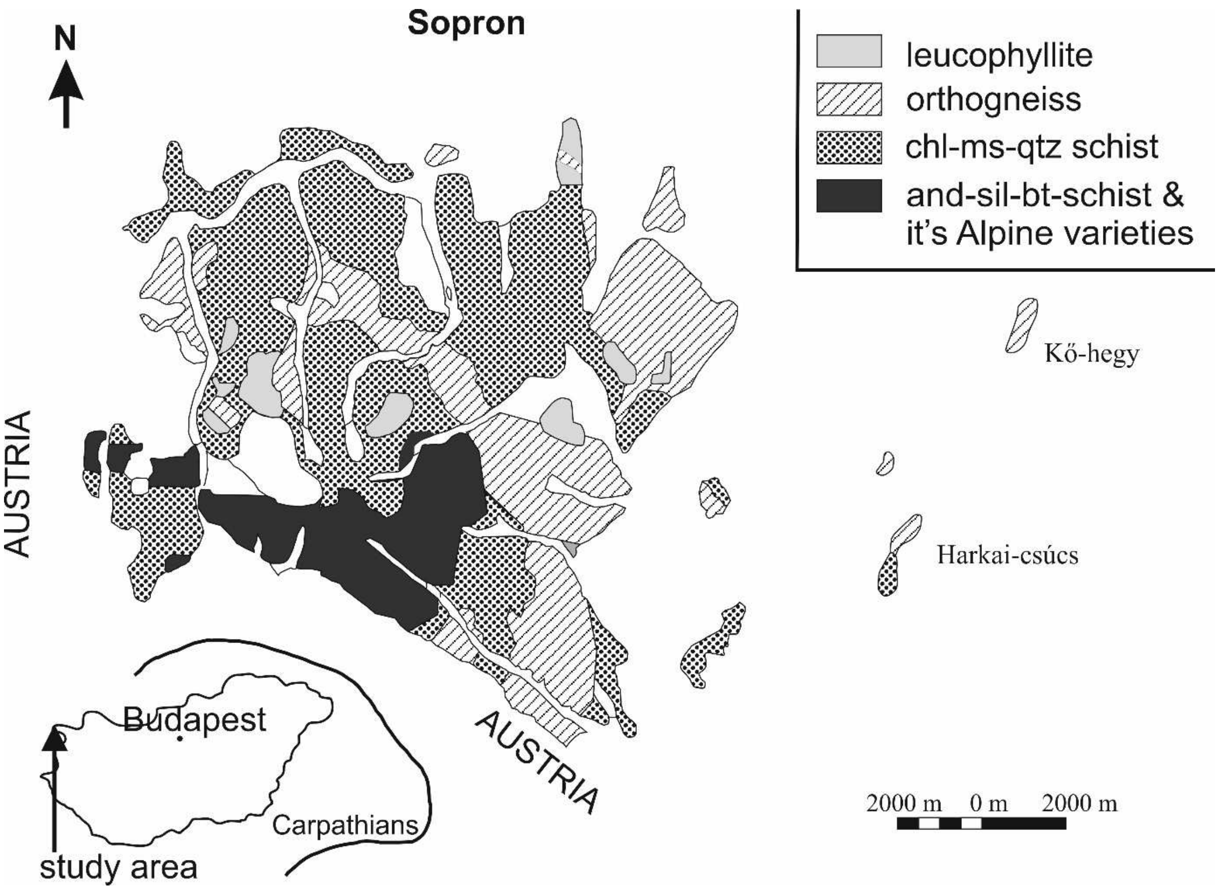

Figure 1. Scetch geologic map of the Sopron area.

Previous workers (e.g. Lelkes-Felvári et al., 1984; Kisházi & Ivancsics, 1985, 1987a,b, 1989) agreed that the gneisses of the Sopron area are of magmatic origin and experienced Alpine greenschist facies metamorphism. However Török (1996, 1998, 2003) has shown that the orthogneiss and the surrounding micaschists have undergone Alpine high-pressure, medium temperature (HP/MT) metamorphism at about 1.2–1.4 GPa and 580–600°C. Draganits (1998) obtained considerably lower pressures for the garnet-bearing chlorite-muscovite±biotite-quartz schist in the Austrian part of the Sopron area (0.95±0.15 GPa at 550±30°C). Demény et al. (1997) concluded that the mineral assemblage of the kyanite-bearing Mg-chlorite-muscovite-quartz schist (so called leucophyllite) has formed under similar high-pressure, medium temperature (HP/MT) conditions. The age of the Alpine metamorphism is Late Cretaceous (70–80 Ma) based on K-Ar and Ar-Ar age dating on biotite and on white mica, as well as on the basis of U-Pb-Th dating on monazite (Balogh and Dunkl 2005, Nagy et al. 2002). Fission track data (57.6-77.5 Ma on zircon and 62.6–40.9 Ma on apatite) indicate rapid tectonic exhumation after the Alpine metamorphism (Balogh and Dunkl 2005).

The orthogneisses consists of quartz, albite, K-feldspar, white mica, occasionally with minor biotite, garnet, clinozoisite, epidote, chlorite, ilmenite, rutile, monazite, apatite. The orthogneiss is associated with garnet-bearing chlorite-muscovite-paragonite-quartz schist, which may contain biotite and chloritoid as well. Mg-chlorite-muscovite-quartz schist with some kyanite and rarely phlogopite can be found along major shear zones crosscutting both the gneiss and the micaschist. Formation of this rock type is attributed to intense Mg-metasomatism caused by fluids migrating through the major shear zones (Kisházi and Ivancsics, 1987b; Demény et al., 1997, Török, 2001).

The orthogneiss contains relic, pre-Alpine magmatic minerals, such as zoned Fe-Mn garnet ($Alm_{34.2-72.8}Sps_{17.1-57.4}Prp_{3.5-9.5}Grs_{0-5.36}Adr_{0-1.98}$), muscovite (with 6.16-6.36 Si atoms p.f.u.), corroded annite-rich biotite with exsolved rutile needles and perthitic K-feldspar (Török, 1998). Muscovite was divided into high-Ti magmatic muscovite and low-Ti subsolidus muscovite applying the criteria of Miller et al. (1981) and Zen (1988). On the basis of relic, magmatic garnet composition and the presence of muscovite in the assemblage the pressure of garnet formation was estimated to be below 0.4 GPa at maximum temperature of 700°C (Török, 1998). The preserved magmatic relics and available chemical data (Lelkes-Felvári et al., 1984; and Kisházi & Ivancsics, 1989; Draganits, 1998, Török, 2001) show that the original rock was a peraluminous garnet-bearing two-mica leucogranite.

High-pressure Alpine metamorphism was inferred from a mineral assemblage containing Ca-Fe-Mn garnet ($Grs_{25.9-58.5}Alm_{12-55.8}Sps_{2.8-38.1}Adr_{0-13.9}Prp_{1.3-3.7}$), annitic, low-Ti biotite, phengite (6.58-7.03 Si atoms p.f.u.), K-feldspar, albite and clinozoisite. Under the high-pressure metamorphism the environment was relatively fluid-rich indicated by the abundant albitisation of the K-feldspar and aqueous fluid inclusions in the cores of the albite porphyroblasts (Török, 1996, 1998).

Petrography

We studied foliated gneiss and coarse grained pegmatite-like gneiss without any visible foliation, found in the operating quarry of Kő-hegy near the village of Kópháza (**Fig. 1.**). The foliated or sometimes sheared gneiss consists mainly of quartz, K-feldspar, albite, and muscovite, with subordinate amount of biotite and garnet. Zoisite, monazite, ilmenite and apatite were found as accessories. Quartz veins were found either parallel to the foliation or cross-cutting it. Two planes of schistosity can be revealed. The relic S_1 schistosity is shown by large (up to 400-500 μm) white mica flakes; it is cut by the younger S_2 schistosity, which is made up by smaller (usually between 80-160 μm) flakes of white mica and biotite. Most of the albite porphyroblasts contain numerous small white mica flakes and two-phase aqueous inclusions in the core, and have a thin inclusion-free rim. Albite with white mica inclusions tend to replace either muscovite or K-feldspar. K-feldspar can be divided into two generations. The first one is relatively big (up to 3-4 mm), twinned grains with perthitic exsolutions while the other one is smaller, without exsolution and associated with garnet, fine grained white mica and biotite. The latter often shows cross-hatched twinning pattern under the microscope. Garnet is usually xenoblastic with skeletal appearance, wrapped around by the S2 schistosity with inclusions of quartz, white mica and feldspar. BSE images of garnet do not exhibit a visible compositional zoning. A weak zoning is visible only on X-ray element maps with a relatively Mn-rich core and a very thin discontinuous Mn- and Fe-rich edge (**Fig. 2.**).

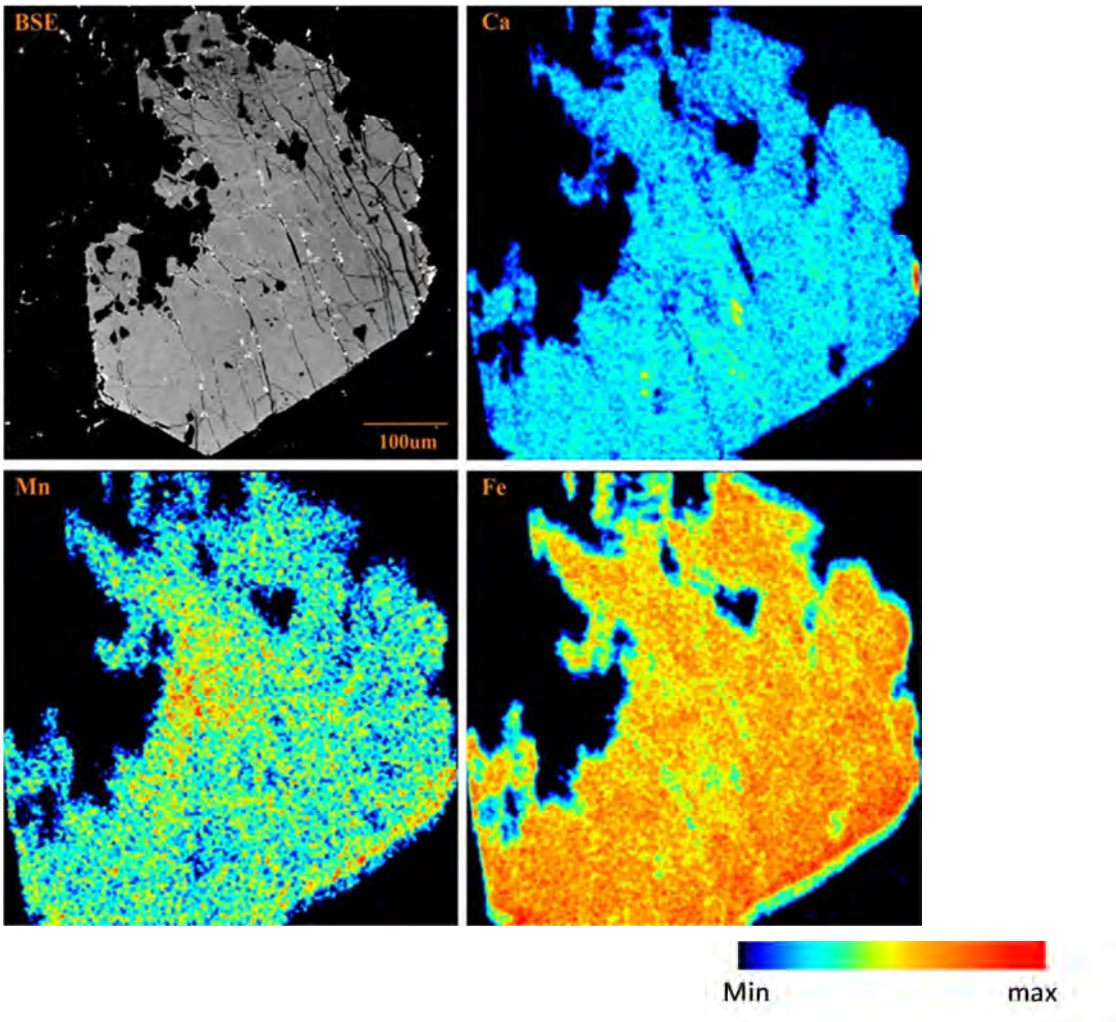

Fig. 2. BSE (upper left) and X-ray maps of a garnet from the foliated Kő-hegy gneiss. Warmer colors refer to higher concentrations on the X-ray maps; scan size: 1mm x 1mm.

The coarse grained pegmatite-like gneiss (further referred to as pegmatite) has similar mineralogy with some small differences. The foliation is much less expressed in the pegmatites than in the gneisses. This variety has no biotite, contains more quartz and less K-feldspar than the gneiss. The minerals in the pegmatite are highly deformed. The big feldspars and white micas (up to 0,8-1 cm) are floating in a quartz matrix of several subgrains along the ragged grain boundary of bigger grains with undulose extinction. Garnets are rare, subhedral, may contain inclusions of white mica and quartz and tend to be bigger than in the gneisses. BSE images of garnet show a homogeneous inner core followed by weak oscillatory zoning in the outer core and a sudden change in composition at the edge of the garnets. The BSE images also reveal darker precipitates along cracs in the garnet. X-ray maps show, that the zoning patterns, observed on the BSE images, namely the oscillatory zoning in the outer core and the the sudden discontinuous compositional change at the edge can mainly be attributed to the changes in the Ca content (**Fig. 3**). Several garnet grains both in the gneisses and the in pegmatite and were studied. The ones with the most complete zoning are presented in this paper.

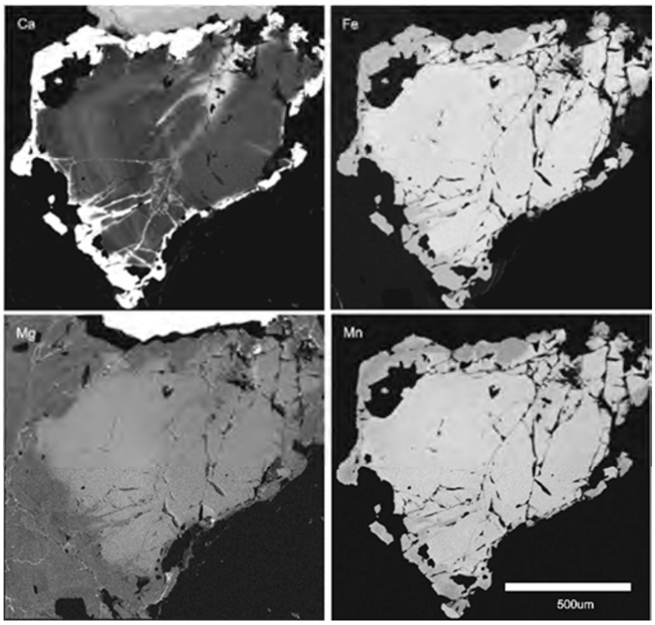

Figure 3. Grey scale X-ray images of garnet grain from pegmatitic nest. Darker grey refers to lower element content

Methods

Electron microprobe analyses and main element distributions were carried out at the Department of Lithospheric Research, Faculty of Geosciences, Geography and Astronomy at the University of Vienna on a Cameca SX Five electron probe microanalyser equipped with a field-emission electron gun and five wavelength dispersive spectrometers (WDS). Element distributions were carried out in stage scanning mode using WDS detectors, dwell times between 100-300 ms and 1.0 – 2.0 µm step size. An acceleration voltage of 15 kV and a beam current of 20 nA were applied for both element distributions and point analyses as well. The probe diameter was set to 5 and 2 µm in case of point analyses in plagioclase grains and micas, respectively. In all other cases the smallest possible beam diameter was used. Natural and synthetic mineral standards were used for calibration and ZAF correction was applied.

Mapping of main and trace elements was performed with micro-PIXE (particle induced X-ray emission spectroscopy) method at the scanning nuclear microprobe in the Institute for Nuclear Research, Hungarian Academy of Sciences in Debrecen (Rajta et al, 1996). Besides Fe, Mn, Mg and Ca trace elements such as Y, Dy, Ti, Zn, Cr and Zr were mapped. A proton beam of 2.4 MeV energy focused down to 2µm x 2µm with a current of 300-500 pA was used to irradiate the samples. Two Si(Li) X-ray detectors placed at 135o geometry to the incidence beam were used to collect the emitted characteristic X-rays. A detector with ultra-thin polymer window (UTW) was used to measure low- and medium-energy X-rays ($Z > 5$), and a Be windowed detector equipped with an additional kapton filter of 125 µm thickness was applied to detect the medium and high energy X-rays ($Z > 20$). The beam dose was measured by a beam chopper. This way all constituent elements could be measured at the same time, reducing both measurement time and sample damage. Signals from all detectors were recorded event by event in list mode by the Oxford type OMDAQ data acquisition system (Grime and Dawson, 1995). More detailed description of the measurement setup and data acquisition system can be found in Uzonyi et al (2001) and Kertész et al (2005, 2015).

In-situ trace element analyses and mapping were performed using LA-ICP-MS (New WaveUp 213 attached to Perkin Elmer Elan DRCII). Operating parameters of the ICP-MS are nebulizer gas flow of 0.96 l/min, auxillary gas flow of 1.2 l/min, plasma gas of 15,8 l/min, lens voltage of 7.25 V and RF power of 1450 kW. Dwell time was normally chosen 10 ms and 20 ms for HREEs. He-gas flow was optimized to 0.9 l/min. The laser worked at around 18 J/cm^2 (energy density) and at repetition rate of 5 Hz. The spot size was chosen 100, 55, 30, 15 (for mapping) and 8µm according to the inhomogeneities of the garnet grain. Acquisition time of background was circa 40 seconds of the transient signal while that of the sample signal was about 60 seconds. SRM NIST610 was applied as an external standard and BCR 2G was measured back as unknown material to control the quality of the analyses. Total oxide as internal standard was applied, whereas major elements (SiO_2, Al_2O_3, FeO, MnO, MgO, CaO, Na_2O) were scanned together with all the rare earth elements (REE), Y (hereafter REY together with REE), Zr, Nb, Hf, Ta, P, Ti, Cr, Co, Ni, Cu, Zn, Sr, Sc and V during laser ablation. They are only used for normalization (Liu et al 2008) and comparing the relative change to the electron microprobe data / locating precisely the ablation spot. Sm, Eu, HREY, Ti, P, Sc, V, Nb, Zn, Ni, Co and Zr were commonly above detection limit. Abundances of LREE in garnet were too low to be precisely analyzed therefore they are not considered here except Sm and Eu, when they are above detection limit.

After detection of small scale zoning in garnet by X-ray maps LA-ICP-MS analyses with a spot size of 100 µm, 55 µm, 30 µm and of 8 µm were arranged trying to follow the fine zoning pattern. Measurements with a spot size of 8 µm made only possible of detecting REY elements but it gave additional information on the complexity of the zoning.

Garnet chemistry

Garnets in the coarse grained pegmatite and in the gneiss have different major and trace element chemistry and will be described separately. Garnet of the pegmatite has two, compositionally distinct subsequent zones. Both zones are further refined by change in structural build-up (orientation of the crystal) and by X-ray maps of Ca, Ti, (Mn) as well as of Y.

Spessartine-rich magmatic core of garnet from pegmatitic nest.

The core is almandine-rich containing about 20% spessartine and minor grossular and pyrope ($Alm_{71\text{-}75}Sps_{20.8\text{-}22.6}Grs_{2.2\text{-}4.3}Prp_{2.3\text{-}2.8}$). It can be subdivided into a homogeneous inner core (Z1) and the outer core with subtile oscillatory zoning according to the Ca distribution map made by electron-microprobe (**Fig. 3**). The outer core showing oscillatory zoning may be subdivided into three parts: one with thicker oscillatory zoning (Z2), one with thin stripes (Z3) and the outer one seems to be homogeneous again (Z4). The grossular component in the "darker" zones of oscillation varies between 2.2% and 2.8% while the "light" zones are characterized by 3.3–4.3% grossular (**Fig.4**). Z2 is an overgrowth on the inner core (Z1) characterized by lower Ca-content and by slightly increased Mg. The subsequent Z3 zone showing the most enhanced oscillatory zoning is characterised by slightly higher grossular content, which is still less than that of the inner homogenous core. Z4 is depleted in Ca and Mn accompanied by a faint increase in Fe.

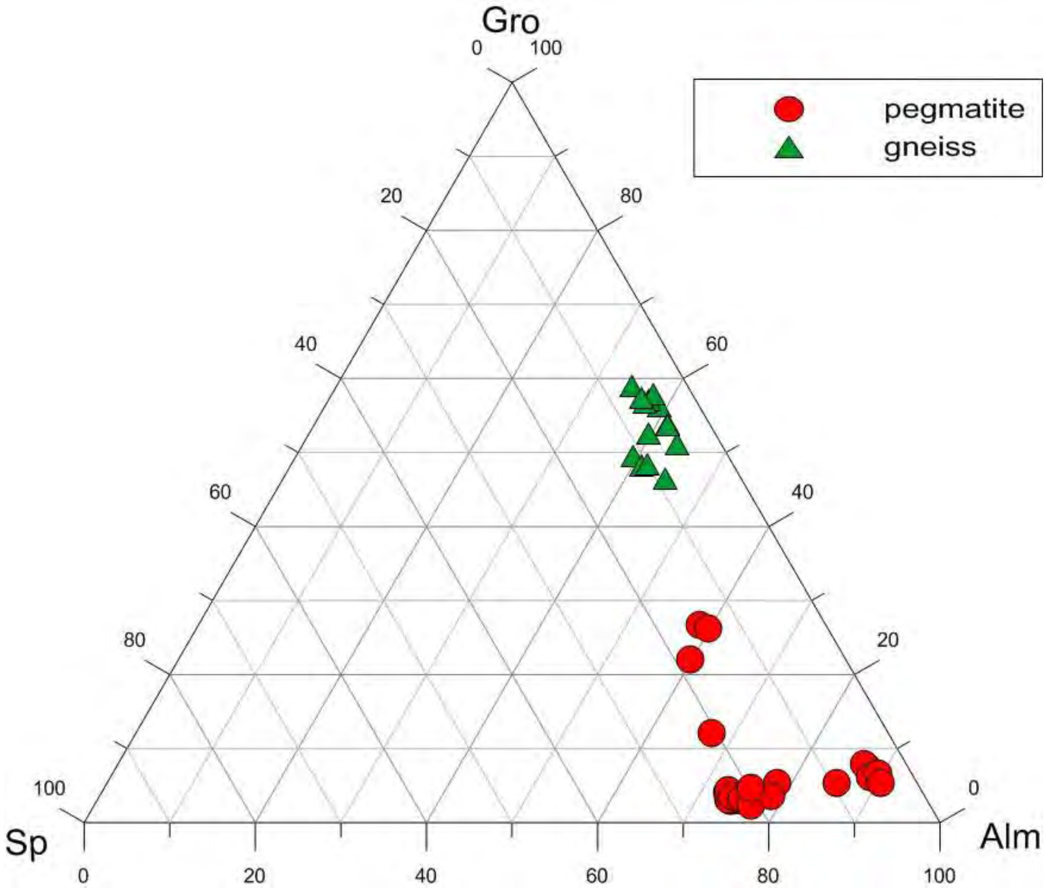

Figure 4. End-member compositions of garnets from coarse-grained pegmatitic nest and gneiss.

Fine trace element variations in the garnet were detected by core to rim profiles of LA-ICP-MS measurements with spot size of 30µ and 8µ (**Fig. 5**). According to these profiles the inner core of the pegmatitic garnet is characterized by enrichments of REY, Sc, Co, Zr, Ti, P and Na content (**Fig. 6**). The inner core does not display any zoning however a weak minimum in Ti and maximum in Ca, Sc and Co contents occur.

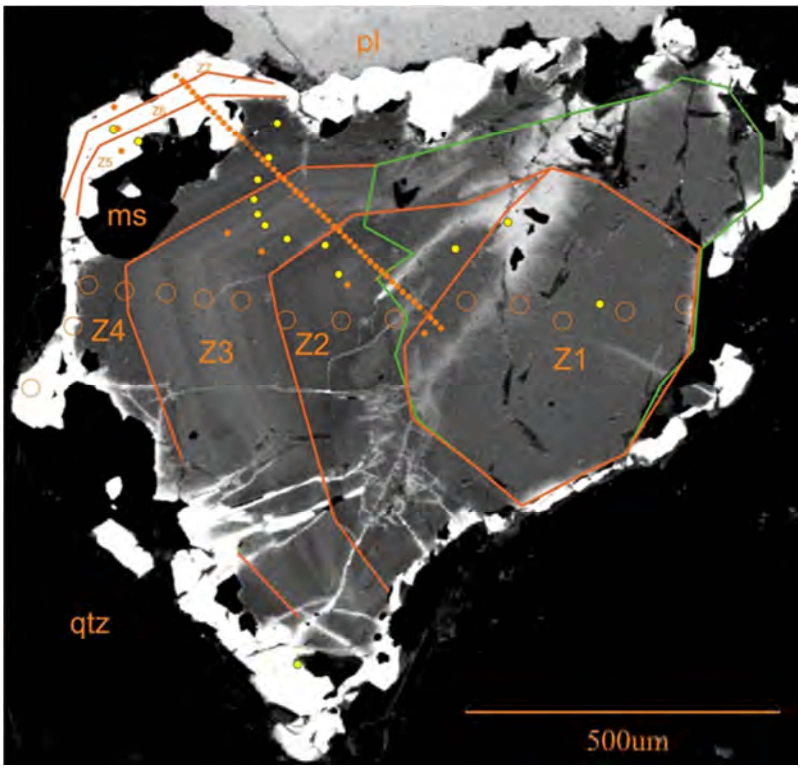

Fig 5 Ca-map of the same garnet grain shown on Fig. 3. with the zone boundaries and LA-ICP-MS profiles of the measurements with 30µm (unfilled circles) and 8µm (full dots) crater diameter. Green line shows amalgamated inner core. Yellow dots show the points of microprobe measurement.

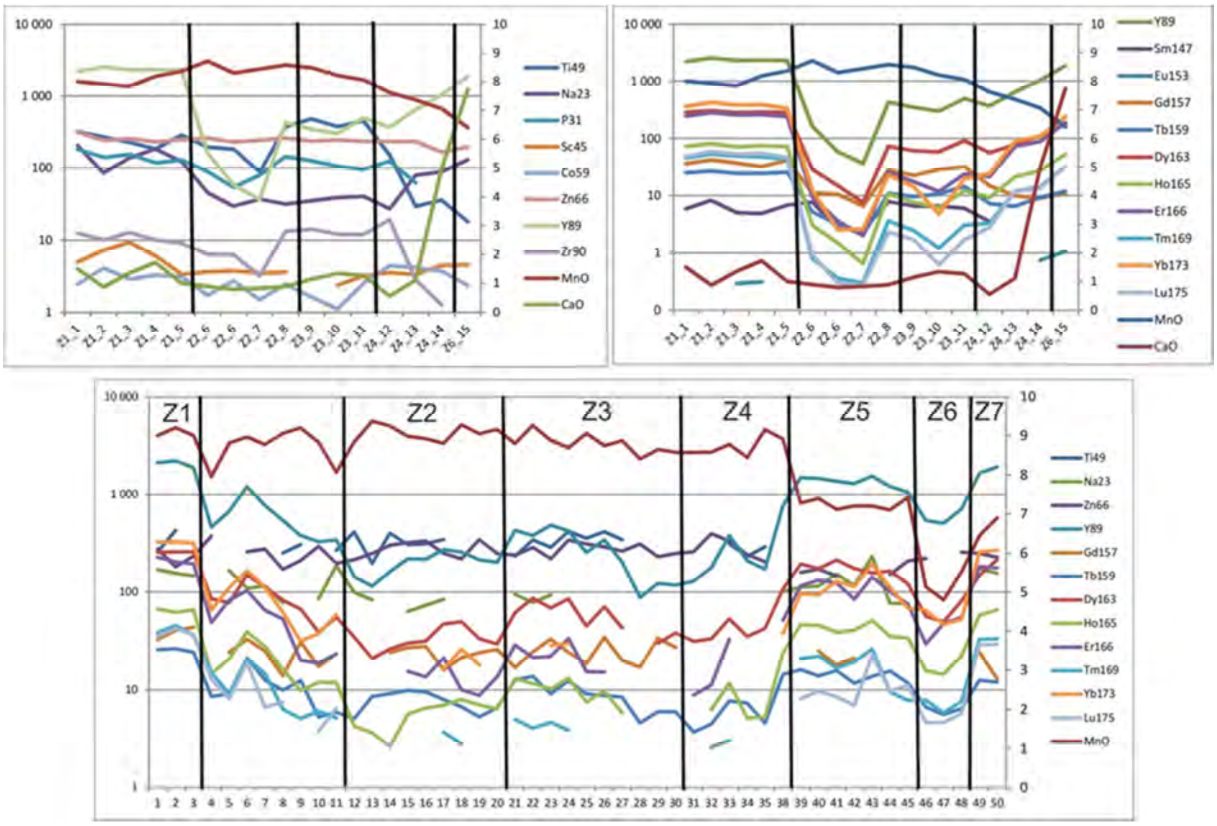

Figure 6 Trace element zoning along the traverses shown in Fig. 5 from measurements with 30 µm (upper profiles) and 8 µm crater diameter (lower profile).

Zone 2 (Z2) with faint oscillatory zoning exhibits the lowest REY, Sc, Co, Zr, Ti, P and Na contents. At the border of Z1 and Z2 chondrite normalized REY patterns are changed from HREY-enriched or flat pattern to depleted humpback one (**Fig. 7**). The most characteristic modification was found in HREE and Y distributions. The concentration of Y drops from 2548 to 36 ppm along with a decrease in Yb from 424 to 3 ppm however Gd varies only from 42 to 7 ppm and the Sm content is modified even less from 8 to 3 ppm (**Fig. 6 and 7**). The difference in concentrations of middle rare earth elements (Sm, Gd, Tb, Dy) is relatively smaller than the change in HREY therefore a relative enrichment of either Tb and/or Dy produces the humpback pattern. The humpback REY distributions belong to the zones of Z2, Z3 and Z4.

The outer part with more expressed oscillatory zoning (Z3) has somewhat higher more REY and P-contents, but still lower than in the homogeneous inner core (Z1) in contradiction to the Zr and Ti contents, which are enriched in Z3 the most, even more than in the core (**Fig. 6**). The lower Ca-, and Mn contents are coupled with lower Ti, Zr, (REY) and enrichment in Co in zone Z4.

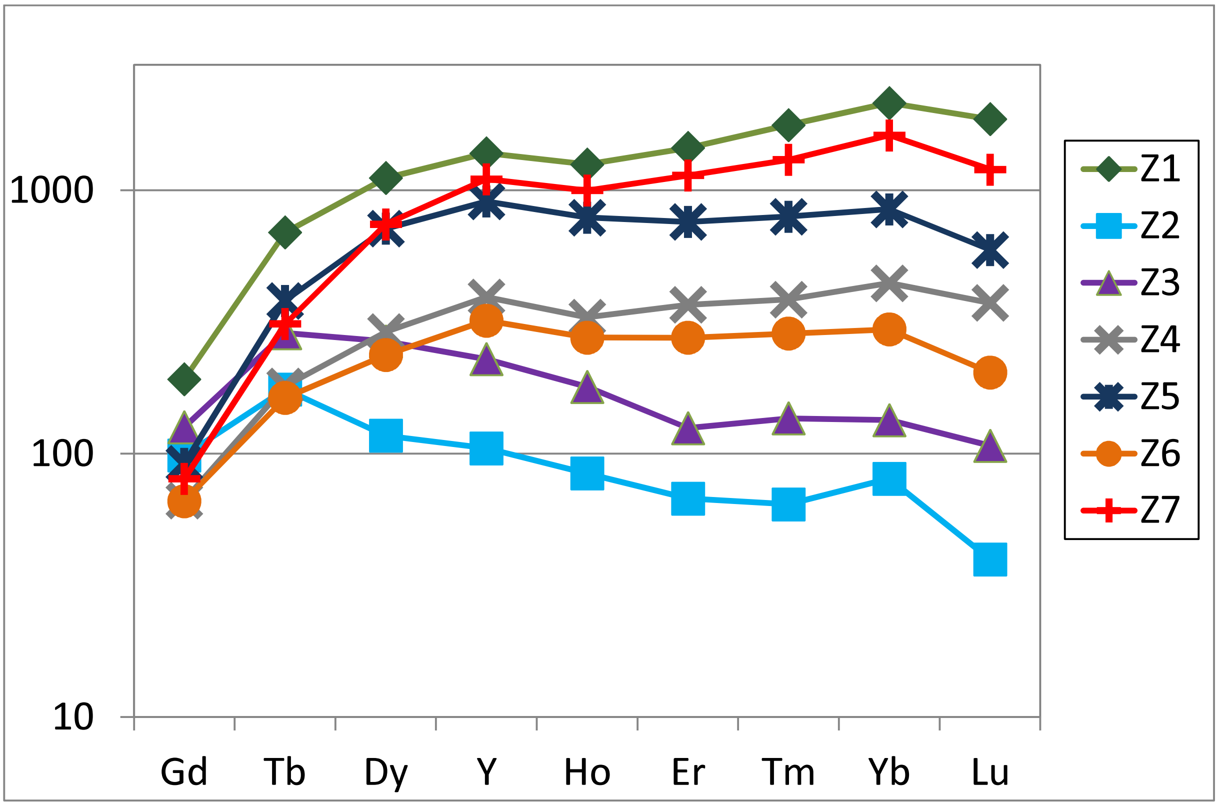

Fig 7 Chondrite normalized average REY patterns of the 7 zones of the pegmatitic garnet shown on Fig. 3. Normalisation is according to McDonough and Sun (1995)

Boundaries between zones might slightly be modified in space in the case of different elements due to LA-ICP-MS profile analyzed from ablated material of a 8 µm size crater however there are also divergences at the border in the case of 30 µm size spots. At the border of Z1/Z2 the 8 µm profile exhibits a transition zone due to Ca enrichment through cracks. Outlines of structural and Ca X-ray map boundaries differs from boundaries signed by REY distributions. A good example is spot Z2_8, shown on **Fig 6**, which belongs to Z2 in the structural sense and based on its low Ca content while the trace element distribution characters (enriched in Ti, P, Zr and REY) are rather resemble to the Z3. The boundary of Z3/Z4 is not well defined either. The depletion in Ca, Mn and Ti are coupled with similar or increased Ho-Er-Tm-Yb-Lu as well as Y while lighter REE-s (Sm-Gd-Tb-Dy) show decrease instead of enrichment. The increase of Co content is observed (at ca. 30 µm) closer to the zone boundary, than the decrease in Zr. It is interesting to note that some of the trace elements (like Zn) seem to show almost homogeneous distribution throughout the highly inhomogeneous garnet.

Grossular-rich metamorphic rim of garnet from pegmatite

These threee zones (Z5-Z7) were revealed by the higher magnification element maps (**Fig. 8**) and were only possible to obtain trace element data using the 8 µm crater diameter measurements of the LA-ICP-MS (**Figs 6 and 7**).

An inhomogeneous and discontinuous grossular-rich rim grew on the resorbed surface of the Z4 garnet. The inhomogeneity of the rim is revealed by the wide range and fluctuation in REY composition (**Fig. 6 and 7**). The rim exhibits elevated grossular and lower almandine, spessartine and pyrope ($Alm_{57.8\text{-}59}Grs_{21.7\text{-}26.4}Sps_{13.8\text{-}18}Prp_{1.3\text{-}1.4}$, **Fig.4**) contents relative to the core (Z1-Z4). The X-ray map of Ca exhibits that grossular-rich material of the rim appears along cracks throughout the garnet core. The most penetrative cracks are parallel to the schistosity. The best-developed parts of the rim on the shortening side display three zones (**Fig. 8**). Because of the very thin zones trace element concentrations in these three zones were measurable only with 8µm spot size. Trace element analyses are almost restricted to REY in the case of 8 µm spot size. Only larger crater size (30 µm) ensures reliable data on other trace elements like Na, P, Sc, Ti, V, Co, Zn and Zr. A sudden increase of the grossular content coupled with increasing REY content is the most striking feature of Zone 5 (Z5). Further grossular enrichment is detected in the intermediate zone (Z6), which is compensated by the decrease of spessartine and almandine components accompanied by depletion in Ti and REY. Zone 7 (Z7) reveals an enrichment in REY again with Mn and decrease of Ca. Z5 and Z7 is enriched in Y as much as 1539 and 1913 ppm, respectively, in contrast to the maximum concentration of Y of 708 ppm in Z6 (**Fig. 6**). The last zone (Z7) is the most enriched in REY. Some of the limbs developed parallel to the schistosity representing the Z7 have the highest REY enrichment. They might have even more REY content than in the core. The highest concentration of Y (3221 ppm) was measured in a limb growing in a pressure shadow and belonging to Z7 in another garnet grain. All zones of the rim are resorbed (**Fig. 8**). Na seems to be enriched in zone 5, while in other zones Na is below the detection limit. All the trace elements, Ti, P, Sc, Co, Zn and Zr seem to decrease or drop below the DL at the rim (Z5-Z7) while the REY are enriched in all rim zones but to different extents.

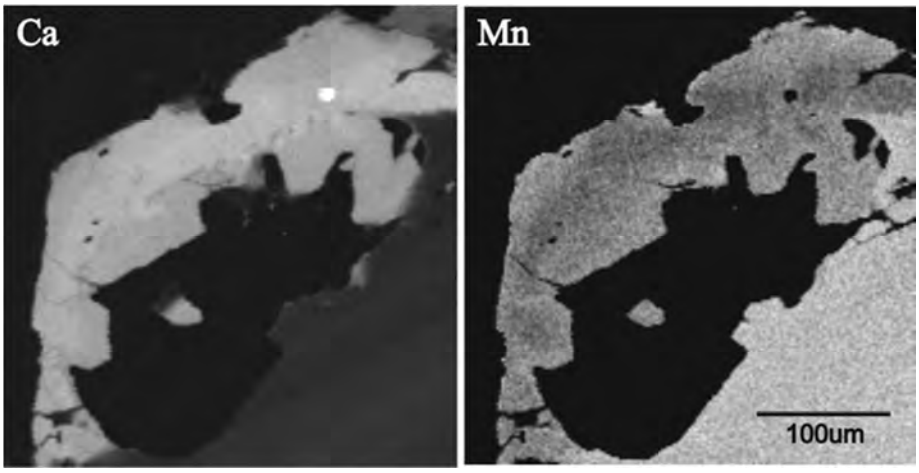

Figure 8. Grey scale X-ray images of the metamorphic rim of the pegmatitic garnet. Darker grey refers to lower element content. The bright spot on the Ca map is apatite, the dark patch in the middle of both maps is muscovite.

Garnet from gneiss

Garnet in gneiss displays different chemical charactistics than the garnets from the pegmatitic nests. They are mainly grossular-almandine solid solutions with some spassartine and minor pyrope ($Grs_{46.1\text{-}58.6}Alm_{34.4\text{-}44.4}Sps_{4.6\text{-}11}Prp_{0.5\text{-}0.9}$). This composition differs substantially from that of the garnets in the pegmatite with much higher grossular and lower almandine and spessartine content. Usually no characteristic zoning is observed, however in a subhedral grain (**Fig. 2**) slightly spessartine-richer core and a discontinuous spessartine increase at the very edge of the garnet are detected. Changes in spessartine are compensated mainly by grossular, subordinately by almandine.

Trace element distributions (**Fig. 9**) also display only weak variation. Subhedral and elongated garnet grains from gneiss sometimes reveal distinct trace element contents. Sc, Zr and Co distributions look similar in both types while distributions of V, Ti, Zn and possibly P change in a different way. The subhedral grain is composed by more P and Zn but less V and Ti. Subhedral grain contains 184–765 ppm Ti while the elongated garnet contains 710–2725 ppm. Garnets in the pegmatite have typically lower Ti content in most cases (28–598 ppm in the core and 18–163 ppm in the rim) V is below detection limit in garnet from pegmatite however garnet in gneiss contains 14–37 ppm of V in the case of subhedral grain and 23–64 ppm in elongated garnet. Although P is not a reliable element measured by ICP-MS due to spectral interferences, the subhedral grain contains significantly more P (94–3131 ppm) than the elongated garnet grain where P is below detection limit except for one spot (212 ppm) at the very edge of the garnet grown in a pressure shadow. P content in the garnet from pegmatite usually covers the lower end of the interval measured in the garnets (32-713 ppm) from gneiss. The lower values are characteristic to the Ca-rich rim of the pegmatitic garnet. Zn distribution is very homogeneous in garnet from pegmatite but here is also a shift between Zn content of the two garnet grains from gneiss: Subhedral grain has slightly more Zn content (25–81 ppm) than the elongated one (15–31 ppm). Concentration of Zn is definitely higher in magmatic garnet of the pegmatite nest (131–396 ppm) showing slight decrease at the metamorphic rim (129–294 ppm) and further decrease (15–81 ppm) in garnet grains of gneiss. The amount of Sc can reach 18–75 ppm in garnet from gneiss but its content is never more than 17 ppm (2–17 ppm) in pegmatitic garnet. The higher amounts were detected in the core of the pegmatitic garnet. Vanadium concentrations and distribution in garnet is very similar to Sc (**Fig. 9**).

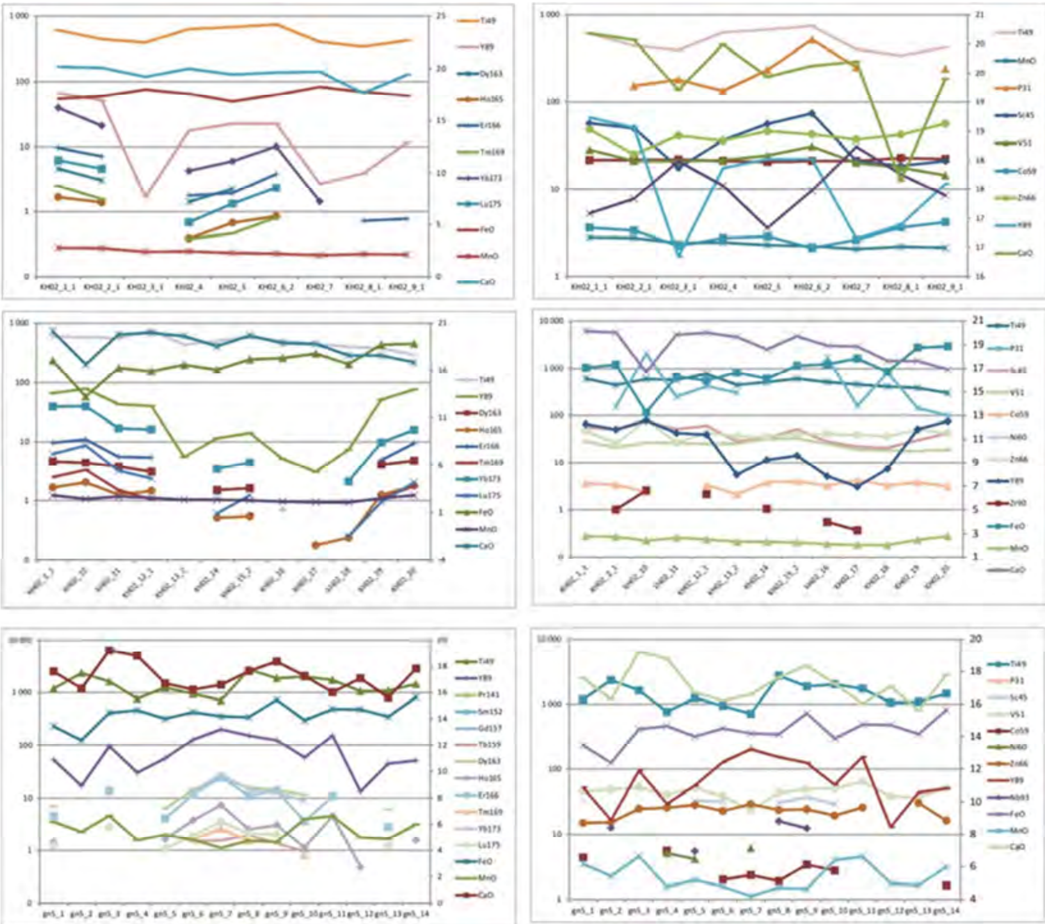

Figure 9. Trace element zoning of garnets from gneiss

Depletion in REY characterizes garnets in the gneiss as compared to the majority of the pegmatitic garnet zones. Sum of REE is far less here (≤90 and ≤130 ppm respectively in elongated and subhedral garnet) than in the majority of garnet zones in pegmatite (14–1458 ppm). Limbs of garnet grown in pressure shadow similarly to the pegmatitic garnet shows a characteristic increase in sum REE (from 13 to 90 ppm) towards the rim (**Fig. 10**).

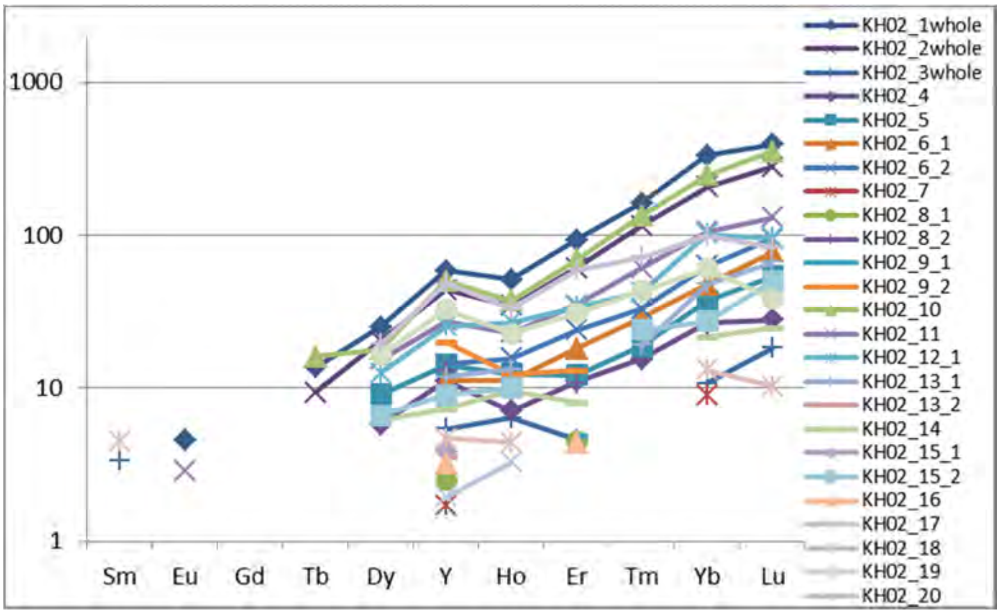

Fig 10 Chondrite normalized REY patterns of the gneissic garnet.

The garnets in gneisses are strongly depleted in REY however some limbs along schistosity reveal some enrichments as the Ca-rich rim in pegmatitic garnet. REY patterns are also distinct: flat or HREY enriched patterns change to humpback patterns in pegmatite while garnets from gneiss have an enriched HREY pattern without any humpback character (**Fig. 10**).

Discussion

Garnets from the Kő-hegy and the other gneisses of the Sopron Mts. were earlier studied and characterized by Török (1996, 1998) using their main element chemistry. Török (1998) divided the analyzed garnets into three groups. The core of the pegmatitic garnet (zones 1-4) in this study fits in the chemical composition of Fe-Mn-rich group, which was found to be of magmatic origin on the basis of its textural position and composition. The conditions of formation were determined to be 0.25-0.4 GPa and 630-680°C earlier by Török (1998) on the basis of CaO content of garnets (Green, 1977), muscovite+quartz stability (Chatterjee and Johannes, 1974) and muscovite granite solidus (Huang and Wyllie, 1973).

The grossular-rich garnets, found throughout the studied gneisses in the Sopron Mts., were considered of metamorphic origin together with the Ca-rich outer zone of the pegmatitic garnet, which was further divided into three distinct zone in this study (Z5-7). During the present study we could detect a more detailed and complex garnet growth and zoning in terms of major and trace elements. The 7 different zones described above may represent different growth events in the magmatic and metamorphic history of the gneiss. Signs of multiple resorptions and the observed different styles of zoning as well as the documented changes in main and trace element chemistry of the garnets indicate a complex growth-dissolution history.

Magmatic garnet growth

According to the X-ray maps, the homogeneous, Ti, Y and REE-rich inner core (Z1) can be regarded as the first product. The Ca-map shows an idiomorphic garnet core, but the Y distribution map made by micro PIXE shows that the core extends to larger areas. Thus the idiomorphic part and the related areas may represent more than one garnet core amalgamated together during the growth of the first garnets from the peraluminious granitic melt. Further growth of the garnet was either assimetric or the other parts later resorbed and disappeared. Now we can observe the Ca poor, Ti, Y and REE-rich inner core (Z1) with the subsequent further generations overgrown on one side and with the Ca-rich rim directly overgrown on resorbed inner core on the remaining sides (**Fig. 5**). The homogeneous core does not display big variations in REY or other major or trace elements distributions, except for Sc and Na. Sc shows a decrease within the Z1, which shows that Sc was the first element to be exhausted from the melt in the close neighbourhood of garnet nuclei. Na oscillates simultaneously with Ca, which shows that availability of these two elements has changed during the growth of the core. These changes may be in correlation with plagioclase crystallisation along with the garnet. The little variations in main and trace elements show that crystallization of Z1 can be processed from a homogeneous melt at stable conditions.

According to Pyle and Spear (1999), the relatively high concentration of REY in garnet from anatectic samples is related to dissolution of phosphates in vapor absent, peraluminous melt, with partitioning of highly compatible REYs into garnet grown during anatexis. Mechanism of developing of garnet core (Z1) in the pegmatite might be explained by formation from the peraluminious melt where the higher REY-content is provided by the dissolved phosphates. Textural analysis reveals that accessories (phosphates as well) are rare both in gneiss and in pegmatitic nests as Pyle and Spear (1999) described the lack of phosphates in the environment of garnet grown in equilibrium with melt. According to our observations the magmatic zones (Z1-Z4) do not contain any apatite or other phosphates. However in the metamorphic rim and the garnets in gneisses may contain apatite inclusions, but the presence of xenotime or any other Y-bearing accessory phase is not observed either because of xenotime was never formed or it had been completely consumed by garnet.

In spite of the several lines of evidence supporting the crystallization of Z1 from a peraluminious melt, the question of other origin than magmatic may arise, as the gneiss contains micaschist enclaves in several outcrops, including the Kő-hegy quarry. We have to discuss the possibility that the REY-rich inner core (Z1) might represent a metamorphic relict. According to several authors the REY content of metamorphic garnets decreases with increasing temperature and pressure (e.g. Hickmott et al, 1987; Otamendi et al, 2002; Likhanov & Reverdatto, 2016), thus metamorphic garnets usually contain relatively high amounts of REY in their core, which decreases towards the edge with increasing metamorphic grade. This contradicts to our observations of relatively high and homogeneous REY content of the Z1 inner core of our garnets. The other contradiction is the main element chemistry, namely the dominance of Fe and Mn with relatively low Ca content, which points rather to the magmatic origin of the Z1.

A sudden and drastic decrease of Y, REE and most of the measured trace elements (except for Zn) and the change in the distribution pattern of HREY from flat to humpback (**Fig. 7.**) takes place at the boundary between the inner core and Z2 zone, attributed to a new garnet generation (Z2). Although we do not see any signs of resorption, a break in the garnet growth can be inferred on the basis of the sudden change. The observed features also imply changes in both the chemical environment and the crystallization conditions of the garnet from equilibrium one to disequilibrium one. The melt was exhausted in Lu, Tm, Yb, Er, Ho, Y, Dy, Tb, Gd and Sm in decreasing order, which is almost identical with the order of the decreasing values of $K_{dgrt/melt}$. The rate of depletion is between 111 and 173 in the case of Lu, Tm, Yb, Er and Ho, but less (64–12) in the case of Y, Dy and Tb and still multiple times in the case of Gd and Sm. Thus a cause of the serious depletion of HREE in Z2 might be the Rayleigh-fractionation (Hollister et al, Pyle and Spear, 1999, Otamendi et al. 2002).

The change in the style of distribution of REY from Z1 (increasing trend in the REE diagram in Z1 and humpback distribution in Z2-4, see **Fig. 7**) to Z4 is also related with the difference in incompatibility of HREE and MREE. The distribution of the HREE shows a typical growth zoning with high amounts of HREE in the core (Z1) and a decreased amount of HREE in the Z2. The previously grown Z1 incorporated the more compatible HREE in a higher rate leaving behind a HREE depleted melt/fluid with higher proportion of MREE. During the growth of the further zones of pegmatitic origin (Z2, Z3 and Z4) the proportion of available MREE constantly was higher in the remaining melt and fluid than during the growth of Z1 causing the humpback nature of distribution of the REY, although the quantity of the REY has grown from Z2 to Z4. This feature may be explained by the depletion of Y and HREE-s from the whole magma by growing Z1 garnets, but some more distant parts of the remaining fluid-rich magma may have retained higher concentration of REEs than that crystallizing the Z2. When the Z3 and Z4 zones were growing, these parts may have supplied the growing amount of REYs and other trace elements.

However the above cited works all show that during a fractionation the change is gradual and not as sharp as in our case. According to Müller et al (2012) the sharp drop in the HREY might result from an abrupt change of the environment of the garnet growth, a change from "normal" peraluminous melt composition to a Na-rich aqueous silica-bearing fluid-rich melt, which is depleted in HREE. Thus this sudden change in trace element content would mean the end of the silicate melt dominated magmatic crystallisation and the beginning of garnet growth in fluid dominated pegmatitic environment. However we do not consider this as viable route in this case, because Na content in Z2 decreases, which shows a depletion caused by albite crystallisation and does not support the idea of a Na-rich fluid.

The explanation of the sudden REY drop between the Z1 and Z2 may be related to the formation of oscillatory zoning in Z2 and Z3. Oscillatory zoning is caused either by repeated changes in the garnet-fluid (±melt) equilibrium related to changes of temperature, pressure and/or fluid/melt composition or by an interplay between garnet growth rate and diffusion in the granitic melt (Harloff, 1927). In this sense the garnet growth rate and/or the diffusion rate has also changed between the Z1 and Z2. While the Z1 has grown more slowly in a relatively steady environment, Z2 and Z3 were growing more rapidly in a slowly cooling environment with lower diffusion rate. This change in growth rate of the magmatic garnet was already discussed by Török (1998) on the basis of main element zoning.

The next zone (Z3), which has a more pronounced oscillatory zoning of grossular and some more REY, Ti, P, Ca and REE content, develops continuously from the Z2. The absolute concentrations of most of the trace elements are larger than in Z2 but in the case of Ti and Zr concentrations exceed that in Z1 and P also increases, which supposes that REY, Zr, Ti and P bearing minerals may have dissolved and contributed to additional material supply of the garnet. The HREEs with the highest atomic number (Er, Tm, Yb, Lu) show some temporal depletion within the Z3. HREE with lower atomic number and MREE show just a moderate or no depletion (**Fig 6**), which again shows the fractionation of the HREE. The depletion is followed by a rise again, which continues in the Z4 as well.

The slightly enriched oscillatory zoned Z3 is followed by a zone (Z4) without visible zoning (**Fig. 3. and 5**). The detectable final stage of the magmatic garnet crystallisation is marked by continuous development of a Ti, Zr, P and Ca poor zone (Z4), with Y and HREE enrichment on the edge. The initial Ca depletion then turns to Ca enrichment towards the Ca-rich metamorphic zones (Z5-7). Zr, Ti and P, which reached the maximum concentration in the previous zone (Z3) decreases rapidly (**Fig. 6**). This shows that these elements, which were reintroduced in the system during the growth of the Z3 are exhausted from the melt rapidly, probably by crystallization of zircon and Ti-oxides or simply by exhaustion in the vicinity of the garnet. However REY are not exhausted, but they have continuous and growing supplies. When Zr, Ti and P begin to decrease, Na content starts to rise together with the REY. This would imply that the source of the REY is not identical with that of the Z3, but they are introduced into the system selectively, most probably by fluids during the growth of the Z4. We cannot see the end of the magmatic/pegmatitic garnet crystallisation, because the outermost magmatic/pegmatitic rim (Z4) is resorbed with an unknown rate and the original magmatic edge of the garnet can not be observed. Mn-depletion can be caused by the exhaustion of Mn from late magmatic-pegmatitic melt/fluid, which leads to the end of garnet formation. Muscovite inclusions suggest that the melt/fluid is still oversaturated by Al, but not by Mn and Fe, and aqueous phase was also present at the end of magmatic garnet crystallization. The Y and REE enrichment on the edge of the Z4 may be attributed to resorption caused preferential retention of highly compatible trace elements at the garnet rim (Hermann and Rubatto, 2003, Storkey et al., 2005).

Formation of metamorphic garnet in pegmatite

The Ca-rich metamorphic rim is very thin in comparison with the magmatic/pegmatitic garnet and comprises of three distinct and discontinouos zones (Z5-7), each predated by resorption, which shows that garnet formation was very limited in space and time and interrupted several times by dissolution during Alpine metamorphism. The Z5 garnet zone crystallised on the resorbed and fractured remnants of the magmatic garnet as it is demonstrated by the high Ca overgrowth and fracture-fillings on the Ca maps of the garnet **(Fig. 3 and 5)**. The high Y and REE content of the new, metamorphic garnet (Z5, **Figs 6 and 7**) may have come from the partial resorption of the magmatic garnet. Resorption of earlier garnet may have triggered formation of a HREE and Y-rich phase, which may have decomposed during the initial stages of metamorphism and gave rise to formation of garnet with high HREE and Y. This is shown by the HREY pattern, which begins a rise at the very edge of the Z4. The high REY and Mn shows the growth of garnet during prograde metamorphism. Another break in the garnet formation with dissolution shows the end of the Z5 and beginning of Z6. The lowest Mn and the highest Ca content shows that this zone might have formed close to the pressure and temperature peak, under high pressure (1,4 GPa) and at moderate temperature (500-550°C) in the presence of dilute, NaCl-dominated aqueous fluids (Török 1998). The lower HREE and Y content of this zone is in good agreement with the observations (e.g. Otamendi et al 2002) that the metamorphic garnets usually accumulate the majority of the HREE and Y in their cores (now Z5) during the initial stages of the garnet growth.

Strong increase of HREE and Y observed in the Z7, which applies especially to garnet limbs growing in pressure shadows. A similar fenomenon was reported by Fornelli et al (2014) from granulitic rocks of Calabria. They attributed this feature to influence of hydrous melts or aqueous fluids. In our case the peak temperature of the alpine HP metamorphism did not exceed 600°C (Török, 1998, 2001, 2003), thus melting can be excluded. As the increase in the HREE and Y is coupled with an increase in Mn, we think that this thin rim may be related with aqueous fluid influx during retrogression. A REE and Th-bearing phosphate mineralisation linked with the retrograde stage of the alpine metamorphism was described by Fazekas (1975), Török, (2001), Freiler et al, (2015), Kertész et al, (2015) from the metamorphic rocks of the Sopron Mountains from several localities. We consider the HREE and Y enrichment in the Z7 as the influence of these retrograde metamorphism related fluids in the pegmatites of the Kő-hegy gneiss.

Garnet growth in gneiss

Garnets in the gneiss show several differences regarding their trace element content in comparison with the garnet found in pegmatites. We did not find any relics of magmatic garnet in the gneiss. The most striking difference is the very high Ca content of the garnets in gneisses even in comparison with the Ca-rich garnet rim of the pegmatites. These high Ca garnets were interpreted as metamorphic ones by Török (1996, 1998).

Metamorphic garnet from gneiss contains more P, Sc, V, Ti and less Zn, REY than metamorphic garnet rim in the pegmatite. The very low REY content of the gneissic garnets may be due to the very low REY content of the gneiss itself, which is shown by very low abundance of monazite, xenotime in the rock. The high Ca content of the garnets show that they were in large parts formed from the anorthite component of the plagioclase and magmatic biotite. This would imply a reaction environment with low concentrations of REY. The higher Ti, Sc and V content in comparison with pegmatitic garnets refers to the higher abundance of biotite and other Ti-bearing phases, which may have taken part in the garnet forming reaction. However Zn, which is mainly incorporated in biotite and is expected to be incorporated into garnet during bioite decomposition shows depletion in gneissic garnets in comparison with metamorphic garnets in the pegmatite. In the case of gneisses phengite, which also readily incorporates Zn, forms also at the expense of biotite and K-feldspar during high-pressure Alpine metamorphism (Török, 1998). Regarding this situation, the Zn content released from biotite breakdown was dissipated between Alpine and phengite. In the case of the pegmatites lack of biotite and phengite left just one choice for the Zn, to incorporate into the garnet.

The distribution of REY follows the usually described trends, with higher concentrations of REY in the core and decreasing towards the rim. However we have an enrichment at the edge, similarly to the ones in the pegmatitic garnet, which indicates that the fluid influx discussed above reached the gneiss as well.

Conclusions

Garnets of magmatic and metamorphic origin were analyzed by EMPA, micro-PIXE and LA-ICP-MS from pegmatitic and foliated gneiss found in Kő-hegy, near Sopron. Experimental application of 30 μm and 8 μm crater diameters during LA-ICP-MS measurements revealed fine fluctuations in trace element zoning. 4 magmatic and 3 metamorphic events during garnet growth were distinguished from well-preserved Variscan pegmatitic garnet. Zones of the pegmatitic garnet were assigned mainly on the basis of textural features shown on Ca map, main element chemistry, and REE concentrations. However concentrations of some trace elements (e.g. Ti, Zr, P, Zn) are not bound to these zones.

Formation of garnet started with a slowly growing homogeneous, high REY core in a peraluminious granitic melt. The subsequent oscillatory Ca zoning of low REY Z2 and Z3 shows fractionation of HREE in the core as well as the changing growth and diffusion rate in the growing garnet.

REY, Zr, Ti and P bearing minerals may have re-dissolved or remelted during crystallization of the Z3 garnet, shown by elevated amounts of these elements. Z4 garnet is the final magmatic zone, where another REY peak with Na shows the influence of a late magmatic fluid influx.

Asymmetric resorption of the magmatic garnet during subsolidus or early metamorphic conditions was followed by prograde metamorphic crystallisation of a Ca-rich garnet. Reaction products formed from partial resorption of the magmatic garnet may have served to relatively high REY content of the new metamorphic garnet, which shows a typical prograde decrease of HREE and Y during growth until the peak metamorphic conditions. The high REY content of the incomplete retrograde rim of the garnet records a fluid, rich in REY.

Metamorphic, high Ca garnets in the gneiss have low REY and Zn, but higher P, Sc, V, Ti content than the metamorphic garnet in the pegmatite. These differences are attributed to the different availability of elements in the pegmatite and the gneiss.

Aknowledgements

This research was supported by Geological and Geophysical Institute of Hungary (project 3.8), the Hungarian National Research, Development and Innovation Office (grant nr. OTKA PD 104692) and the Bolyai János Research Scholarship donated to JD.

References

Ackerson, M.R. (2015): AGU Fall Meeting, San Francisco.

Balogh, K., Dunkl, I. 2005. Argon and fission track dating of Alpine metamorphism and basement exhumation in the Sopron Mts. (Eastern Alps, Hungary): thermochronology or mineral growth? Mineralogy and Petrology 83, 191-218.

Carlson, W.D. (2002): Am. Mineral., 87, 185–204.

Chatterjee, N.D. & Johannes, W., (1974): Thermal stability and standard thermodynamic properties of synthetic 2M muscovite, KAl2[AlSi3O10(OH)2]. Contrib. Miner. Petrol. 48: 89-114.

Chernoff and Carlson (1997a, 1997b, 1999

Demény, A., Sharp Z.D., Pfeifer H-R., 1997. Mg metasomatism and formation conditions of Mg-chlorite-muscovite-quartzphyllites (leucophyllites) of the Eastern Alps (W. Hungary) and their relations to Alpine whiteschists. Contributions to Mineralogy and Petrology 128, 247-260.

Draganits, E., 1998. Two crystalline series of the Sopron Hills (Burgenland) and their correlation to the lower Austroalpine in Eastern Austria. Jahrbuch der Geologischen Bundesanstalt, 141, 113-146 (in German with English abstract).

Fazekas, V., Kósa, L. Selmeczi, B., 1975. Rare-earth element mineralisation in the crystalline schists of the Sopron Mountains. Földtani Közlöny, 105, 297-308 (in Hungarian with English abstract).

Fornelli, A., Langone, A., Micheletti, F., Pascazio, A., Piccarreta G. (2014) The role of trace element partitioning between garnet, zircon and orthopyroxene on the interpretation of zircon U-Pb ages: an example from high grade basement in Calabria (Southern Italy). International Journal of Earth Sciences, Volume 103/2, 487-507.

Freiler, Á., Horváth, Á., Török, K. (2015) ^{226}Ra activity distribution of rocks in the Sopron Mts. (West Hungary). J. Radioanal. Nucl. Chem. 306, 243-247.

Grime, GW., Dawson, M. (1995): Recent developments in data acquisition and processing on the Oxford scanning proton microprobe, Nucl. Inst. and Meth. B 104 107

Green, T.H. (1977): Garnet in silicic liquids and its possible use as a P-T indicator. Contrib. Miner. Petrol. 65: 59-67.

Harloff, C. (1927) Zonal structures in plagioclases. Leidsche Geol. Mededeel. 2, 99- 114.

Hermann and Rubatto, 2003:

Hickmott D.D., Shimizu, N., Spear, F.S., Selverstone, J. (1987) Trace-element zoning in a metamorphic garnet. Geology, 15, 573-576.

Hickmott & Shimizu 1990;

Hickmott & Spear 1992;

Hollister et al

Huang W.L. & Wyllie, P.J. (1973): .Melting relations of muscovite-granite to 35 kbar as a model for fusion of metamorphosed subducted oceanic sediments. Contrib. Miner. Petrol. 42: 1-14.

Keane, S.D., Essene, E.J., Manning, C.E. (1997): Seventh Annual V. M. Goldschmidt Conference, Tucson, Arizona.
Kertész, Zs., Furu, E., Angyal, A., Freiler, Á., Török, K., Horváth, Á. (2015) Characterization of uranium and thorium containing minerals by nuclear microscopy. J. Radioanal. Nucl. Chem. 306, 283-288.
Kertész Zs., Szikszai Z., Uzonyi I., Simon A., Kiss Á. Z. (2005): Development of a bio-PIXE setup at the Debrecen scanning proton microprobe. Nucl. Instr. and Meth. B 231, 106-111.
Kisházi, P., Ivancsics J., 1985. Genetic petrology of the Sopron Crystalline schist sequence. Acta Geologica Hungarica 28, 191-213.
Kisházi, P. & Ivancsics, J. (1987a): Petrogenesis of the Sopron Micaschist Formation. Földtani Közlöny, **117:** 203-221. (in Hungarian with English abstract).
Kisházi, P. & Ivancsics, J. (1987b): Contribution to the problematics of the origin of leuchtenbergite-bearing metamorphics in the Sopron area. Földtani Közlöny **117:** 31-45 (in Hungarian with English abstract).
Kisházi, P. & Ivancsics, J. (1989): Petrogenesis of the Sopron Gneiss Formation. Földtani Közlöny **119:** 153-166 (in Hungarian with English abstract).
Kohn, M.J. & Malloy, M.A. (2004): Geochim. Cosmochim. Acta 68, 101–113.
Lelkes-Felvári, Gy., Sassi, F.P. & Visoná, D. (1984): Pre-Alpine and Alpine developments of the Austridic basement in the Sopron area (Eastern Alps, Hungary). Rend. Soc. It. Miner. Petr. **39:** 593-612.
Lesnov, F.P. & Anushin, G.N. (2013): CRC Press, ISBN-13: 978-0-203-11967-9, 300.
Likhanov, I.I., Reverdatto V.V. (2016) Quantitative analysis of mass transfer during polymetamorphism in pelites of the Transangarian Yenisei Ridge. Russian Geology and Geophysics, 57, 1204-1220.
Liu, Y., Hu Z., Gao, S., Günther, D., Xu, J., Gao C., Chen, H., 2008: In situ analysis of major and trace elements of anhydrous minerals by LA-ICP-MS without applying an internal standard. Chemical Geology 257 (2008) 34–43.
Manning 1983
McDonough, W.F. & Sun, S.-S. (1995): Chem. Geol. 120 223-253.
Moore, S.J. Carlson, W.D. (2010): Common patterns of rare-earth-element distribution in garnet. AAPG Search and Discovery Article #90172 © CSPG/CSEG/CWLS GeoConvention 2010, Calgary, Alberta, Canada, May 10-14, 2010
Müller, A., Kearsley, A., Spratt, J., Seltmann, R. 2012 Petrogenetic implications of magmatic garnet in granitic pegmatites from Southern Norway. Can Mineral 50, 1095-1115.
Nagy G., Draganits, E., Demény, A., Pantó, Gy., Árkai, P. 2002, Genesis and transformations of monazite, florenzite, and rhabdophane, during medium grade metamorphism : examples from the Sopron Hills, Eastern Alps. Chem. Geol. 191, 25-46.
Nagy, G., Draganits, E. (1999) Occurrence and mineral chemistry of monazite and rhabdophane in the Lower and ?Middle Austroalpine tectonic units of the southern Sopron Hills (Austria). Mitt. Ges. Geol. Bergbaustud. Österr. 42, 21-36.

Otamendi J.E., de la Rosa, J.D., Patino-Douce, A.E., Castro, A. (2002) Rayleigh fractionation of heavy rare earths and yttrium during metamorphic garnet growth. Geology, 30, 159-162.
Pyle, J.M. & Spear, F.S. (1999): Yttrium zoning in garnet: Coupling of major and accessory phases during metamorphic reactions. Geological Materials Research 1, 1– 49.
Rajta, I., Borbély-Kiss, I., Mórik, Gy., Bartha, L., Koltay, E., Kiss, ÁZ (1996): The new ATOMKI scanning proton microprobe, Nucl. Instr. and Meth. B 109-110, 148-153
Schmolke, M.K., Zack, T., O'Brien, P.J., Jacob, D.E. (2008): Earth and Planetary Science Letters 272 488–498.

N. Shimizu, Rare earth elements in garnets and clinopy-roxenes from garnet lherzolite nodules in kimberlites, Earth Planet. Sci. Lett. 25, 26-32, 1975.
Shimizu and Richardson, 1987
Spear &Kohn 1996;
Stevens G., Villaros, A., Moyen, J-F. (2007): Geology 35, 9–12.
Storkey et al., 2005
Török, K., (1996): High-pressure/low temperature metamorphism of the Kő-hegy gneiss, Sopron (W-Hungary); Phengite barometry and fluid inclusions Eur. J. Miner. **8:** 917-925.
Török, K. 1998. Magmatic and high-pressure metamorphic development of orthogneisses in the Sopron area, Eastern Alps (W-Hungary) Neues Jahrbuch für Mineralogie Abhandlungen 173, 63-91.
Török, K. 1999. Pre-Alpine development of the andalusite-sillimanite-biotite-schist from the Sopron-Mountains (Eastern Alps, W-Hungary). Acta Geologica Hungarica 42 (2), 127-160.
Török, K. 2001. Multiple fluid migration events in the Sopron Gneisses during the Alpine high-pressure metamorphism, as recorded by bulk-rock and mineral chemistry and fluid inclusions. Neues Jahrbuch für Mineralogie Abhandlungen 177 (1), 1-36.
Török, K. 2003. Alpine P-T path of micaschists and related orthogneiss veins near óbrennberg (W-Hungary, Eastern Alps). Neues Jahrbuch für Mineralogie Abhandlungen 179 (2), 101-142.
Uzonyi, I., Rajta, I., Bartha, L., Kiss, ÁZ., Nagy A. (2001): Realization of the simultaneous micro-PIXE analysis of heavy and light elements at a nuclear microprobe, Nucl. Instr. and Meth. B 181 (1-4), 193-198
Wang etal 2003 Chinese Science Bulletin Vol. 48 No. 15 August 2003 1615
Yang, P. & Rivers, T. (2002): Geol. Mat. Res. 4, 1–35.